

**Unclassified**

**NEA/CSNI/R(2013)5**

Organisation de Coopération et de Développement Économiques  
Organisation for Economic Co-operation and Development

**15-Jul-2013**

**English text only**

**NUCLEAR ENERGY AGENCY  
COMMITTEE ON THE SAFETY OF NUCLEAR INSTALLATIONS**

**Report of the OECD/NEA KAERI Rod Bundle CFD Benchmark Exercise**

**JT03343001**

**Complete document available on OLIS in its original format**

*This document and any map included herein are without prejudice to the status of or sovereignty over any territory, to the delimitation of international frontiers and boundaries and to the name of any territory, city or area.*



NEA/CSNI/R(2013)5  
**Unclassified**

**English text only**

## ORGANISATION FOR ECONOMIC CO-OPERATION AND DEVELOPMENT

The OECD is a unique forum where the governments of 34 democracies work together to address the economic, social and environmental challenges of globalisation. The OECD is also at the forefront of efforts to understand and to help governments respond to new developments and concerns, such as corporate governance, the information economy and the challenges of an ageing population. The Organisation provides a setting where governments can compare policy experiences, seek answers to common problems, identify good practice and work to co-ordinate domestic and international policies.

The OECD member countries are: Australia, Austria, Belgium, Canada, Chile, the Czech Republic, Denmark, Estonia, Finland, France, Germany, Greece, Hungary, Iceland, Ireland, Israel, Italy, Japan, Luxembourg, Mexico, the Netherlands, New Zealand, Norway, Poland, Portugal, the Republic of Korea, the Slovak Republic, Slovenia, Spain, Sweden, Switzerland, Turkey, the United Kingdom and the United States. The European Commission takes part in the work of the OECD.

OECD Publishing disseminates widely the results of the Organisation's statistics gathering and research on economic, social and environmental issues, as well as the conventions, guidelines and standards agreed by its members.

*This work is published on the responsibility of the OECD Secretary-General.  
The opinions expressed and arguments employed herein do not necessarily reflect the official  
views of the Organisation or of the governments of its member countries.*

## NUCLEAR ENERGY AGENCY

The OECD Nuclear Energy Agency (NEA) was established on 1 February 1958. Current NEA membership consists of 31 countries: Australia, Austria, Belgium, Canada, the Czech Republic, Denmark, Finland, France, Germany, Greece, Hungary, Iceland, Ireland, Italy, Japan, Luxembourg, Mexico, the Netherlands, Norway, Poland, Portugal, the Republic of Korea, the Russian Federation, the Slovak Republic, Slovenia, Spain, Sweden, Switzerland, Turkey, the United Kingdom and the United States. The European Commission also takes part in the work of the Agency.

The mission of the NEA is:

- to assist its member countries in maintaining and further developing, through international co-operation, the scientific, technological and legal bases required for a safe, environmentally friendly and economical use of nuclear energy for peaceful purposes, as well as
- to provide authoritative assessments and to forge common understandings on key issues, as input to government decisions on nuclear energy policy and to broader OECD policy analyses in areas such as energy and sustainable development.

Specific areas of competence of the NEA include the safety and regulation of nuclear activities, radioactive waste management, radiological protection, nuclear science, economic and technical analyses of the nuclear fuel cycle, nuclear law and liability, and public information.

The NEA Data Bank provides nuclear data and computer program services for participating countries. In these and related tasks, the NEA works in close collaboration with the International Atomic Energy Agency in Vienna, with which it has a Co-operation Agreement, as well as with other international organisations in the nuclear field.

This document and any map included herein are without prejudice to the status of or sovereignty over any territory, to the delimitation of international frontiers and boundaries and to the name of any territory, city or area.

Corrigenda to OECD publications may be found online at: [www.oecd.org/publishing/corrigenda](http://www.oecd.org/publishing/corrigenda).

© OECD 2013

You can copy, download or print OECD content for your own use, and you can include excerpts from OECD publications, databases and multimedia products in your own documents, presentations, blogs, websites and teaching materials, provided that suitable acknowledgment of the OECD as source and copyright owner is given. All requests for public or commercial use and translation rights should be submitted to [rights@oecd.org](mailto:rights@oecd.org). Requests for permission to photocopy portions of this material for public or commercial use shall be addressed directly to the Copyright Clearance Center (CCC) at [info@copyright.com](mailto:info@copyright.com) or the Centre français d'exploitation du droit de copie (CFC) [contact@cfcopies.com](mailto:contact@cfcopies.com).

## **THE COMMITTEE ON THE SAFETY OF NUCLEAR INSTALLATIONS**

“The Committee on the Safety of Nuclear Installations (CSNI) shall be responsible for the activities of the Agency that support maintaining and advancing the scientific and technical knowledge base of the safety of nuclear installations, with the aim of implementing the NEA Strategic Plan for 2011-2016 and the Joint CSNI/CNRA Strategic Plan and Mandates for 2011-2016 in its field of competence.

The Committee shall constitute a forum for the exchange of technical information and for collaboration between organisations, which can contribute, from their respective backgrounds in research, development and engineering, to its activities. It shall have regard to the exchange of information between member countries and safety R&D programmes of various sizes in order to keep all member countries involved in and abreast of developments in technical safety matters.

The Committee shall review the state of knowledge on important topics of nuclear safety science and techniques and of safety assessments, and ensure that operating experience is appropriately accounted for in its activities. It shall initiate and conduct programmes identified by these reviews and assessments in order to overcome discrepancies, develop improvements and reach consensus on technical issues of common interest. It shall promote the co-ordination of work in different member countries that serve to maintain and enhance competence in nuclear safety matters, including the establishment of joint undertakings, and shall assist in the feedback of the results to participating organisations. The Committee shall ensure that valuable end-products of the technical reviews and analyses are produced and available to members in a timely manner.

The Committee shall focus primarily on the safety aspects of existing power reactors, other nuclear installations and the construction of new power reactors; it shall also consider the safety implications of scientific and technical developments of future reactor designs.

The Committee shall organise its own activities. Furthermore, it shall examine any other matters referred to it by the Steering Committee. It may sponsor specialist meetings and technical working groups to further its objectives. In implementing its programme the Committee shall establish co-operative mechanisms with the Committee on Nuclear Regulatory Activities in order to work with that Committee on matters of common interest, avoiding unnecessary duplications.

The Committee shall also co-operate with the Committee on Radiation Protection and Public Health, the Radioactive Waste Management Committee, the Committee for Technical and Economic Studies on Nuclear Energy Development and the Fuel Cycle and the Nuclear Science Committee on matters of common interest.”

**REPORT OF THE OECD/NEA–KAERI ROD BUNDLE  
CFD BENCHMARK EXERCISE**

B. L. Smith  
Paul Scherrer Institute, Villigen PSI, Switzerland

C.-H. Song; S.-K. Chang; J. R. Lee; J. W. Kim<sup>#</sup>  
Korea Atomic Energy Research Institute (KAERI), Daejeon, Republic of Korea

---

<sup>#</sup> Now at Seoul National University of Science and Technology (SNUST), Seoul, Republic of Korea

## EXECUTIVE SUMMARY

The OECD/NEA-KAERI MATiS-H Benchmark was initiated to test the ability of state-of-the-art Computational Fluid Dynamics (CFD) codes to predict important turbulence parameters downstream of a generic design of spacer grid in a rod-bundle geometry. The presence of the spacer grid is an important factor in both fuel economy and safety, because of the enhanced heat transfer it generates, enabling more efficient cooling of the fuel rods, and an increased safety margin to critical heat flux. Generally, spacer grid design is highly proprietary information, and there is little opportunity for CFD analysts working in the area to compare their numerical approaches.

The MATiS-H experimental facility at the Korea Atomic Energy Research Institute (KAERI) has been used in the past in the development of advanced nuclear fuels in Korea. To stimulate an international assessment of the different numerical approaches to spacer grid design using CFD, KAERI agreed to perform a series of experiments using this facility, and to offer the data to the CFD community.

The test section consists of a square channel of 170x170 mm cross-section and 4670 mm length. The channel contains a 5x5 rod bundle, each of the 25 rods being of 25.4 mm outer diameter and 3863 mm in length, representing the fuel rods in an actual fuel bundle. The rods serve only as blockages in the test, and are not heated. The working fluid is water. The test rig is 2.6 times larger than an actual reactor-grade bundle in order to provide good measurement resolution. A mixing spacer grid is situated in the rod bundle for enhancing lateral flow mixing. Experiments were conducted for two spacer grid designs, of the split-type and swirl-type. The Reynolds number based on the hydraulic diameter within the rod bundle was  $Re \sim 50\,000$ , corresponding to an axial bulk velocity of  $\sim 1.50$  m/s within the bundle region. Conditions in the water loop were closely controlled in the tests to maintain a constant temperature of 35°C and an ambient pressure of 1.57 bar. Detailed measurements of the velocity field were taken in the bundle using a 2-D LDA system at four downstream locations from the spacer grid: 0.5, 1.0, 4.0 and 10.0  $D_H$ , measured from the downstream edge of the spacer grid. Flow conditions (in terms of mean and fluctuating velocities) were also measured upstream of the spacer grid, specifically to provide suitable inlet boundary conditions for the associated CFD simulations.

Participants in the benchmark exercise were given the (steady) volumetric flowrate. Fully developed flow conditions in the 5x5 rod bundle geometry were anticipated upstream of the spacer grid in this experiment. To confirm this, an additional experiment was conducted, with details as follows. The inlet length of about 100  $D_H$  upstream of the spacer grid was originally chosen to ensure fully developed flow conditions on the upstream side of the spacer grid. However, it was considered desirable to have inlet boundary conditions at about 10  $D_H$  upstream of the spacer grid from the viewpoint of the CFD simulations. These were provided (from the measurements taken from an additional experiment for which the spacer grid had been removed) in terms of flow profiles of the axial and lateral mean and root-mean-square (rms) velocities, both in graphical and tabular forms. To aid mesh generation, Computer-Aided-Design (CAD) files were produced by KAERI for both spacer-grid designs and, after implementation of quality control procedures, made ready for distribution to participants in several standard formats.

An organising committee was set up early in 2011, which included the director of the Thermal-Hydraulics Safety Research Division, KAERI, S. Korea (C.-H. Song), who had overseen this and the previous experiments performed in the MATiS-H test facility. Detailed specifications were drawn up ahead of a formal announcement of the benchmark exercise, and an invitation to attend a kick-off meeting held on April 28, 2011 at the NEA headquarters in Paris was sent out to more than 750

interested parties. Of these, 48 formally registered interest in the exercise, and consequently received the detailed specifications and CAD files. The specifications also included instructions for standard formatting of the requested data files to facilitate easy processing of the numerical data. A deadline of April 30, 2012 was set for participants to present their data files to the organisers for synthesis. The deadline was extended by almost one month to facilitate some late submissions, but finally closed on May 29, 2012 ahead of an *Open Meeting* on May 30, 2012, also held at the NEA HQ in Paris, when the downstream test data were opened for the first time. Participants were warned that if they did not present their blind predictions by this extended deadline, they would not later be able to withdraw them, and their results would then be included in the subsequent synthesis.

In total, 25 participants submitted blind CFD results by the extended deadline, and these have consequently been included in the synthesis report, which was presented as an invited paper at the CFD4NRS-4 Workshop held in Daejeon, S. Korea from 10-12 Sept. 2012. For completeness, the salient points from this paper are included in Section 5 of this document. Of the 25 submissions, fifteen (15) used a Reynolds-Averaged Navier Stokes (RANS) turbulence model, four (4) used a hybrid approach, while the remaining six (6) used Large Eddy Simulation (LES). Ten (10) addressed only the split-type spacer grid; three (3) addressed only the swirl-type, while twelve (12) addressed both. The number of control volumes spanned 700K to 144M. Of the simulation results submitted, the majority (19) were obtained using the three commercial CFD software packages ANSYS CFX, FLUENT and STAR-CCM+. The rest were derived from the open software OpenFoam (1), and various in-house CFD codes (5).

A comprehensive analysis of calculated results has revealed that overall good agreement with experimental data can be achieved with a moderate number of mesh cells, and less-sophisticated turbulence models, provided care is taken to follow Best Practice Guidelines, and the use of first-order space discretisation is avoided. Generally, the scale-resolving turbulence models performed well. While the simple RANS models were able to capture the mean velocity profiles quite well, they showed evidence of being over-diffusive for this application. In complete contrast to the previous T-junction benchmark, the SAS-SST turbulence model has performed well in this exercise for the split-type spacer design, but is still inferior to full Large Eddy Simulation (LES) simulations for the swirl-type design.

In conclusion, the benchmark exercise was very successful, and of international appeal. Notwithstanding the non-prototypic nature of the grid spacers used in this exercise, the activity has supported the mission of extending the existing assessment database for spacer grid design using CFD.

## TABLE OF CONTENTS

1. MOTIVATION AND BACKGROUND.....	9
1.1 The CFD4NRS Workshop Series .....	10
1.2 Construction of the CFD for NRS Wiki Pages .....	10
1.3 Benchmark Exercise on Thermal Fatigue.....	11
1.4 Benchmark Exercise on Turbulence in a Rod Bundle Generated by Spacer Grids .....	11
2. ORGANISATIONAL PROCEDURES .....	13
2.1 CSNI Approval .....	13
2.2 The Work of the Benchmark Organising Committee .....	13
3. EXPERIMENTAL FACILITY .....	17
3.1 General Layout .....	17
3.2 Instrumentation .....	19
3.3 LDA Measurements .....	20
3.4 Upstream Measurements.....	22
3.5 Supplementary Experiment: Inlet Conditions.....	22
3.6 Downstream Measurements.....	24
3.6.1 Lateral Downstream Velocity Measurements .....	25
3.6.2 Axial Downstream Velocity Measurements.....	28
3.6.3 Vorticity Contour .....	30
3.7 Supplementary Experiment: End Effects.....	31
4. COMPUTATIONS.....	33
4.1 Submissions .....	33
4.2 Codes and Models.....	37
4.3 Data Requested .....	38
4.4 Unofficial Additional Information: CAD File of MATiS-H.....	38
5. SYNTHESIS OF RESULTS.....	41
5.1 Introduction.....	41
5.2 Available Data .....	41
5.3 Inlet Flow Conditions .....	41
5.4 Metric for Comparison.....	42
5.5 Rankings for Split-Type Spacer Simulations.....	42
5.5.1 Mean Velocities .....	42
5.5.2 Time-Averaged RMS Velocities.....	44
5.5.3 Best estimation for different turbulence models .....	45
5.5.4 Use of Periodic Boundary Conditions.....	46
5.5.5 Time-Averaged Circulation in a Sub-Channel.....	48
5.5.6 Rankings based on combined mean and rms predictions.....	49
5.6 Rankings for Swirl-Type Spacer Simulations.....	51
5.6.1 Mean Velocities .....	51
5.6.2 Time-Averaged RMS Velocities.....	51
5.6.3 Best Estimation for Top-Ranked Simulations.....	52
5.6.4 Use of Periodic Boundary Conditions.....	54
5.6.5 Time-Averaged Circulation Data in a Sub-Channel .....	55
5.6.6 Rankings based on combined mean and rms predictions.....	57
5.7 Conclusions from the Synthesis of Results.....	58
6. OVERALL CONCLUSIONS .....	61

ACKNOWLEDGMENTS.....	65
REFERENCES.....	67
ANNEX 1: ANNOUNCEMENT .....	69
ANNEX 2: SPECIFICATIONS .....	73
ANNEX 3: NOMENCLATURE.....	123

## 1. MOTIVATION AND BACKGROUND

*An Exploratory Meeting of Experts to Define an Action Plan on the Application of Computational Fluid Dynamics (CFD) Codes to Nuclear Reactor Safety (NRS) Problems* took place in Aix-en-Provence, France on 15-16 May, 2002 [1]. It was a meeting jointly sponsored by the IAEA\* and the OECD/NEA‡. A follow-up meeting, *Use of Computational Fluid Dynamics (CFD) Codes for Safety Analysis of Reactor Systems including Containment*, took place in Pisa on 11-14 Nov., 2002 [2]. These joint meetings resulted in the formulation of an action plan recommending the creation of three Writing Groups, overseen by the WGAMA# committee of the OECD/NEA, and with mandates to perform the following tasks:

- WG1 Provide a set of guidelines for the application of CFD to NRS problems;
- WG2 Evaluate the existing CFD assessment bases, identify any gaps, and initiate activities aimed at broadening the assessment database;
- WG3 Summarise the extensions needed to CFD codes for application to two-phase NRS problems.

Work began early in 2003. Teams of experts were assigned to each of the groups, representing the following OECD member countries: the Czech Republic, France, Germany, Italy, Japan, S. Korea, the Netherlands, Norway, Sweden, Switzerland and the USA. Preliminary reports were submitted to WGAMA group in September 2004, which scoped the work needed to be carried out to fulfil the respective mandates, and which also made recommendations on how to achieve the defined objectives. In January 2005, all three groups were re-formed to carry out their respective tasks. The work was concluded in December 2007, and CSNI reports were eventually issued by each group describing the work undertaken [3,4,5].

The WG2 Writing Group provided evidence to show that CFD is a tried-and-tested technology, and that the main industrial-level CFD vendors were themselves taking active steps to quality assure their software products by testing their codes against standard test data, and through active participation in international benchmarking exercises. However, in a period of low growth in the nuclear power industry (starting in the 1980s), the primary driving forces for the development of CFD technology remained for several years in non-nuclear areas, such as in the aerospace, automotive, marine, turbo-machinery, chemical and process industries, and to a lesser extent the environmental and biomedical industries. In the power-generation arena, the principal applications were again non-nuclear: combustion dynamics for fossil-fuel burning and gas turbines, vanes for wind turbines, etc. A resurgence of interest in nuclear occurred from 2005 to 2011, a period which coincided with the issue of the WG reports, but has now been interrupted again as a consequence of the Fukushima accident on March 11, 2011.

---

\*International Atomic Energy Agency

‡Organisation for Economic Cooperation and Development, Nuclear Energy Agency

#OECD/NEA Working Group on the Analysis and Management of Accidents

During the period in which the WG2 group met, and accepting the commission to not only report on the existing assessment databases for the application of CFD to nuclear reactor safety issues but also to take steps to broaden and extend the databases, three new initiatives were taken:

1. To organise a new series of international workshops to provide a forum for experimenters and numerical analysts to meet and exchange information;
2. To encourage nuclear departments at universities and research organisations to release previously unpublished test data by initiating international numerical benchmark exercises; and
3. To establish a Wiki-type web portal to give online access to the information collated by the WGs, as documented in their final reports, and, via user input, to provide a means for updating and extending the information they contained. A special *CFD Task Group* was set up by WGAMA for this purpose, and is due to report back to the CSNI by the end of 2012.

### 1.1 The CFD4NRS Workshop Series

The first of the international workshops took place in Garching, Germany in 2006 [6], and was organised directly by the WG2 group, which was still sitting at this time. Selected papers from the workshop were subsequently published in a special issue of Nuclear Engineering and Design [7]. Further workshops in the series, as well as the benchmarking and webpage initiatives, were organised via a smaller *Special CFD Group* formed later by WGAMA. This group consisted of the chairmen of the three Writing Groups, together with the NEA secretariat.

The second workshop in the series, XCFD4NRS, took place in Grenoble, France in September 2008 [8], and concentrated more on multi-phase aspects, the focus of the WG3 Writing Group. The third workshop, CFD4NRS-3, took place in Washington DC in September 2010, and the fourth took place in Daejeon, Korea in September 2012. This last workshop was organised by KAERI, and included a special visit to the MATiS-H test facility in association with this benchmark exercise.

### 1.2 Construction of the CFD for NRS Wiki Pages

The three CSNI documents, like any state-of-the-art reports, are only up-to-date at the time of writing, and, given the rapidly expanding use of CFD as a refined analysis tool in nuclear technology, the information they contain will soon become outdated. To preserve their usefulness and topicality, improvements and extensions to the documents are foreseen. It was decided that the most efficient vehicle for regular updating would be to create a Wiki-type web portal. Consequently, in a pilot study, a dedicated webpage has been created on the NEA website using Wikimedia software [9]. The WG1 and WG2 documents in the forms they appear in the respective archival documents [3,4] have now been uploaded to provide online access to the material they contain. The webpages for the WG3 document [5] are under construction.

All the main chapters of the Writing Group documents have been made active links to the subject material on the respective webpages, and have been subdivided where necessary. Active links are installed at all levels to enable the user to navigate quickly to other parts of the respective documents. All webpage addresses, for example to the commercial CFD sites, are also active, and it is planned to install similar links for the journal references too, which will be useful for registered subscribers with electronic access to the material. However, the most useful feature of the web portal is the opportunity to modify, correct, update and extend the information contained there, the Wiki environment being the vehicle for this. The aim is to have a static site with unrestricted access. Readers will not be able to directly edit or change the information, but can communicate their suggestions to the website editors. In parallel, a beta version of the webpages will be maintained for installing updates prior to transfer to the static site. At present, access to the beta version is restricted to the three former chairmen of the Writing Groups, who have editing responsibility for the website versions of their respective documents, together with the NEA secretariat and webmaster. It will be each respective editor's

responsibility to review all new submissions, and implement them into the open-access version of the site, following approval by the CSNI. This responsibility has since been extended to a full CFD Task Group under the auspices of WGAMA.

### **1.3 Benchmark Exercise on Thermal Fatigue**

During a meeting of the three Writing Group chairmen convened in Grenoble in September 2008 at the conclusion of the 2<sup>nd</sup> of the workshops, XCFD4NRS [8], discussions were held concerning candidate experiments around which to organise an international CFD benchmark exercise; both single-phase and two-phase options were considered. It was generally acknowledged that it would be desirable to have the opportunity of performing a “blind” benchmark, and this would entail finding a completed experiment for which the data had not yet been released, or encouraging a new experiment (most likely in an existing facility) to be undertaken especially for this exercise. The group took on the responsibility of finding a suitable experiment, for providing the organisational basis for launching the benchmark exercise (though not on the scale of an International Standard Problem, ISP), and for the synthesis of the results. An early opportunity came in the area of thermal fatigue associated with flow mixing in a T-junction. Vattenfall R&D, Älvkarleby, Sweden, agreed to release previously unpublished test data from one of their T-junction experiments in support of this benchmarking activity, and assigned the member of their staff who had performed the experiment to the Special CFD Group to give hands-on expertise.

The benchmark exercise was carried out, under the supervision of WGAMA, between 2009 and 2011, terminating in the issue of a full CSNI report [10], a paper delivered at the 15<sup>th</sup> Int. Topical Meeting on Nuclear Reactor Thermal Hydraulics (NURETH-15) in Toronto [11], and which will subsequently appear in the special issue of Nuclear Engineering and Design dedicated to this conference. Of the 69 participants who registered interest in participation, 29 submitted blind CFD results, which were then included in the synthesis. The procedural steps established during the coordination of this benchmark activity have been used as a template for the current exercise.

### **1.4 Benchmark Exercise on Turbulence in a Rod Bundle Generated by Spacer Grids**

The Korea Atomic Energy Research Institute (KAERI) had participated in the T-junction benchmark exercise, and subsequently made approaches to the OECD/NEA Special CFD Group with the offer of providing previously unpublished test data to serve as a basis for a similar benchmarking activity on the issue of turbulent mixing downstream of a spacer grid in a rod bundle geometry. It was recognised that an international benchmarking activity of this nature would be welcome, since the design of spacer grids in fuel rod bundles is highly proprietary information, this being true also in Korea. However, KAERI were prepared, at their own expense, to design, manufacture and test in their MATiS-H facility spacer grids of a generic type, and offer the data to the CFD community in the framework of an OECD/NEA benchmarking activity. Moreover, KAERI were prepared to offer CAD files of two generic designs of grid spacer – of “split-type” and “swirl-type” – as an aid to grid generation on the part of the participants in the exercise.

Tests were to be performed under single-phase, isothermal conditions, to concentrate the effort on the turbulence characteristics of the flow generated by the grid geometry. High quality Laser Doppler Velocimetry (LDV) techniques in three dimensions would be employed to provide time-averaged (mean and rms) velocity data suitable for the assessment of turbulence models incorporated in CFD software. It is often stated, both within and outside the nuclear community, that turbulence modelling is the last mountain to climb in single-phase fluid dynamics, and this exercise, with its direct correspondence to fuel rod cooling and safety margins to CHF, would provide a solid foundation for the use of CFD in this particular application area.

Certainly, there had already been a considerable amount of research activity in the subject [12-20], but till now no direct means to quantify the status of the application of CFD to the technology in terms of a blind comparison exercise. Hence, the instigation of this benchmark would be of topical interest to the CFD community. Consequently, the first steps were taken to initiate the benchmark exercise and invite international participation.

## 2. ORGANISATIONAL PROCEDURES

### 2.1 CSNI Approval

The offer of previously unreleased experimental data to act as a basis for the 2<sup>nd</sup> benchmark activity organised by the Special CFD Group was put before the WGAMA committee in September 2010. A CAPS<sup>†</sup> was prepared, and delivered to the members of WGAMA for consideration. The points put forward to support the proposal were:

- This was the third of the mandate items proposed by the WGAMA Special CFD Group in 2007, and the other two items – the organisation of the CFD4NRS workshops and the setting up of a web-based portal for information relating to the use of CFD in NRS – were already approved and ongoing.
- A very successful CFD benchmark activity based on the T-junction experiment performed at Vattenfall R&D had just concluded, and the present benchmark would be organised similarly.
- The Special CFD Group would undertake the synthesis of the numerical results, including the comparison with measured data, and report its findings at the next scheduled Workshop in the series, CFD4NRS-4, already approved by WGAMA, to be held in September 2012, and organised by KAERI.
- The exercise would complement ongoing industrial studies, but for which the test data were restricted.
- Maximisation of heat removal from nuclear fuels under normal or transient operation and accidental conditions is very important in the safety (and economics) of nuclear power plants. This is very closely related to the turbulent flow structures in the rod bundles, and these are directly affected by the design of the spacer grids.
- Because of the complex geometric factors involved, it is recognised that CFD has a unique analysis function to perform in this context, and many groups would be interested in assessing their analytical skills in such an internationally sponsored programme.
- Several organisations from Canada, the Czech Republic, Finland, France, Germany, Hungary, Italy, Korea, the Netherlands, Slovenia, Spain, Sweden and Switzerland had expressed interest in participating in this benchmark.

After some discussion, the CAPS was approved, passed on to the Project Review Group (PRG) for assessment, and finally endorsed by the CSNI in December 2010. Work began on organising the benchmark activity early in 2011.

### 2.2 The Work of the Benchmark Organising Committee

The organising committee was formed from members of the WGAMA Special CFD Group, together with the KAERI staff member in charge of the rod bundle experiment. Table 1 lists the members of

---

<sup>†</sup>CSNI Activity Proposal Sheet

the committee, their affiliations, and their principal functions within the scope of the benchmark exercise.

Table 1: Members of the OECD/NEA–KAERI rod bundle CFD benchmark organising committee.

Brian L. Smith	PSI, Switzerland	Chairman
Chul-Hwa Song	KAERI, S. Korea	Had overseen the MATiS-H experiment
John H. Mahaffy	PSU (Emeritus), USA	To provide support in the synthesis
Ghani Zigh	US NRC, USA	Had organised the CFD4NRS-3 workshop, and to provide valuable expertise
Dominique Bestion	CEA, France	Expert, and special advisor on workshop organisation
Abdallah Amri	OECD/NEA, France	Secretariat

A date was fixed for a kick-off meeting of the benchmark exercise (28 April, 2011), and the secretariat made the arrangements for this to take place at the NEA Headquarters in Paris. An announcement was prepared (reproduced in Annex 1) and sent out to more than 750 prospective participants on March 6, 2011 with an invitation to (i) attend the kick-off meeting, and/or (ii) register as a participant in the benchmarking exercise. In total, 48 registrations were made from organisations in 21 countries. Table 2 lists the countries specifically, and the number of registrations per country. All registered participants subsequently received the official benchmark specifications. The kick-off meeting was attended by 28 delegates, with apologies from a further eight (8), who had originally intended to come, but then could not for various reasons. The minutes of the meeting are documented [21].

Table 2: Registrations to the OECD/NEA–KAERI rod bundle CFD benchmark.

Belgium	1	Germany	9	Netherlands	2	Switzerland	3
Canada	4	Greece	1	Russia	3	UAE	2
Czech Republic	2	Hungary	1	Slovakia	1	UK	2
Egypt	1	Italy	1	Slovenia	1	USA	3
Finland	2	Japan	1	Spain	2		
France	3	S. Korea	3	Sweden	1		

To set the scene at the kick-off meeting, C.-H. Song and S.-K. Chang from KAERI gave specific details of the MATiS-H test facility, the construction of the CAD files of the two spacer-grid designs, and invited suggestions on what else could be supplied. In response, some delegates voiced their concerns that the measurement plane was too closely situated to the outlet manifold, and that there would be some influence of the outlet conditions on the exit boundary conditions specified for the benchmark exercise for the associated CFD simulations. KAERI replied that this issue was currently being investigated using CFD, and that there could be provision made for some further experimental tests to clarify this point.

The final timetable for the benchmark activity is given in Table 3. A draft version of the benchmark specifications was circulated to all registered participants on June 10, 2011 with an invitation for

feedback concerning errors, clarity, ambiguity and possible misunderstandings. A number of comments were received, answered appropriately by email, and some modifications to the specifications were made. Taking account of these changes, the benchmark specifications were re-issued on July 15, 2011. This gave participants more than nine months to complete their calculations and submit their results by the deadline date of April 30, 2012.

Table 3: Timetable for the OECD/NEA–KAERI CFD rod bundle CFD benchmark.

April 28, 2011	Kick-Off Meeting
May 13, 2011	Distribution of draft version of the Benchmark Specifications (geometry only)
June 10, 2011	Distribution of draft version of the Benchmark Specifications (flow parameters)
June 30, 2011 (extended)	Deadline set for comment/queries from participants concerning the Benchmark Specifications to be submitted to the organisers
July 15, 2011	Official Distribution of the Benchmark Specifications (geometry and flow data)
Dec. 20, 2011	Distribution of MATiS-H CAD file prepared by JRC, Petten
April 30, 2012	Deadline for receipt of simulation results (extended to May 29)
May 30, 2012	Open Benchmark Meeting (first opening of the test data)
Sept. 10, 2012	Presentation of results and synthesis at CFD4NRS-4 Workshop

The deadline for submission was generally respected, because of the date of the timing of the Open Benchmark Meeting on May 30, 2012, at which time the test data would be opened for the first time. As seen at the previous benchmark in this series, some delegates had last-minute problems with their submittals, so the deadline was extended to May 29, 2012, one day before the opening of the downstream data. Reminders that the deadline for submission was approaching were sent to all registered participants on Feb. 11 and April 12, 2012, which provided sufficient encouragement for the bulk of the bulk of the submissions to be supplied on time. Participants were also reminded that following the extended deadline of May 29, 2012, they would not be permitted to exchange or withdraw their submitted results, which would then automatically become part of the official benchmark synthesis.

Due to security restrictions on the KAERI website, automatic uploading of results was not possible, and participants were instructed to attach their data files to email communications. This procedure worked well in most cases, and special consideration was given to those participants who experienced difficulties with the procedure. Each participant was given the option to exchange the files submitted for updated ones at any time up to the deadline date, but then no further changes were permitted.

In total, 25 submissions were received by the time of the extended deadline. Based on the bad experience gained for the T-junction benchmark activity, in which there were often formatting errors in the files submitted, the Python script, which would subsequently be used to examine the files, was sent to each participant in advance for testing. This procedure followed the recommendations made by John Mahaffy, who was the person responsible for the synthesis of the T-junction benchmark. All 25 submissions were included in the subsequent analysis carried out by C.-H. Song, J.R. Lee and J.W. Kim (KAERI), the synthesis being presented as a plenary lecture delivered by C.-H. Song, at the CFD4NRS-4 Workshop in Daejeon, S. Korea on September 10, 2012. In addition, a special Poster Session was organised at the workshop, where participants could display their results without the need

to prepare an accompanying paper. Any subsequent post-test simulations they had performed since release of the downstream test data could also be shown at this time.

The Open Benchmark Meeting was attended by 22 participants in the benchmark exercise, plus members of the Organising Committee, and the NEA Secretariat. B. L. Smith (PSI) made a presentation giving the background to the benchmark activity, C.-H. Song (KAERI) summarised the simulation data received, and described the preparations being made at the CFD4NRS-4 Workshop in regards to the benchmark activity, and S.-K. Chang (KAERI) presented the measured velocity data downstream for both the spacer types. A very preliminary synthesis of the benchmark results was presented by K.-Y. Kim of INHA University, Incheon, S. Korea, who was acting as a consultant for KAERI in this matter. All participants at the meeting received paper copies of all the presentations, and a CD was also produced and distributed. It was explained that the downstream data would be made available to all participants following their signing of a confidentiality agreement in which they acknowledged that the data remained the exclusive property of KAERI, and were subject to publication only within the context of this benchmark exercise. With this proviso, all those registered members of the benchmark who had submitted results ahead of the (extended) deadline would then have access to the downstream data. The released data files were in the form of Excel spreadsheets.

An open discussion session then followed, in which participants asked questions, aired views, and made suggestions for improvement in the organisation of the benchmark and the presentation of the results. Interest in the benchmark activity remained high, and a suggestion was made of whether an open forum could be set up at the CFD4NRS-4 Workshop where participants could exchange their experiences. (This was agreed, and a Poster Session at the Workshop was subsequently arranged.)

Most of the comments made were minor, and did not affect the submitted results.

- There were sometimes communication problems. These were due to the time difference between Korea and Europe, and particularly the USA, as well as security issues associated with the KAERI website, and the subsequent overhead in dealing with large email attachments.
- The organisers expressed regret that there were some minor inconsistencies between data supplied with the CAD files and information in the printed specifications. However, all difficulties were resolved as the benchmark progressed.
- The comment was made that there was some confusion in the specifications due to “vague” statements concerning the reliability of near-wall velocity measurements. This was acknowledged, and consequently corrected.
- The question arose of whether there were mechanical vibrations of the test rig that could have contributed to the measured velocity fluctuations. KAERI replied that none were noticed.
- One delegate raised the issue of whether there was information on the surface roughness of the rods and channel wall. KAERI replied that no measurements had been undertaken, but all surfaces were considered smooth.
- There was the suggestion that information concerning the Courant time and minimum time for collecting statistics would have been valuable in the case of transient simulations being performed. This was agreed.
- The two comments were made that (i) gaining access to valuable experimental data provided an incentive to participate in the benchmark exercise, and (ii) the benchmark activity gave participants a good opportunity to know the state-of-the art of CFD codes on a subject of concern for power upgrades and increased safety margins.

### 3. EXPERIMENTAL FACILITY

#### 3.1 General Layout

A full description of the experimental rig is included as part of the official Benchmark Specifications, reproduced in Annex 2, together with the velocity data upstream of the spacer grid (also included in Annex 2). In addition, a paper [22] was presented at the CFD4NRS-4 Workshop detailing the experimental part of the benchmark exercise, and another paper is being prepared for the forthcoming NURETH-15 conference to be held in Pisa in May 2013. However, for completeness, the most salient points are given here also.

A schematic of the MATiS-H experimental rig is given in Fig. 1. This cold loop facility is used to perform hydraulic tests in a rod bundle array under ambient pressure and temperature conditions. The rig consists principally of a water storage tank (e), a circulation pump (f), and a test section (a). The volume of the water in the storage tank and the maximum flow rate of the circulation pump are  $0.9 \text{ m}^3$  and  $2.0 \text{ m}^3/\text{min.}$ , respectively. The flow rate in the loop during operation is controlled automatically by adjusting the rotational speed of the pump, the loop coolant temperature being accurately maintained within a range of  $\pm 0.5\text{K}$  by controlling the heater (i) and the cooler (h) in the water storage tank. For monitoring and controlling the loop parameters (i.e. flow rate, pressure and temperature), a mass flowmeter (m), a gauge pressure transmitter (o) and a thermocouple (n) are installed in the inlet circuit to the test section.

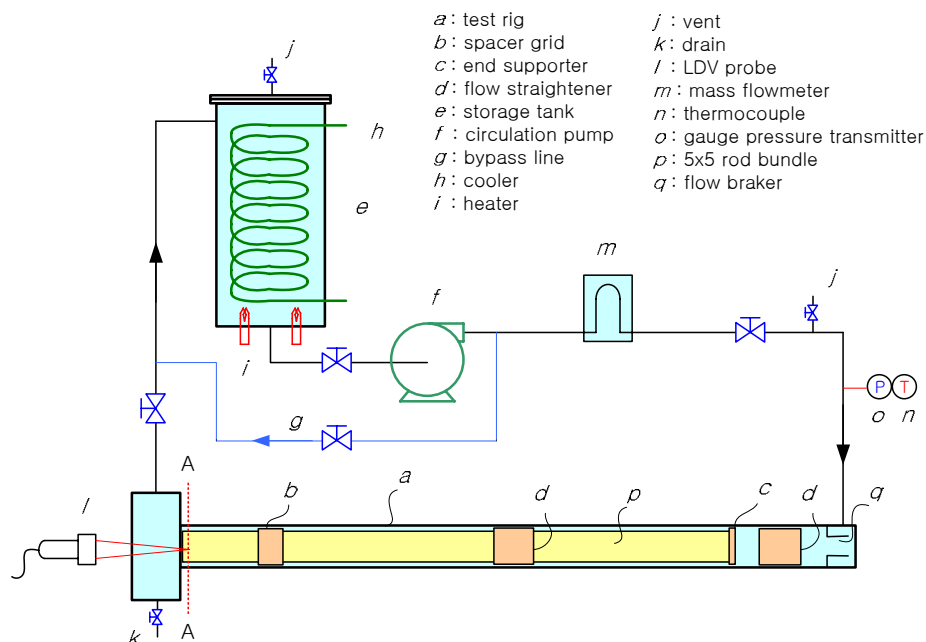


Fig. 1: Schematic of the MATiS-H experimental set-up.

The main body of the horizontal test section comprises a 4670mm-long square duct of inner dimensions 170x170 mm, containing a 3863mm-long 5x5 rod bundle array. Figures 2 and 3 show

front and side views of the test section, together with photos of the LDA probe arrangement. The flow enters the test section vertically at one end (Fig. 3), and exits via the three symmetrical legs attached to the outlet manifold (Fig. 2). All internal devices (i.e. the 25 rods of the 5x5 matrix, the spacer grids and supports) are made from stainless-steel. Acrylic plates are used for the upper and lower covers of the square duct, while Plexiglas® is employed at the front and side windows through which the LDA measurements are made.

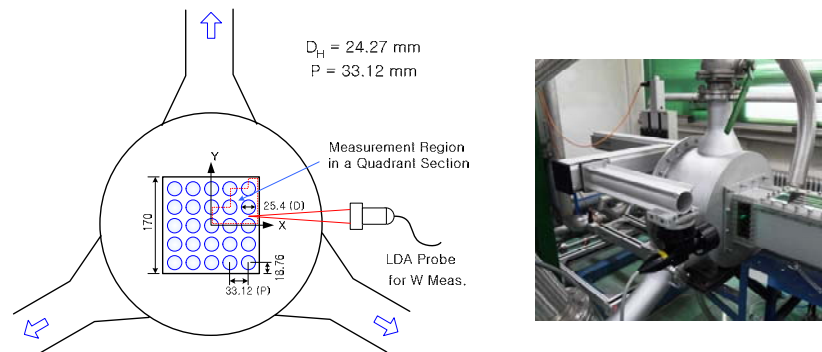


Fig. 2: Front view of the MATiS-H test rig.

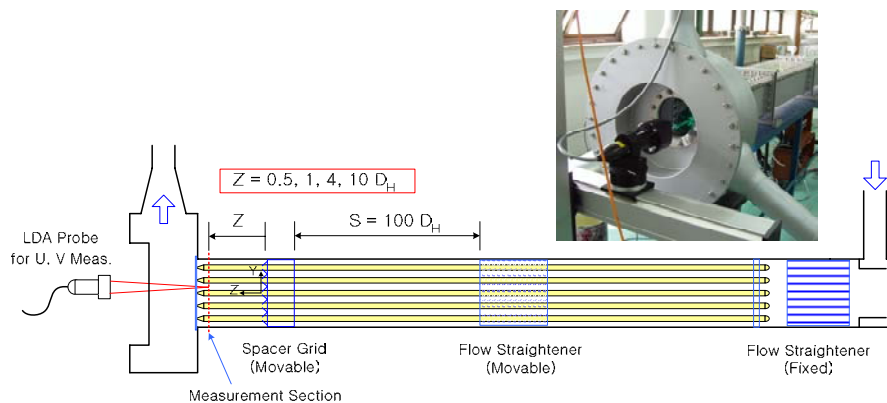


Fig. 3: Side view of the MATiS-H test rig.

One of the spacer grids installed in the rod bundle is of the “split-type”, which features two vanes at each crossing of the grid straps, as shown in Fig. 4(a), the vanes being bent through an angle of  $30^\circ$  with respect to the horizontal. The other spacer grid is of the “swirl-type”, which has four vanes at every crossing of the grid strap, as shown in Fig. 4(b). In this case, the vanes are bent through  $35^\circ$  with respect to the horizontal. More details are given in the official benchmark specifications (Annex 2).

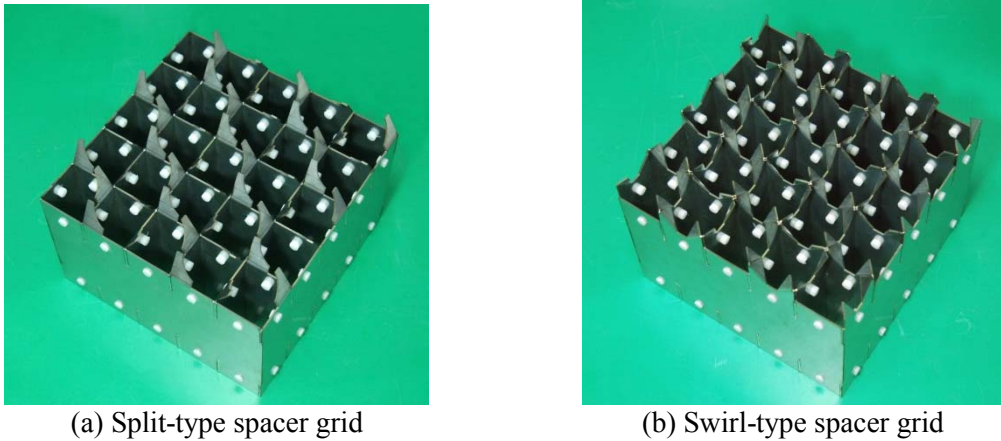


Fig. 4: The two types of spacer grids used in the experiments.

### 3.2 Instrumentation

Table 4 gives the specifications of the instruments used for monitoring and controlling the loop parameters: i.e. system pressure, temperature and mass flow rate.

Table 4: Instrumentation for loop monitoring and control.

Measurement	Instrument	Calibration Range	Accuracy
System Pressure ( $P_{sys}$ )	Rosemount 3051CG	0 ~ 350 kPa	$\pm 0.15\%$ of span
System Temperature ( $T_{sys}$ )	Watlow, T-type, Unground	0 ~ 350°C	$\pm 0.50K$
Mass Flow Rate ( $\dot{m}$ )	Micro Motion CMF300M	0 ~ 37.8 kg/s	$\pm 0.1\%$

A two-component Laser Doppler Anemometry (LDA) system was used to measure the velocities and turbulence properties in the rod bundle. The LDA system consists of a 2-D probe and the FiberFlow optics/transmitter of DANTEC<sup>®</sup>. The laser source used here was the Stabilite 2017 argon-ion laser of Spectra Physics. The 3-D traversing system (9041T033, resolution = 6.25  $\mu\text{m}$ ) of DANTEC<sup>®</sup> was used to move the LDA probe to the correct positions in the measurement region. Seeding particles of hollow glass spheres, with a mean diameter of 10  $\mu\text{m}$  and density 1100  $\text{kg/m}^3$ , were added to the water.

Figure 5 illustrates some properties of the LDA probe used in the experiments. The focal length and beam spacing are 310 mm and 24 mm, respectively, as shown in Fig. 5(a). Thus, the half angle of the beam crossing is 2.217°, which is quite narrow. The reason for choosing this narrow angle probe is to reduce the dead zone of the measurement region near the rods.

The measurement volume is formed as shown in Fig. 5(b), where the elliptical shape has major and minor axis lengths of 3.89 mm and 0.15 mm, respectively. When the probe is used in water, the half angle of the beam crossing is expected to be 1.662°, which is narrower than in air due to beam refraction, as illustrated in Fig. 5(c). In this case, the measurement volume becomes more elongated, with major and minor axes of 6.76 mm and 0.18 mm, respectively.

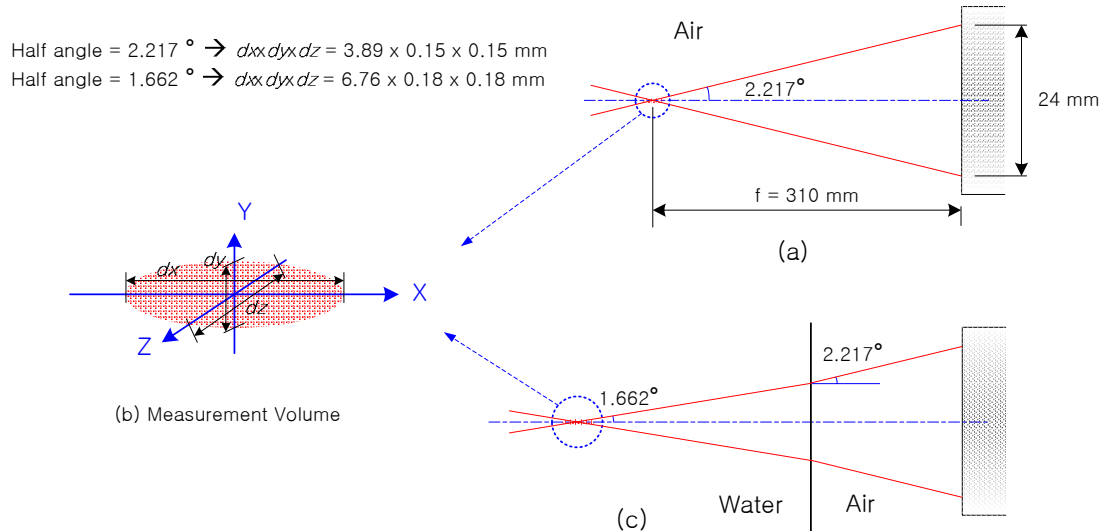


Fig. 5: Measurement volume of an LDA probe.

### 3.3 LDA Measurements

The LDA probe was accurately aligned, based on the geometry of a square duct containing a 5x5 rod bundle, as schematically shown in Fig. 6. Before calibration of the probe position, the laser beam power was reduced to minimise the size of the beam focusing to make the measurement more precise. In the case of the front measurement (Fig. 3), the probe was aligned by repeatedly scanning the centres of the nine rods in a  $90^\circ$  quadrant (marked with crosses in Fig. 6). For the side measurement (Fig. 2), the probe was repeatedly focused on both the inner walls (indicated by the edges at  $\pm 2.566 P$  in Fig. 6), along the x-axis.

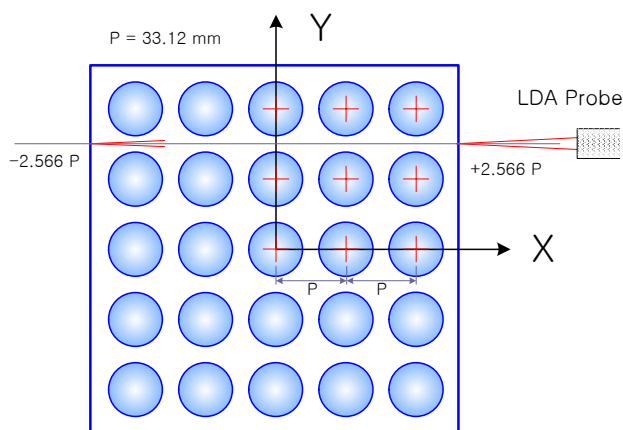


Fig. 6: Details of the LDA probe alignment.

From the shape of the measurement volume of the LDA probe, as detailed above, there will be inherent errors in the near-wall region ( $x > 2.4 P$ ) inside the duct, due to the elongation of the measurement volume in the x-direction for the side measurements of the axial velocity ( $W$ ), as indicated in Fig. 7. From Fig. 7(a), it can be seen that the axial velocities will be measured accurately near the upper wall of the channel, due to the short width of the measurement volume in the y-direction. In contrast, the measurements near the side wall, as shown in Fig. 7(b), will have larger errors because of the adverse shape of the measurement volume. This “undesirable” zone is estimated to be the region  $x > 2.464 P$  in the x-direction, considering the size of the measurement volume given in Fig. 5(c).

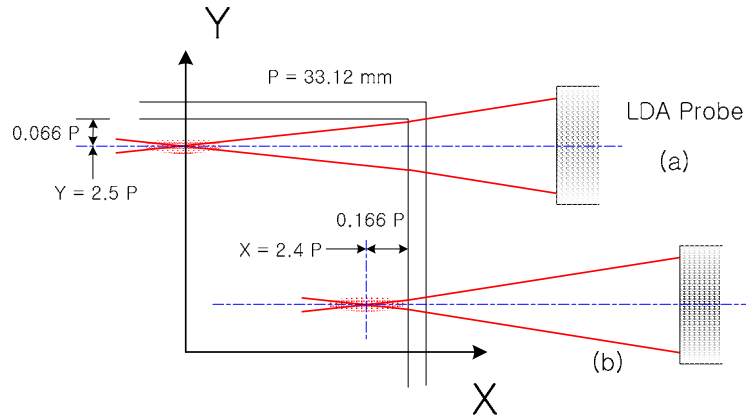


Fig. 7: Illustration of the origin of measurement uncertainties in near-wall regions.

Further evidence of measurement uncertainties in near-wall regions is illustrated in Fig. 8, which shows histograms of the velocity sampling at a measurement point in a near-wall region; the bars in the elongated red circles signify zero velocities, indicating the wall boundary. The averaged values of the samples in near-wall regions appear to underestimate the actual velocities, and the root-mean-square (rms) values of the dispersed sampling produce overestimates for the turbulence intensities. The Figure suggests that the region  $x > 2.4 P$  in the x-direction should be excluded from the measurement data to be made available for CFD validation.

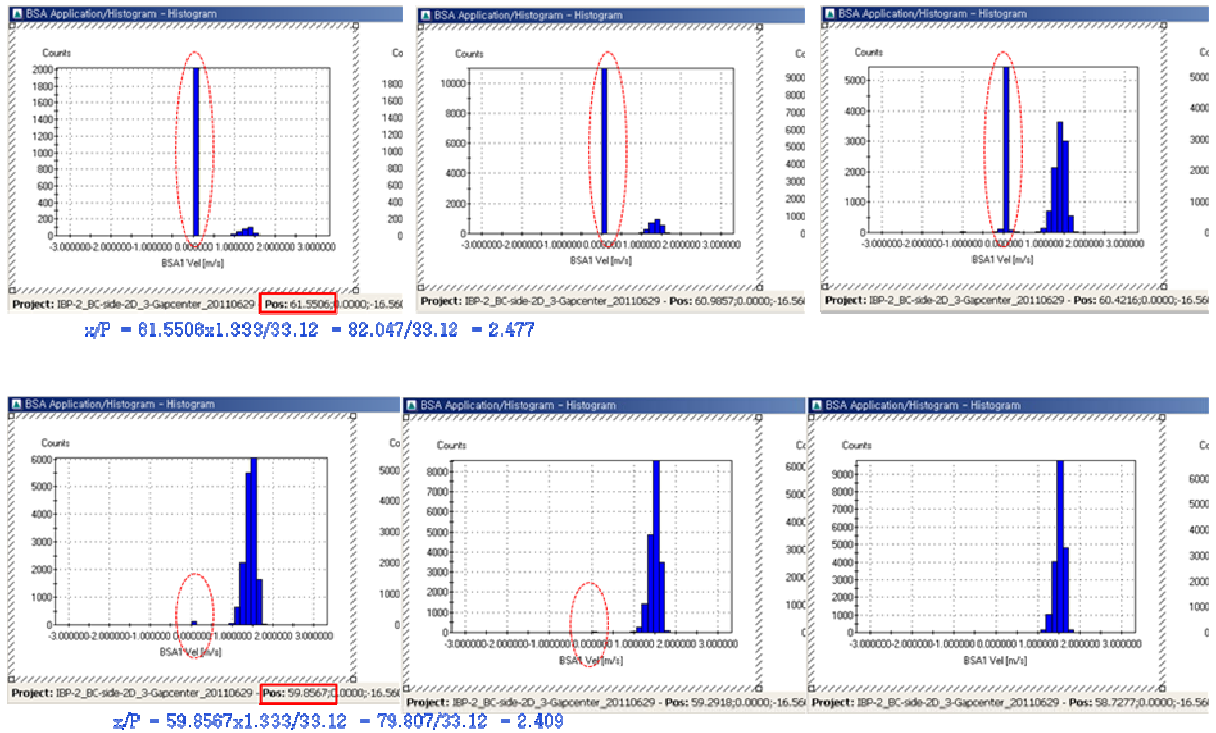


Fig. 8: Histograms of velocity sampling in near-wall regions.

The sources of the LDA measurement uncertainties are divided into random and systematic errors. These two sources of error are then considered to make up the total uncertainty in the velocity measurements. The factors contributing to the systematic error include the uncertainties due to the resolution of the motorised stage, the alignment of the LDA probe, and that of the LDA instrument

itself. The combined uncertainties of the LDA velocity measurements for all lateral and axial components, normalised with respect to the axial bulk velocity, are then estimated to be between 4.8% and 5.1%, with 95% confidence. The random error is only considered in regard to the uncertainty associated with the turbulence intensities, which, again normalised to the axial bulk velocity, is estimated to be between about 0.2% and 1.8% for most of the measured data, though very exceptionally this increases to between 2% and 4.8%.

All velocity signals from the moving particles in the flow field were taken with the option of 20 000 samplings, or any number of samplings over a period of 20 seconds per measurement point.

### 3.4 Upstream Measurements

The experimental conditions were carefully maintained at the specified values for both the downstream and upstream experiments. The test rig was kept at a constant temperature of 35°C using the heater and cooler devices in the water storage tank. The mass flow rate was also preserved by keeping the inverter at a constant frequency of the circulation pump. Consequently, the loop parameters were very strictly controlled for the duration of the test. These loop conditions also gave stable flow parameters for the bulk velocity and Reynolds number. The mean values and the uncertainties of the loop operating conditions are summarised in Table 5.

Table 5: Loop operating conditions.

Parameter		Mean Value	Overall Uncertainty (%)	Measuring Location
Loop Parameter	Mass Flow Rate (kg/s)	24.2	0.29	Pump Discharge
	Temperature (°C)	35	2.90	Test Rig Inlet
	Pressure (kPa)	156.9	0.39	Test Rig Inlet
Flow Parameter	Bulk Velocity, $W_{Bulk}$ (m/s)	1.50	0.37	Test Section
	Reynolds Number, $Re^{\#}$	50 250	2.01	Test Section

$$\# Re = \frac{\rho \cdot W_{Bulk} \cdot D_H}{\mu}$$

### 3.5 Supplementary Experiment: Inlet Conditions

Some participants at the kick-off meeting expressed concern that, though upstream velocities were expected to be turbulent and fully developed, no direct velocity measurements had been made. In response, KAERI undertook to perform an additional experiment to provide definitive velocity data a short distance upstream of the spacer grid for the CFD practitioners to use directly, if they so wished, as inlet boundary conditions for their simulations. It should be emphasised that this supplementary test, the data from which were not part of the official benchmark specifications, was performed by KAERI at their own expense in the spirit of the exercise [22].

For the upstream test, the spacer grid was removed, and the flow straightener positioned 90  $D_H$  from the measuring plane, as indicated in Fig. 9. Thus, the inlet boundary conditions would correspond to a plane 10  $D_H$  upstream of the spacer grid for the CFD simulations. LDA measurements were taken mainly in the z-direction between the rods in the upper right quadrant of the A-A section (Fig. 9) to obtain the mean axial velocity ( $W$ ) profiles in the rod gaps. The measurement plane A-A is located 10 mm upstream from the end of the rod bundle to minimise any end-effects arising from the proximity of the outlet manifold on the flow characteristics in the bundle. The measurement bands were made as wide as possible, whilst ensuring there was no beam interference due to the proximity of the rods and channel walls.

For the available regions, the measurement resolution was 0.75 mm. The axial velocity contour maps, based on all measured data, are as shown in Fig. 10. The mean velocities and their rms values are normalised with respect to the bulk velocity,  $W_{\text{bulk}}$  (1.50 m/s), and the X-Y coordinate with the rod pitch,  $P$  (33.12 mm). As expected, the peaks in axial velocity occur at or near the centres of the open flow regions, but with some degree of negative bias towards the channel wall due to the shear effect.

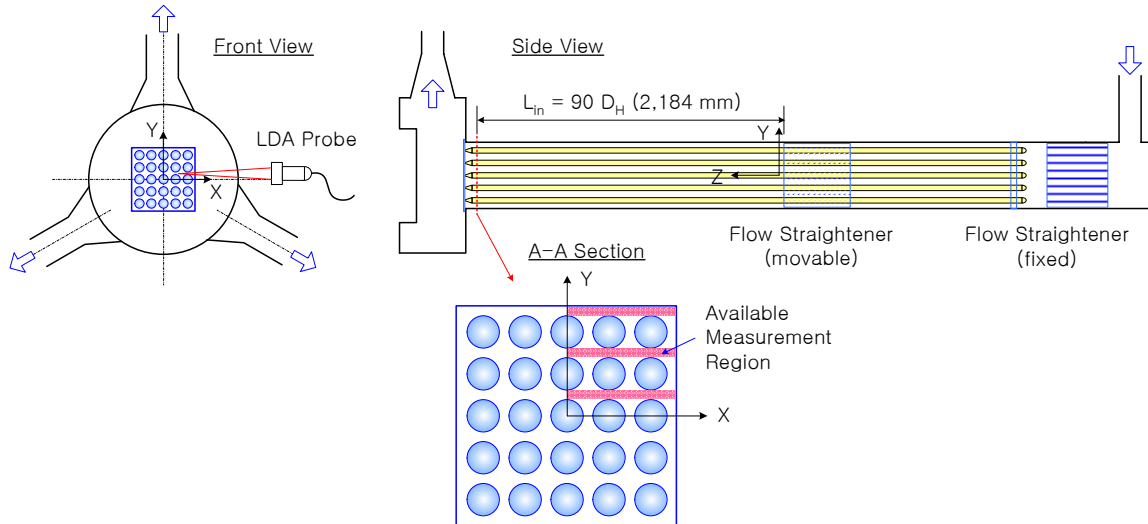


Fig. 9: Layout of the test rig for measuring the inlet boundary conditions.

Three measurement trajectories, those representing the centrelines in each of the three gaps, have been selected to highlight the turbulent properties of the flow. These are shown in Fig. 11. Data collected near the side wall, i.e. for which  $X/P > 2.4$ , though included in Fig. 10 for illustrative purposes, are excluded from Fig. 11, due to the increased uncertainties of the measurements in this region. Elimination of these near-wall data was decided based on the histogram information given in Fig. 8. Figure 11(a) shows the differences in the mean axial velocity profiles along the centrelines for each of the three gaps. The peaks and troughs reflect the free-flow regions and rod blockages, respectively. The turbulence intensity distributions (scaled with respect to the mean axial bulk velocity) shown in Fig. 11(b) are seen to be restricted to the range 5% to 8%. Figure 11(c) shows the presence of small, inwardly-directed cross-flows. The turbulence intensities associated with these cross-flows are at a level of about 5%, as seen in Fig. 11(d).

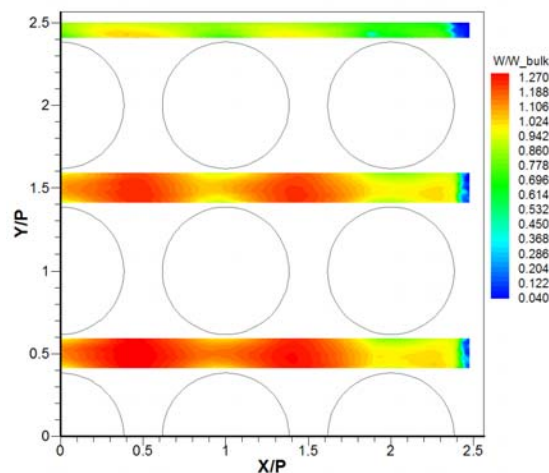


Fig. 10: Contours of mean axial velocity ( $W$ ) in a quadrant section.

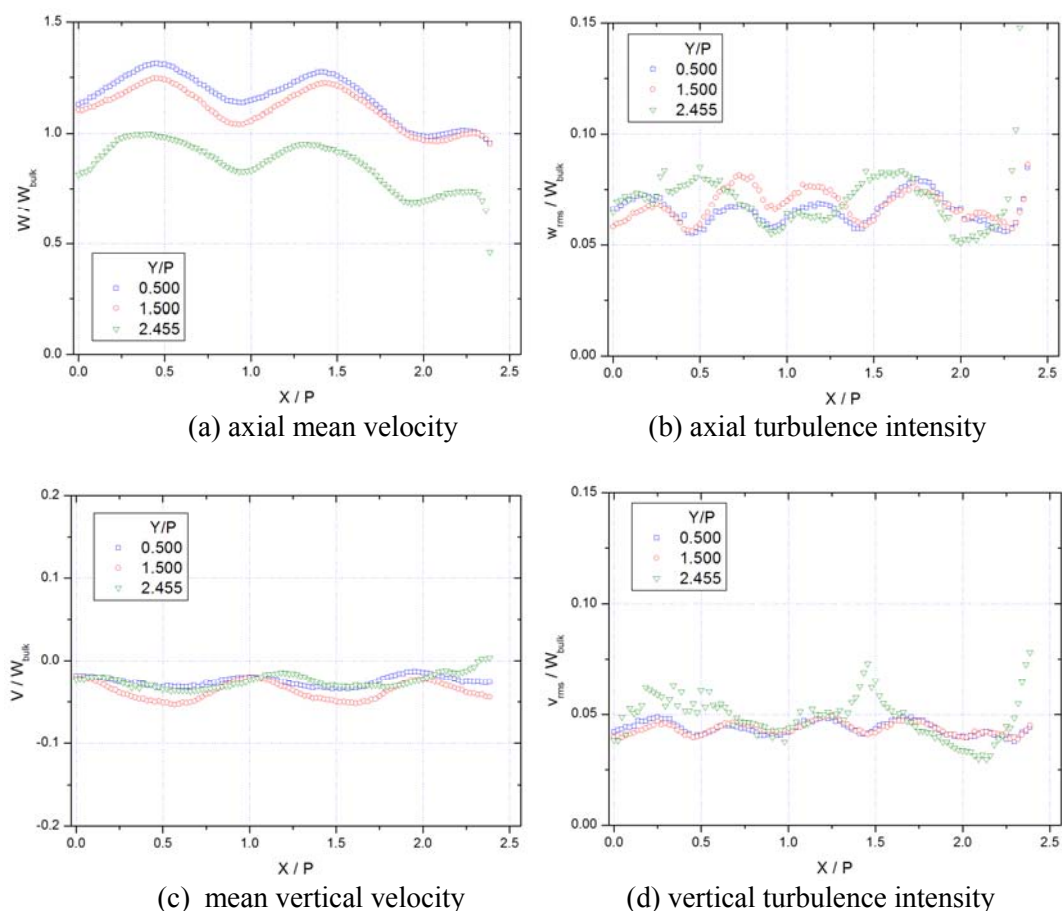


Fig. 11: Flow properties along the centerlines of the three gaps for the upstream test.

All data presented in this document are the property of KAERI, and have been used with their permission.

### 3.6 Downstream Measurements

LDA measurements have been taken at the downstream locations  $Z = 0.5, 1.0, 4.0$  and  $10.0 D_H$  (measured from the vane tips of the spacer grid). For the downstream tests [22], the spacer grid and flow straightener were kept a constant separation of  $100 D_H$ , irrespective of the distance  $Z$  to the measurement plane, by sliding the spacer-grid/straightener assembly lengthwise along the channel; see Fig. 3.

Figure 12 shows the measurement region in the upper right quadrant of the measuring plane A-A, as defined in Fig. 1. Lateral mean velocities  $U$  and  $V$  have been estimated from multiple measurements taken for each downstream distance  $Z$  in the yellow-shaded region shown in Fig. 12(a), which includes sub-channels 1, 2, 3, 5, 6 and 9. For the  $U$  and  $V$  measurements, the LDA probe was placed at the front of the test rig, as shown in Fig. 3. The measurement points are distributed in the yellow region with a spatial resolution of  $0.75$  mm, giving a total of 4173 measurement points altogether. The axial velocity  $W$  is also measured at each downstream distance  $Z$  along the mid-gap lines  $Y/P = 0.5, 1.5, 2.455$ , as illustrated in Fig. 12(b). For this measurement, the LDA probe is located at the side of the test rig, as indicated in Fig. 2. The measurement points here are also distributed with a spatial resolution of  $0.75$  mm along the respective measurement lines.

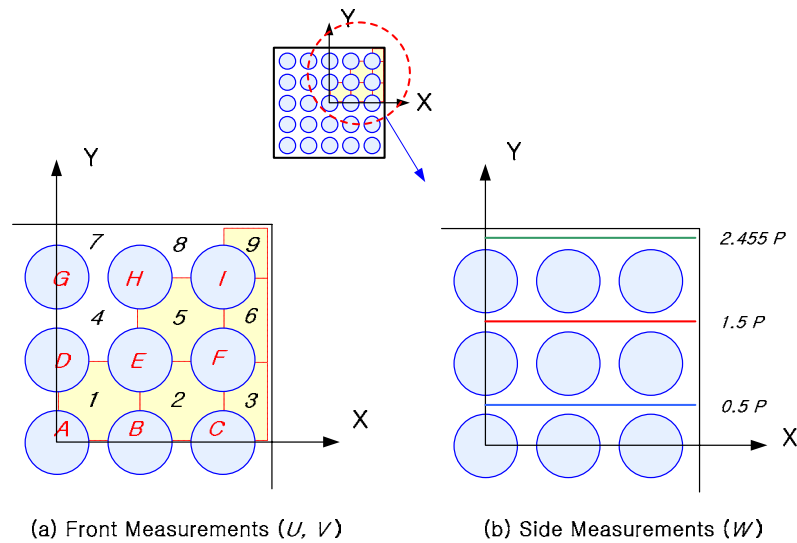


Fig. 12: Measurement region in a quadrant at the measurement section A-A.

### 3.6.1 Lateral Downstream Velocity Measurements

The lateral, or cross-flow, velocities have also been measured at the same four downstream locations. In this case, the LDA probe is placed at the front of the test rig, and scans the measurement region automatically by means of an accurate motorised traversing system. The layout of the test rig and the probe are as shown in Fig. 3. Typical lateral velocity vectors and turbulence intensities (both normalised with respect to the bulk axial velocity,  $W$ ), are mapped over the full measurement region in Fig. 13. Figures 13(a) and 13(b) show results at the downstream distances  $1.0 D_H$  and  $10.0 D_H$ , respectively, for the split-type spacer, while Figs. 13(c) and 13(d) show the same for the swirl-type spacer.

Note that there is a blank zone to the right of rod “F” (c.f. Fig. 12a). Here, the velocity vectors are not presented because of the loss of LDA signals caused by the presence of the solid rib used for fixing the rod in the duct. The vane orientations on the grid strap in the measuring quadrant of the rod bundle are inserted in the upper left corner in each Figure for orientation purposes; the R, L, U and D notations denoting the folding direction of each vane on the grid strap according to Right, Left, Up and Down, respectively. The legend scale for each of the Figures is not the same, but is chosen to present the distributions of the turbulence intensities in an optimal way, depending on their respective maximum and minimum values.

Swirls are generated in the open-flow regions by the vanes of the spacer grids. The shapes of the swirls are more contorted in the case of the split-type spacer, Figs. 13(a) and 13(b), as a consequence of the diagonal vane arrangement, while for the swirl-type spacer, for which the vanes are positioned at each corner of the rod straps (though differently folded), the swirls are more circular in shape, and centrally located. The cross-flow in the rod gaps is more vigorous for the split-type spacer, while the distribution of turbulence intensity ( $u_{rms}$ ) in the sub-channels is flatter in the case of the swirl-type spacer.

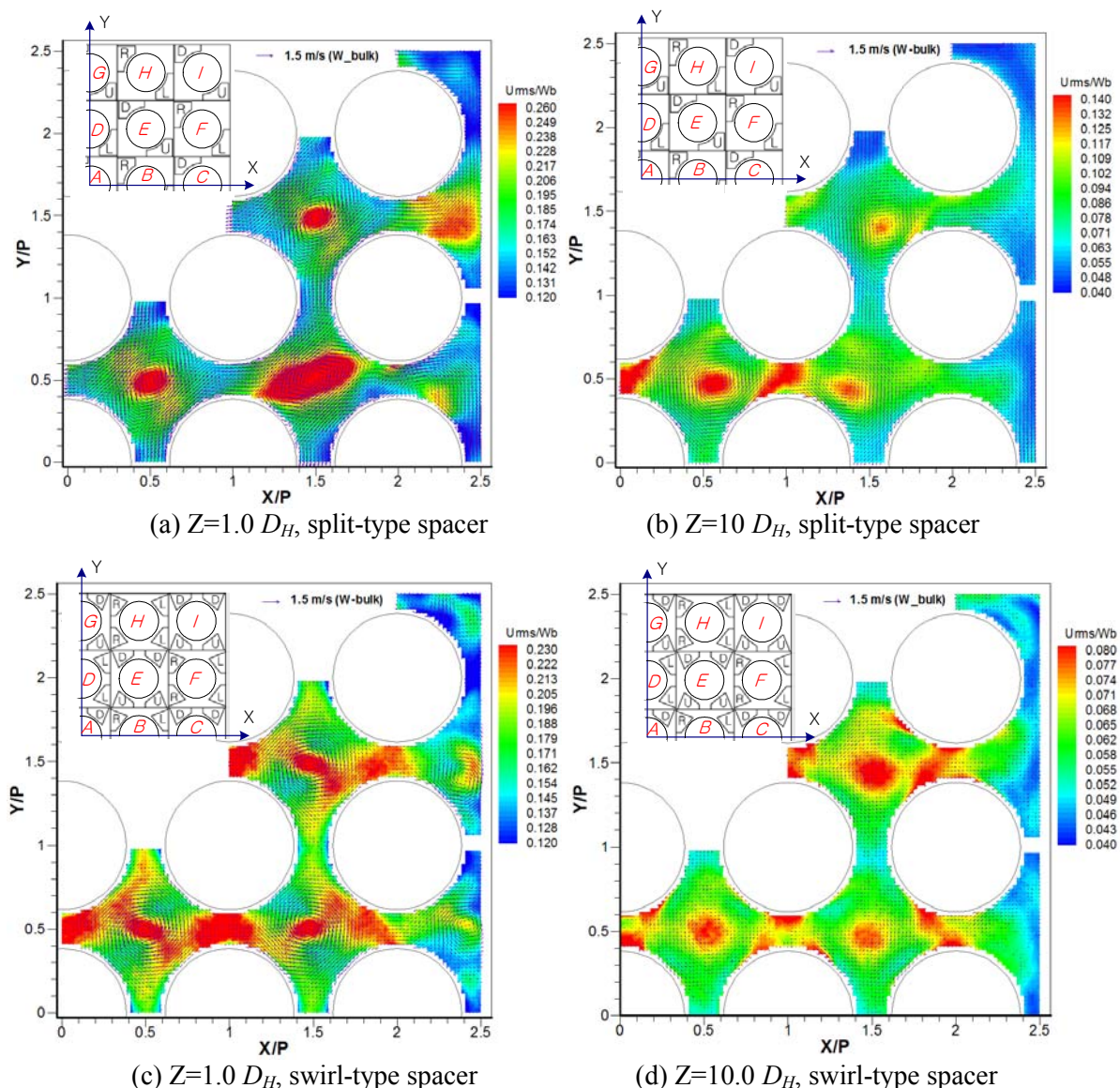


Fig. 13: Lateral velocity vectors  $U, V$  (coloured according to turbulence intensity,  $u_{rms}/W_{bulk}$ ).

Figures 14 and 15 show line profiles of the (normalised) vertical component of the mean velocity ( $V$ ), and the turbulence intensity profiles ( $v_{rms}/W_{bulk}$ ), along the three horizontal gap lines. As can be seen, the magnitudes decay downstream, but at different rates, depending on the spacer type. Also, lateral flow mixing is seen to be more vigorous in the case of the split-type spacer than for the swirl-type spacer.

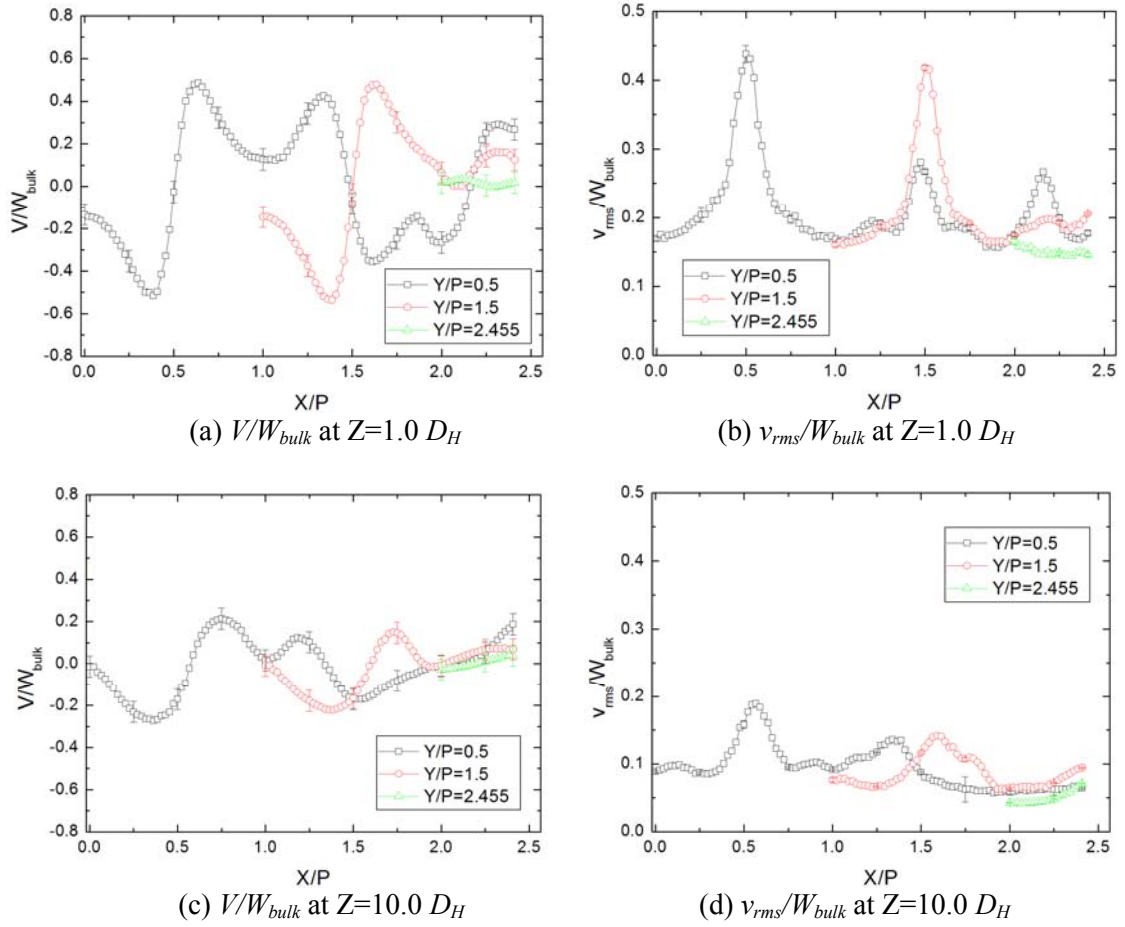
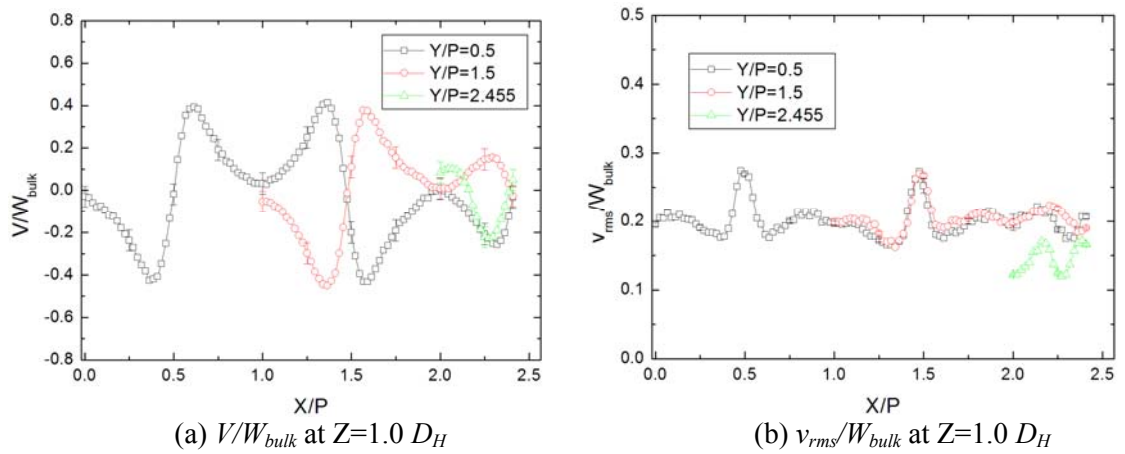


Fig. 14: Profiles of the vertical velocity ( $V$ ) and turbulence intensity ( $v_{rms}/W_{bulk}$ ) along the three gaps for the split-type spacer design



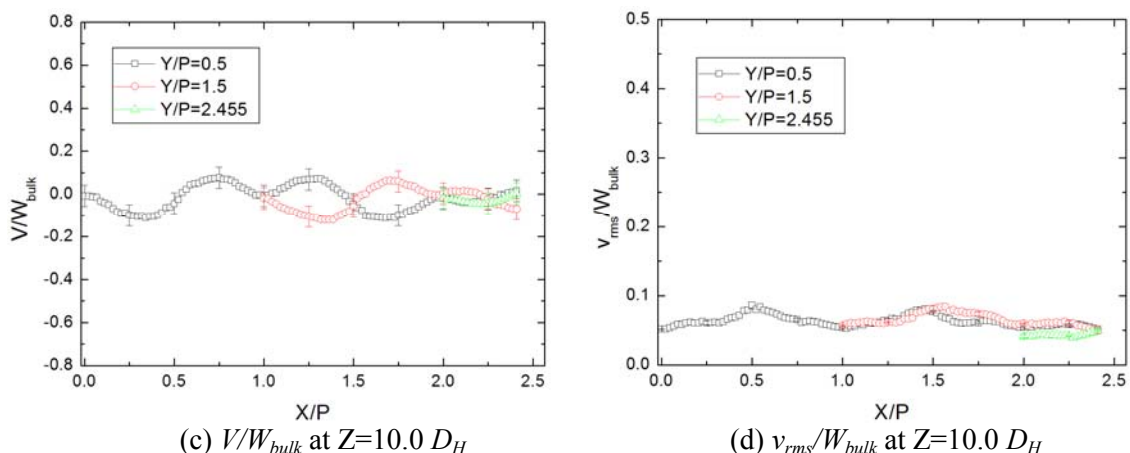
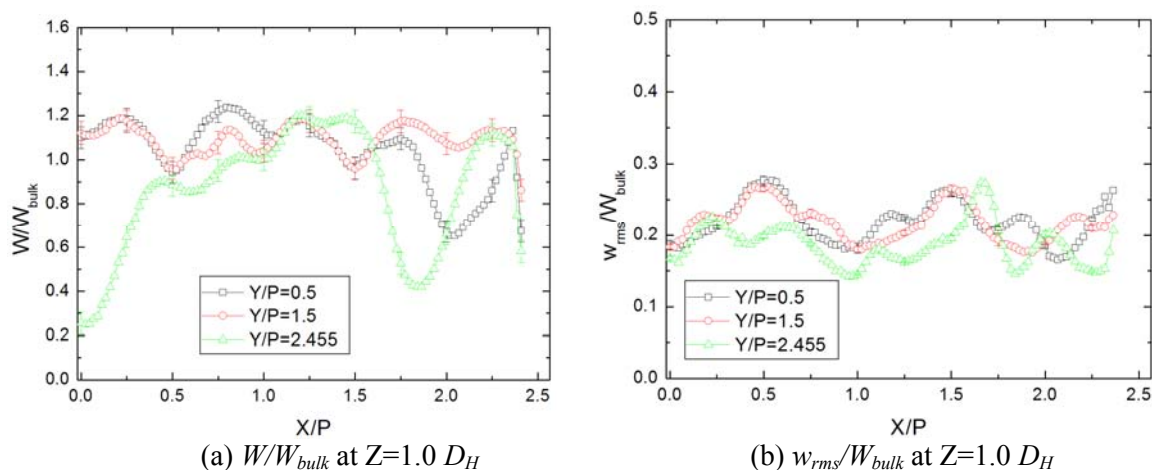


Fig. 15: Profiles of the vertical velocity ( $V$ ) and turbulence intensity ( $v_{rms}/W_{bulk}$ ) along the three gaps for the swirl-type spacer design.

### 3.6.2 Axial Downstream Velocity Measurements

Axial velocities have also been measured. To obtain these data, the set-up of the LDA probe is changed so that the laser beam enters the side of the test rig, as shown in Fig. 2. Velocity signals were taken along the gap centrelines in the measurement region using the automatic traversing system described earlier. Typical mean axial velocity profiles and turbulence intensities are shown in Figs. 16 and 17, respectively. In Fig. 16, which represents the case for the split-type spacer, Figs. 16(a) and 16(b) display profiles of the axial velocity ( $W$ ) and turbulence ( $w_{rms}/W_{bulk}$ ) along the three measuring lines, designated by the Y/P values given in Fig. 12, at the downstream distance  $Z = 1.0 D_H$ , while Figs. 16(c) and 16(d) show corresponding values at  $Z = 10.0 D_H$ .



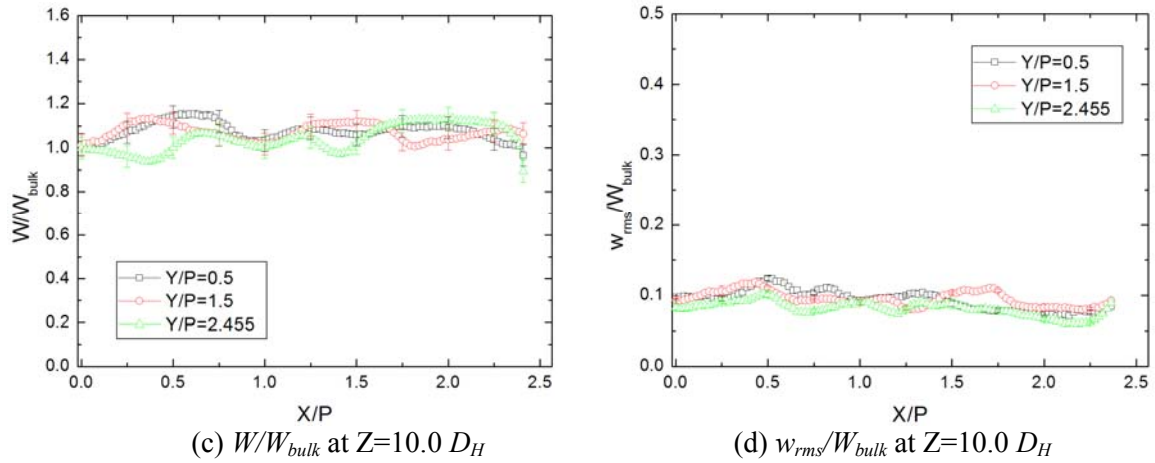


Fig. 16: Profiles of the axial velocity  $W$  and turbulence intensity  $w_{rms}/W_{bulk}$  along the three gaps for the split-type spacer design.

All the distinctive peaks and troughs at  $Z = 1.0 D_H$  have almost decayed completely at  $Z = 10.0 D_H$ . Figure 17 shows the same results as the above for the case of the swirl-type spacer, and these show the same, though not identical trends.

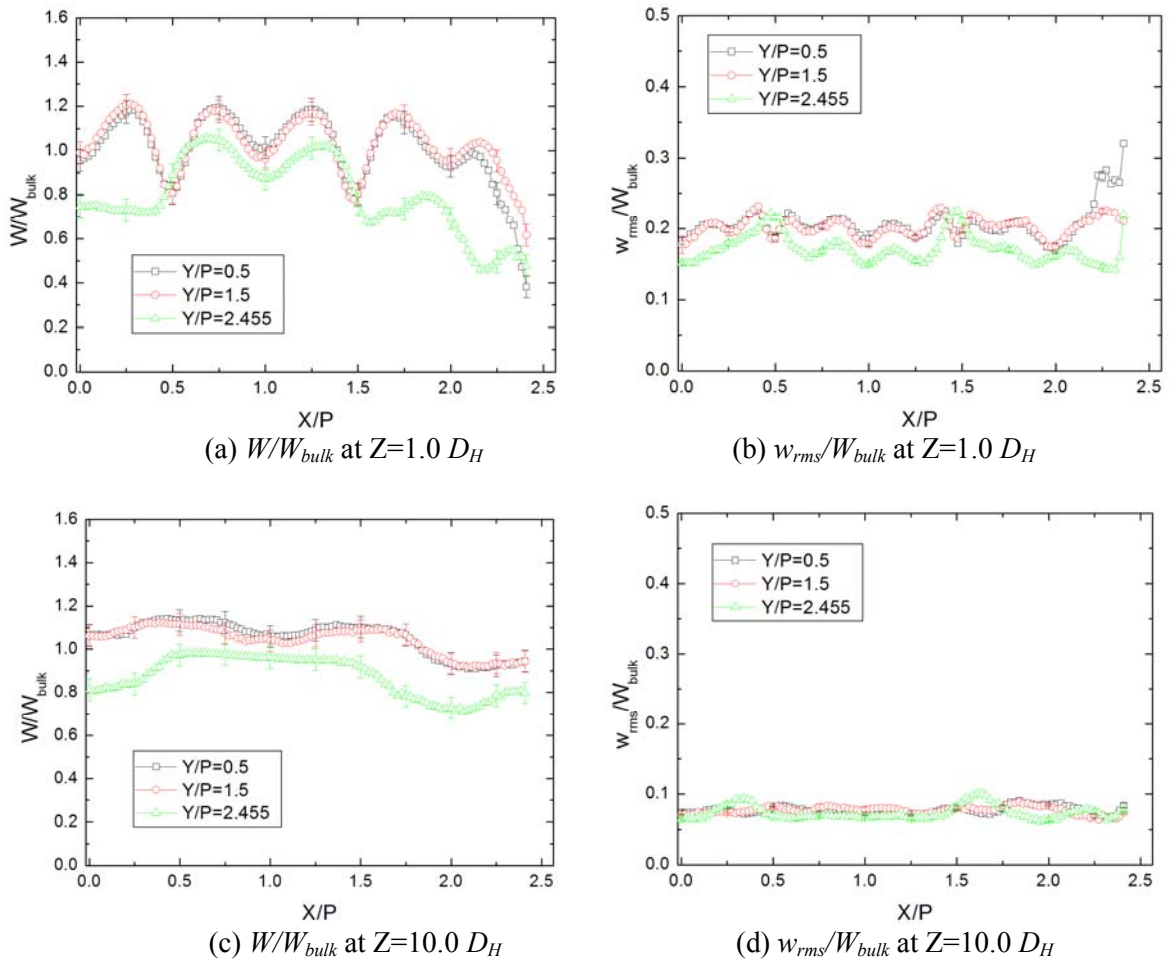


Fig. 17: Profiles of the axial velocity  $W$  and its turbulence intensity  $w_{rms}/W_{bulk}$  at the three gaps for the swirl-type spacer design.

### 3.6.3 Vorticity Contour

Contours of the mean axial component of vorticity in the sub-channels can be constructed from the measured lateral velocity data, the definition of the vorticity being as follows:

$$\omega_z = \frac{\partial v}{\partial x} - \frac{\partial u}{\partial y} \quad (1)$$

Figure 18 shows the distribution of  $\omega_z$  in sub-channels in typical cases for both the split-type and swirl-type spacer designs. Figures 18(a) and 18(c) indicate that the vorticity distribution near the spacer grid is more elliptic for the split-type spacer than for the swirl-type spacer, this as a consequence of the different vane arrangements. For both spacer types, the vorticity strength decays downstream, as can be noted from the legend scales. The vorticity peaks, which appear in the centres of the sub-channels just downstream of the grid spacer for both spacer designs, are seen to migrate towards the adjacent rods further downstream for the split-type spacer, Fig. 18(c), but tend to retain their central positions in the sub-channels in the case of the swirl-type spacer, Fig 18(d).

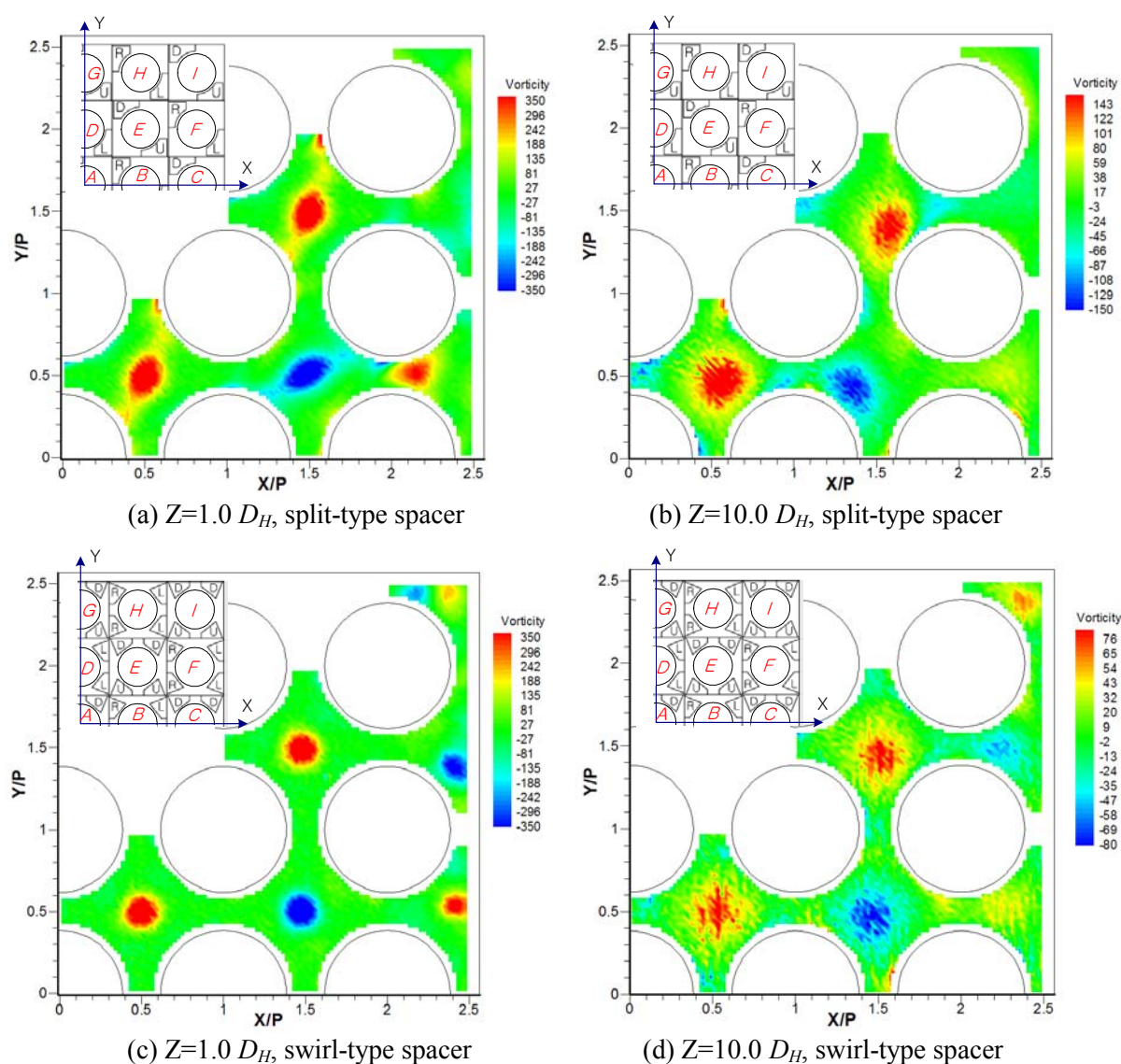


Fig. 18: Vorticity contours of the lateral flow in sub-channels.

### 3.7 Supplementary Experiment: End Effects

Concerns were expressed by some participants at the kick-off meeting that the proximity of the measurement plane to the outlet manifold could have had an effect on the measured values that would be difficult to reproduce in the CFD simulations. Consequently, KAERI performed a number of supplementary experiments in the MATiS-H facility to specifically address this issue [22]. For these tests, the measuring plane (Section A-A in Fig. 19) was moved progressively upstream (away from the outlet manifold) from its standard position 10 mm from the rod tips to 20 mm, 30 mm and 40 mm, progressively. Simultaneously, the spacer grid was also moved to maintain the same 67 mm distance to the measuring plane used in the benchmark tests. These additional tests were carried out for the split-type spacer only.

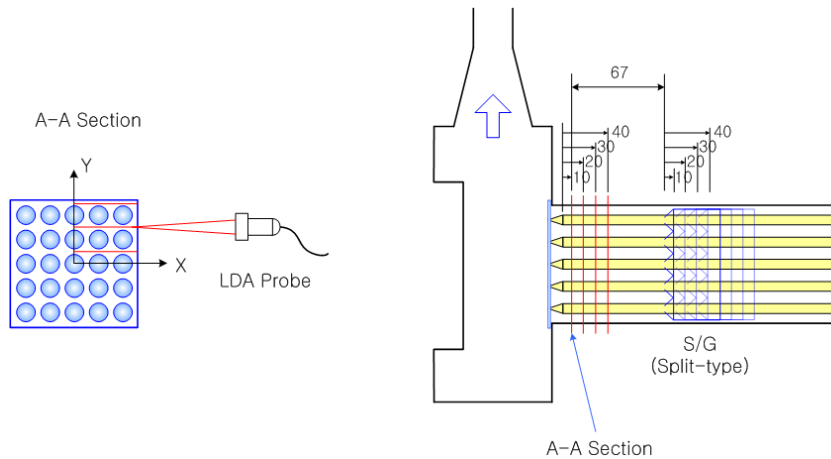


Fig. 19: Layout of the test rig for measuring end effects.

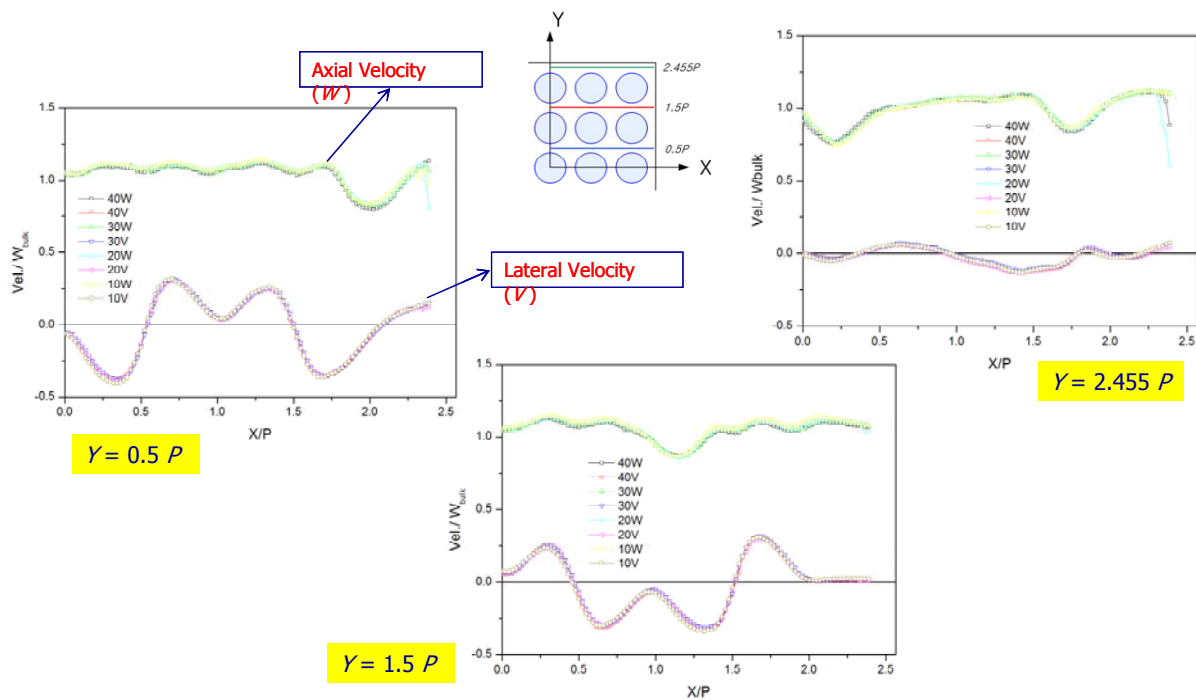


Fig. 20: Comparison of velocity profiles obtained by moving the measuring plane.

Figure 20 shows the effects on the mean axial ( $W$ ) and lateral ( $V$ ) velocity profiles along the measuring lines at  $Y = 0.5 P$ ,  $1.5 P$  and  $2.455 P$  as a consequence of moving the measurement plane

away from the outlet manifold by the designated distances. Apart from some spurious effects close to the channel wall (already alluded to above), the profiles are seen to overlay each other perfectly, confirming that the data from the benchmark tests are free of end-effects caused by the entry of the square section into the outlet manifold assembly. Additional evidence supplied by detailed CFD simulations (not shown here), also performed at KAERI, support these findings.

## 4. COMPUTATIONS

### 4.1 Submissions

As stated above, following the Kick-Off Meeting, there were 48 official registrations made to the NEA secretariat. All subsequently received the Benchmark Specifications and the CAD files of the two spacer grid designs (in various formats). Of these, 25 submitted results before the deadline (which was extended from April 30, 2012 to May 29, 2012 to accommodate some entries for which errors had occurred in the transmission of results). The first submission was received in April 2012, and the last just a few hours before release of the test data on May 30, 2012.

Since not all participants submitted numerical predictions for both spacer types, it is convenient to separate the submissions into those concerned with the split-vane design (Sp) and those for the swirl-type design (Sw). Detailed submission information is described in [23], and summarised in Tables 6-8. Table 6 shows the numerical schemes adopted for the temporal/spatial discretisations for each submission, and the inlet boundary conditions employed. The labels for the split and swirl vane calculations are denoted by Sp01-Sp22 and Sw01-Sw15, respectively. The list reflects the alphabetical order of those who submitted their data, though the names are removed here to maintain anonymity; no ranking of the submissions is implied by the numerical order. Since there are participants who performed a simulation for just one type of spacer design, and others who considered both, the split and swirl labels can differ for the same participant.

Of 25 submissions, five (5) are steady RANS calculations, whereas the rest are URANS or LES calculations. Most of calculations were performed using second-order upwind or central difference schemes for the spatial discretisation. However, two participants applied the more diffusive first-order upwind scheme. The effect of spatial discretisation will be discussed later. For the inlet boundary conditions, only two (2) participants applied the supplementary experimental data provided by KAERI at  $10 D_H$  upstream of the spacer. Others used uniform (top-hat) conditions at an extended distance upstream of the spacer grid (to generate fully-developed profiles), or their own velocity profiles obtained from independent bare rod bundle calculations.

Table 6: Lists of numerical schemes and inlet conditions used.

Label		Numerical Scheme		Inlet Condition
Split	Swirl	Temporal	Spatial	
Sp01		Implicit unsteady	1st	Uniform velocity
Sp02		3rd Runge-Kutta	2nd order centred	Profile from bare rod simulation
Sp03		1st	2nd	Uniform velocity
Sp04	Sw01	-(steady)	2nd	Interpolation with KAERI data
*Sp05		1st implicit Euler	2nd Central difference	Uniform velocity
Sp06	Sw02	2nd implicit Euler	2nd bounded central	Profile from bare rod simulation
Sp07	Sw03	1st	2nd	Uniform velocity
Sp08		-(steady)	2nd	Profile from bare rod simulation

Sp09		- (steady)	2nd (Gauss linear)	Uniform velocity
Sp10	Sw04	2nd	2nd	Profile from bare rod simulation
Sp11	Sw05	2nd	2nd	Profile from bare rod simulation
Sp12		2nd Backward Euler	Central difference	24.2 kg/s with 5% turbulence intensity
Sp13	Sw06	1st	2nd	Uniform velocity
Sp14		2nd Backward Euler	between 1st and 2nd	-
Sp15	Sw07	2nd Backward Euler	Central difference	Profile from bare rod simulation
Sp16		1st	1st	Uniform velocity
	Sw08	3rd order	7th order polynomials	-
Sp17	Sw09	2nd	2nd	Uniform velocity
Sp18	Sw10	- (steady)	2nd	Uniform velocity
	**Sw11	2nd Backward Euler	2nd	Interpolation with KAERI data
Sp19		2nd Backward Euler	2nd	Profile from bare rod simulation
	Sw12	2nd implicit	2nd bounded central	Interpolation with KAERI data
Sp20	Sw13	2nd Backward Euler	2nd	Uniform velocity
Sp21	Sw14	- (steady)	Green-Gauss	Uniform velocity
Sp22	Sw15	2nd	2nd	Full length modelling

\* sub-channel simulation with split vane

\*\* sub-channel simulation with swirl vane

Unlike the earlier T-junction benchmark exercise, in which half the participants chose the LES turbulence model, a variety of models were applied in this benchmark exercise. Table 7 lists the models and wall treatments used. Interestingly, participant Sp06/Sw02 used a hybrid SAS/LES model in which the SAS model was applied for the region upstream of the spacer grid, and LES for the remaining region. As for modelling of the near-wall region, most of commercial code users selected a model provided as a standard user option in the code.

Table 7: Lists of turbulence models and wall treatments used.

Label		Turbulence Model	
		Model	Near-wall
Sp01		k- $\epsilon$	All $y^+$ wall Treatment
Sp02		LES-WALE	Standard wall function (Reichardt)
Sp03		RSM	Blended wall treatment for all $y^+$
Sp04	Sw01	Omega-Based RSM	Standard wall functions
*Sp05		RSM-SSG	Standard wall functions
Sp06	Sw02	SAS & LES	Low Re k- $\omega$ for SAS
Sp07	Sw03	Detached LES	Smagorinsky SGS with damping function, $f(y^+)=1-\exp(-y^+/25)$

Sp08		k- $\epsilon$	Hybrid between high- $y^+$ and low- $y^+$
Sp09		k- $\epsilon$	Standard wall function
Sp10	Sw04	BSLRSM	Automatic wall function
Sp11	Sw05	SST k- $\omega$	Blending function
Sp12		SAS-SST	Automatic wall function
Sp13	Sw06	LES	-
Sp14		SAS-SST	Automatic wall function
Sp15	Sw07	LES-Smagorinsky	Automatic wall function
Sp16		RSM	-
	Sw08	LES, spectral damping	-
Sp17	Sw09	k-w SST	All $y^+$ modelling
Sp18	Sw10	k- $\epsilon$	All $y^+$ wall Treatment
	**Sw11	SST	Standard wall-functions
Sp19		BSL EARSM	Automatic wall function
	Sw12	LES-WALE	Enhanced wall functions
Sp20	Sw13	SST k- $\omega$	Automatic wall function
Sp21	Sw14	SST k- $\omega$	-
Sp22	Sw15	Ideal LES	Scale factor for viscosity calculation

It is well-known that tetrahedral meshing, in combination with a finite-volume solver, leads to excessive numerical diffusion for RANS simulations and loss of kinetic energy for scale-resolving models. However, the convenience of generating tetrahedral meshes within the spacer grid, with its highly complex geometry, was a compelling reason to utilise this type of mesh for this part of the flow domain. In the free-flow region outside the spacer, the more accurate hexahedral mesh structure would be preferred. It is not surprising then, that the majority of submissions featured meshes of this hybrid type. However, for the split-type spacer case, one participant (Sp12) did make the extra effort to construct a fully hexahedral mesh, as did another (Sp05), though in this case the geometry was restricted to four (4) sub-channels. In three (3) submissions (Sp01, Sp08 and Sp17/Sw09), a polyhedral mesh system was used to obtain an advantage of orthogonality of the flow with a relatively small number of control volumes. One submission (Sp07/Sw03) employed a rectangular Cartesian grid, using the immersed boundary method (IBM) to install the vane geometry. Details are listed in Tables 8 and 9, separately for the split-type and swirl-type spacer designs [23]. Note that the  $y^+$  values vary according to the turbulence model.

Table 8: Mesh information for the split-vane simulations.

Label	Type	Mesh (million)	$y^+$	Min. cell edge length (mm)	Max. cell edge length (mm)
Sp01	Polyhedral	3.3	0.1-36	0.023	3.3
Sp02	Tetrahedral	54	30-	0.5 (normal to pin)	1.5 (parallel to pin)
Sp03	Hexahedral/Tetrahedral	107.6	3-32	0.225 (on tip) / 0.4 (downstream)	0.8
Sp04	Tetrahedral	22.5	1-52.8	0.1	4.4
Sp05*	Hexahedral	20	2-89	0.084	0.816
Sp06	Hexahedral/Tetrahedral	22.2	0.7-4.7	0.04	3.24
Sp07	Cartesian, Immersed	30	5-15	0.3	0.5

	Boundary Method				
Sp08	Polyhedral	9	0.05-7	0.5	1
Sp09	Hexahedral/Tetrahedral	14.3	2-140	0.36	6.49
Sp10	Hexahedral/Tetrahedral	96.3	0.18-7.06	0.105	1.023
Sp11	Hexahedral/Tetrahedral	96.3	0.07-5.11	0.105	1.023
Sp12	Hexahedral	13.1	0.16-87.03	0.227	81.8
Sp13	Hexahedral/Tetrahedral	8	1.8-4.3	0.1 (transverse) / 0.8 (longitudinal)	1.6 (transverse) / 3.6 (longitudinal)
Sp14	Tetrahedral	6.5	4.49-149	1.05	3.6
Sp15	- (Unstructured)	25.5	0.06-2.98	0.0085	0.9
Sp16	Hexahedral/Tetrahedral	15.3	4-30	0.1	4
Sp17	Polyhedral	48.8	0.005-37.5	0.002	0.5
Sp18	trimmer with prism layers	64.1	0.02-2	0.02	0.5
Sp19	Hexahedral/Tetrahedral	22.7	6.02-177.8	0.33	2.325
Sp20	Hexahedral/Tetrahedral	68	0.43-29.57	0.14	1.76
Sp21	Hexahedral/Tetrahedral	68	0.21-31.31	0.14	1.76
Sp22	Hexahedral/Tetrahedral	144	-	0.1	1.5

\* Reduced geometry simulation with periodic boundary conditions.

According to Best Practice Guidelines [3], every CFD simulation should be accompanied by a mesh-convergence study to minimise numerical error. Though no specific requirement was made in this benchmark exercise, it was assumed by the organisers (perhaps wrongly) that such a study would be carried out, since each participant was instructed to submit what he regarded as his “best” simulation, and only one data set would be accepted for synthesis. In addition, at the time the Benchmark Specifications (Annex 2) were distributed, the participants were not informed that their identities would be kept secret (this was not done for the T-junction Benchmark). These two factors were considered to provide sufficient inducement to participants to perform a mesh-convergence study ahead of submission of their results. However, it might be wiser to request details of this directly, and such a requirement will be considered in future benchmark exercises in this series.

Table 9: Mesh information for the swirl-vane simulations.

Label	Type	Mesh (million)	Y+	Min. cell edge Length (mm)	Max. cell edge Length (mm)
Sw01	Tetrahedral	27	1.2-46.9	0.1	4.4
Sw02	Hexahedral/Tetrahedral	20.6	1.3-11.0	0.07	3.24
Sw03	Cartesian, Immersed boundary Method	30	5-15	0.3	0.5
Sw04	Hexahedral/Tetrahedral	108.7	0.28-4.87	0.068	0.866
Sw05	Hexahedral/Tetrahedral	108.7	0.06-3.16	0.068	0.866
Sw06	Hexahedral/Tetrahedral	8	1.7-4.6	0.1 (transverse)	1.6 (transverse) /

				/ 1.1 (longitudinal)	3.6(longitudinal)
Sw07	- (Unstructured)	26	0.09- 2.73	0.0085	0.9
Sw08	- (Unstructured)	0.7	-	-	-
Sw09	Polyhedral	62.8	0.001- 14	0.002	0.485
Sw10	Trimmed with prism layers	64.7	0.02-2	0.2	0.5
Sw11**	Tetrahedral	3	3-65	0.26 (transverse) / 1.0 (longitudinal)	0.7 (transverse) / 1.0 (longitudinal)
Sw12	Hexahedral/Tetrahedral	110	0.5-25.0	0.02	1.0
Sw13	Hexahedral/Tetrahedral	65	2.74- 27.31	0.14	1.76
Sw14	Hexahedral/Tetrahedral	65	0.35- 32.71	0.14	1.76
Sw15	Hexahedral/Tetrahedral	47	-	0.1	1.5

\*\* Reduced geometry simulation with periodic boundary conditions.

## 4.2 Codes and Models

Of the 25 submissions, five (5) used a standard, steady-state Reynolds-Averaged Navier Stokes (RANS) turbulence model, ten (10) used the unsteady URANS form of the model, four (4) used a hybrid model, while the remaining six (6) employed some form of Large Eddy Simulation (LES). Table 10 provides some more details, and complete information may be found in [23].

Table 10: Summary of turbulence models employed.

Item	Description			
Submissions	25			
Solver	Commercial: 19 (ANSYS-CFX, FLUENT, STAR-CCM+)			
	Others: 6			
Model		$k-\varepsilon$	SST $k-\omega$	RSM
	RANS (5)	3	1	1
	URANS (10)	1	4	5
	Hybrid (4)	SAS-SST	DES	SAS/LES
		2	1	1
LES: 6				
Mesh	Number: 0.7 M – 144 M			
	Type	Hexahedral / Tetrahedral (for most cases)		
		Polyhedral (only in the case of STAR-CCM+)		

### 4.3 Data Requested

It was hoped that most participants would submit calculated results for both the split-type and the swirl-type spacer grid geometries, though it was made clear that results for just one type would be accepted, and included in the synthesis. For participants who wished to submit results for just one type, the split-type spacer grid was recommended. This recommendation was generally adhered to: in fact, of the 25 submissions received, ten (10) referred to the split-type spacer design only, three (3) to the swirl-type design only, while twelve (12) addressed both designs.

Only very basic quantities were requested, to permit flexibility in the choice of summary results, and to ensure uniform processing of the results. These were time-averaged mean and rms velocities in all coordinate directions at four (4) specified downstream locations. One exception was that the circulation in a specified sub-channel (that is, the integral of the longitudinal component of vorticity over the sub-channel cross-sectional area) was also requested, to give a measure of the capability of the simulations to capture, in an integral sense, the degree of swirl generated in the sub-channel by the vanes of the spacer grid.

From the lessons learned from the first CFD benchmark exercise, expounded by J. H. Mahaffy (JHM) in his invited lecture at the CFD4NRS-3 workshop [24], the Python [25] script, which had been prepared by KAERI in collaboration with JHM to aid the synthesis of the simulation data, was distributed to all participants in advance, and it was their responsibility to ensure that their data files could be successfully read by the script ahead of formal submission to the benchmark organisers. This cautionary procedure proved very successful in all but one case, for which the participant had no access to the Python code. Countless hours of frustration were saved by this simple expedient, which also serves as a lesson for future benchmark exercises in the series.

### 4.4 Unofficial Additional Information: CAD File of MATiS-H

At the kick-off meeting in May 2011, several delegates expressed concern that the proximity of the measuring plane to the outlet manifold (see Fig. 3) might have a back influence on the measured quantities that would be difficult to quantify if a simple outlet condition at the end of the test section was adopted for the CFD calculations. This point was taken up for further investigation by KAERI, in which new experiments in the MATiS-H facility were organised (see Section 3.7).

An independent initiative was taken by a group at EU JRC Petten in the Netherlands<sup>‡</sup> to produce a CAD file of the entire MATiS-H test rig (which did not previously exist), which would include details of the inlet and outlet manifolds, to serve as an aid to mesh construction for those who wished their CFD model to extend beyond the immediate upstream and downstream regions of the spacer. The CAD model was subsequently sent to the staff at KAERI for evaluation, whose staff corresponded directly with JRC on the details. It was made clear by the benchmark organisers that this additional information was not to be considered part of the official specifications, and the point was also made by KAERI that though the CAD file had not been subject to a strict quality assurance procedure, it had been examined carefully. On this basis, the CAD file was distributed to all registered participants, to be used at their discretion. An image of the MATiS-H test section, including inlet and outlet manifolds, generated directly from the CAD file is shown in Fig. 21. One participant used this information to construct the mesh used for his numerical simulation.

---

<sup>‡</sup> Thanks are due to H. Wilkening, K. Tucek, P. Green and A. Grah of EU JRC, Petten, NL.

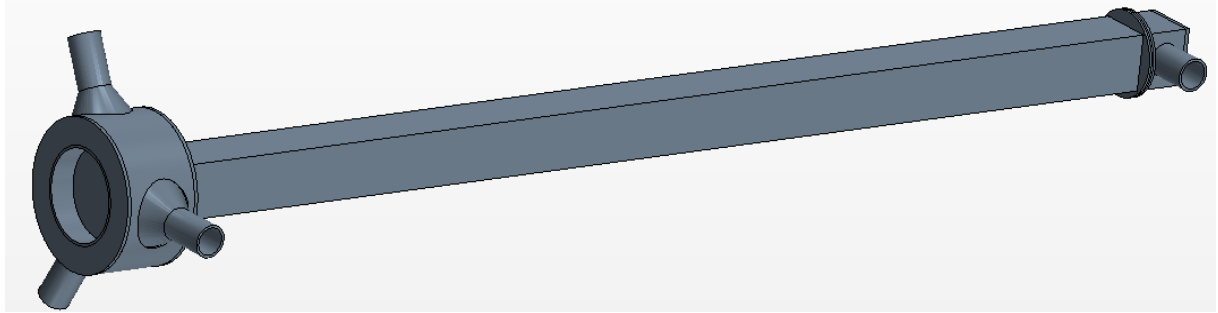


Fig. 21: Computer-generated image of MATiS-H derived from the JRC CAD file.



## 5. SYNTHESIS OF RESULTS

### 5.1 Introduction

As mentioned previously, it was intended for all data reduction and plotting to be accomplished using a Python script [25] to control the total level of effort involved. The script previously used by J. H. Mahaffy for the T-junction benchmark [10,11,24] was used as a basis for this, modified appropriately (by KAERI), and, with the cooperation of the original author, used to read the data requested from the participants. Many man-hours were saved by this simple expedient.

The synthesis was undertaken jointly by J.R. Lee, J. Kim and C.-H. Song of KAERI. Their findings were presented in the form of an invited paper [23] at the CFD4NRS-4 Workshop (co-sponsored by the OECD and IAEA), which took place in Daejeon, S. Korea from Sept. 10-12, 2012, and is included in the official proceedings. This report is an exhaustive analysis of the benchmark submissions, and can stand separately to the information contained in this Section. In addition, detailed descriptions of calculation results and corresponding explanations are contained in selected papers presented at the CFD4NRS-4 workshop, the official proceedings from which are due to be distributed in the first half of 2013. Subsequently, only highlights of the overall synthesis are presented here.

### 5.2 Available Data

Following the signing of a confidentiality agreement, each participant in the benchmark exercise received directly from KAERI the following three types of experimental data at the three different elevations  $Y/P = 0.5, 1.5$  and  $2.455$  for each of the four axial locations  $Z = 0.5 D_H, 1.0 D_H, 4.0 D_H$  and  $10.0 D_H$  downstream of the spacer grid:

- Time-averaged values for all three velocity components (U,V,W) for each measuring plane;
- Time-averaged rms values of the fluctuating components ( $u',v',w'$ ) of all three velocity components;
- Circulation in one specified sub-channel (see Annex 2),  $\Gamma = \iint \omega_z dx dy$ , where  $\omega_z$  is the z-component of vorticity.

### 5.3 Inlet Flow Conditions

At the kick-off meeting of the benchmark exercise, there were questions raised on what inlet conditions would be most appropriate. As explained in Section 3.7, KAERI did perform supplementary tests in the MATiS-H facility specifically to provide mean velocity profiles and turbulence intensities at a distance  $10 D_H$  upstream of the spacer grid. These were distributed to all registered participants in addition to the official benchmark specifications, and indeed used in some of the simulations. Other participants ran an independent simulation without the spacer grid to produce fully developed profiles, which were then adopted as the boundary conditions for the simulations including the spacer grid. However, most opted for simple uniform profiles (usually the default option in commercial codes). Table 11 gives a breakdown of the inlet conditions adopted [23]. Even though different types of inlet boundary condition were applied in this exercise, detailed comparisons

revealed that the effect on downstream predictions was small, presumably because the velocities and turbulence levels are completely regenerated by the spacer.

Table 11: Classification of inlet conditions used for the calculations.

Type of Inlet Condition	Split vane case (Sp)	Swirl vane case (Sw)
Uniform flow	01, 07, 09, 12, 13, 16, 17, 18, 20, 21, 22	03, 06, 09, 10, 13, 14, 15
Profile from bare rod simulation	02, 06, 08, 10, 11, 15, 19	02, 04, 05, 07
KAERI-supplied data	04	01, 12

#### 5.4 Metric for Comparison

A very simple linear metric was chosen to compare the relative quality of the time-averaged velocity profiles produced by the CFD calculations [23]:

$$M = \frac{1}{N} \sum_{i=1, N} |C_i - D_i| \quad (1)$$

where  $N$  is the total number of discrete values along the curve, as requested in the Benchmark Specifications (Annex 2),  $C_i$  is the  $i^{\text{th}}$  result from the CFD calculation and  $D_i$  is the measured value at the same location. Since the measured velocity profiles across the channel width are more complex in the present case, with multiple peaks and troughs, other more sophisticated options for a suitable metric were explored, but found to be unnecessary.

The metric was applied separately to the split-type and swirl-type numerical data, and time-averaged values for the velocity components and the time-averaged rms values of their fluctuating components at one elevation,  $Y = 0.5 P$  in Fig. 12(b), were used for comparison, this elevation representing a typical sub-channel flow region in a rod bundle, free from near-wall distortions. Of all the four measurement planes in the axial direction, those at  $1.0 D_H$  and  $4.0 D_H$  were chosen for comparing calculation with experiment, because the most vigorous vortex behaviour is seen at  $1.0 D_H$  downstream of the spacer grid, and the most noticeable decay in turbulent kinetic energy was observed to exist up to the measuring station at  $Z = 4.0 D_H$ .

Metrics were generated for all benchmark submissions using all comparisons of time-averaged velocity components, rms-velocity fluctuations and circulation (in the specified sub-channel), as previously described. For the comparisons, the 25 submissions were assigned a ranking directly from the application of the metric, from 1 (lowest metric value) to 22 (highest metric value) for the split-type spacer, and from 1 (lowest metric value) to 15 (highest metric value) for the swirl-type spacer, appropriately. This process was separately repeated for each component of the time-averaged mean velocity at the two measurement locations, each component of the time-averaged rms value of the velocity, and the circulation in the specified sub-channel.

#### 5.5 Rankings for Split-Type Spacer Simulations

##### 5.5.1 Mean Velocities

The final rankings [23] for comparisons based on mean velocity for the split-type spacer at the two downstream locations  $Z = 1.0 D_H$  and  $Z = 4.0 D_H$  are given in Table 12. A separate analysis [23] has revealed that the rankings in the two planes is not strongly correlated, indicating that a submission with good agreement against measured data at  $Z = 1.0 D_H$  does not necessarily imply good agreement

at  $Z = 4.0 D_H$ . For example, Sp13 is ranked in 3<sup>rd</sup> place at  $Z = 1.0 D_H$ , but 10<sup>th</sup> at  $Z = 4.0 D_H$ . However, the same analysis has revealed that the rankings are more closely correlated for the time-averaged rms values. The submissions shown in red (Sp09, Sp17, Sp19, Sp12, Sp15) in Table 12 are the most highly ranked for their respective turbulence model groups, as listed in Table 7. Note that the simulation chosen to represent the Reynolds Stress Model (RSM) group is Sp19, which features the Baseline Explicit Algebraic version of the RSM model (BSL EARSM). In this model, the shear-stress components are not calculated explicitly using transport equations, as it is in the differential versions of the RSM model, but derived algebraically from a basic two-equation Eddy Viscosity Model (EVM) approach. Indeed, some authors consider the model to be more accurately described as a Non-Linear Eddy Viscosity Model (NLEVM), and has been used successfully [26] in other rod-bundle simulations.\* In this application, better results were obtained using this pseudo-RSM model than those produced using conventional RSM approaches (Sp03, Sp10, Sp16), so has been adopted in this document as the “flag bearer” of the RSM approaches. Note also that Sp12, which employs the SAS-SST turbulence model, is ranked very highly at both downstream locations, in stark contrast to its performance for the T-junction benchmark [24].

Table 12: Ranking according to time-averaged mean velocities for the split-type spacer.

$Z = 1.0 D_H$			$z = 4.0 D_H$		
Rank	Score	Submission	Rank	Score	Submission
1	13.41	<b>Sp12</b>	1	11.58	<b>Sp19</b>
2	14.89	<b>Sp19</b>	2	12.02	<b>Sp09</b>
3	16.01	Sp13	3	12.75	Sp06
4	17.18	Sp16	4	13	<b>Sp12</b>
5	18.91	<b>Sp15</b>	5	14.13	<b>Sp15</b>
6	19.39	<b>Sp17</b>	6	14.27	Sp02
7	19.95	Sp02	7	14.63	Sp18
8	20.21	Sp14	8	16.41	<b>Sp17</b>
9	20.47	Sp22	9	16.53	Sp01
10	23.65	<b>Sp09</b>	10	17.33	Sp13
11	23.89	Sp06	11	17.47	Sp11
12	24.2	Sp01	12	17.82	Sp08
13	25.5	Sp18	13	18.9	Sp20
14	26.17	Sp08	14	20.75	Sp07
15	28.26	Sp11	15	21.19	Sp21
16	28.66	Sp03	16	21.51	Sp16
17	30.35	Sp10	17	21.78	Sp03
18	32.22	Sp07	18	23.39	Sp10
19	47.32	Sp04	19	24.84	Sp14
20	48.79	Sp20	20	33.44	Sp22
21	54.64	Sp21	21	34.5	Sp04

\* The authors are grateful to E. Baglietto for clarifying this point.

### 5.5.2 Time-Averaged RMS Velocities

Ranking tables for the time-averaged rms velocity data pertaining to the split-type spacer design have also been produced. The rms data from the 2-equation RANS models obtained under steady-state conditions was obtained from the turbulent kinetic energy, and is the same for all component directions, given the implied isotropy in the model. Most participants supplied these data as such, and in the requested format.

Table 13 shows the ranking according the rms data for the split-type spacer grid. The ranking is obtained by separately applying the metric above to each velocity component, at the discrete points requested in the Benchmark Specifications, and summing to obtain an overall score. This procedure is followed separately for data presented in each of the measuring planes  $Z = 1.0 D_H$  and  $Z = 4.0 D_H$ . No attempt has been made to normalise the scores, a procedure that would anyway not affect the rankings. Examining Table 13 in conjunction with Table 12, which gives the rankings for the mean velocities, provides a good measure of overall performance. Quantitative rankings produced on this basis are given in Section 5.5.6.

Table 13: Ranking according to time-averaged rms velocities for the split-type spacer.

Z=1.0 D <sub>H</sub>			Z=4.0 D <sub>H</sub>		
Rank	Score	Submission	Rank	Score	Submission
1	4.16	Sp12	1	2.21	Sp06
2	7.64	Sp07	2	3.23	Sp07
3	8.38	Sp19	3	3.84	Sp12
4	9.79	Sp17	4	3.95	Sp19
5	10.36	Sp15	5	6.5	Sp18
6	11.3	Sp11	6	6.84	Sp15
7	11.59	Sp06	7	7.06	Sp03
8	12.05	Sp18	8	7.41	Sp11
9	17.94	Sp03	9	9.37	Sp17
10	18.66	Sp09	10	9.8	Sp09
11	23.33	Sp08	11	10.32	Sp08
12	24.19	Sp10	12	15.34	Sp01
13	27.62	Sp14	13	15.8	Sp10
14	28.18	Sp01	14	17.38	Sp14
15	28.88	Sp02	15	18.35	Sp22
16	32.77	Sp16	16	18.75	Sp02
17	35.32	Sp20	17	21.07	Sp16
18	35.54	Sp22	18	25.18	Sp20
19	39.29	Sp04	19	25.96	Sp04
20	39.31	Sp13	20	25.98	Sp13
21	39.44	Sp21	21	26.03	Sp21

The calculation results were examined from many different viewpoints, taking account of the fact that various types of turbulence model and mesh distribution had been employed [23].

- Best estimation for different turbulence models;
- Effect of turbulence model;
- Effect of spatial discretisation;

- Effect of simulating selected sub-channel(s) using periodic boundary conditions.

For the discussion here, only the first and last points on the above list are highlighted. Many more details are given in the synthesis report [23].

### 5.5.3 Best estimation for different turbulence models

For this comparison, the best estimation for each type of turbulence model according to the ranking given in Table 13 was selected: that is, Sp09 for  $k-\varepsilon$ , Sp17 for  $k-\omega$ , Sp19 for RSM, Sp12 for hybrid, and Sp15 for LES. Submission Sp09 is a steady-state simulation, whereas the others are unsteady. In these calculations, either a uniform velocity profile or one derived from an independent bare rod bundle simulation were used as inlet boundary conditions; details are given in Table 6. The number of control volumes employed ranges from 3.3M to 144M, with most of the submissions falling in this range 13M to 48M.

Figure 22 shows the cross-sectional mesh distributions for four (4) of the five (5) best predictions for each turbulence group. It is noted that a fine mesh is employed in the core region of the sub-channel, where vortices are expected, as well as in the near-wall region to capture boundary-layer effects. Since this synthesis mainly focuses on information along the centreline of a sub-channel, the mesh concentration into the core region would be an important factor.

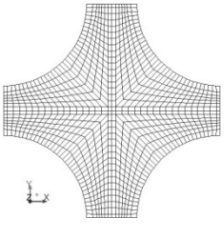
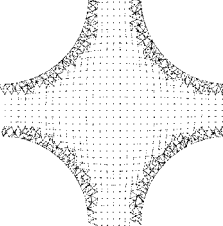
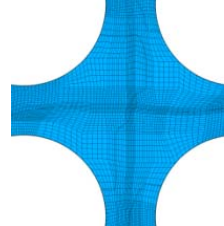
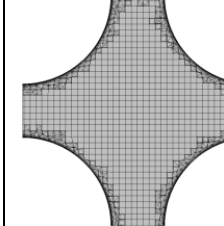
	k- $\varepsilon$ 14.3M (Sp09)	RSM 22.7M (Sp19)	Hybrid 22.7M (Sp12)	LES 25.5M (Sp15)
Mesh Distribution				

Fig. 22: Mesh distributions for the leading cases for each turbulence model.

By way of illustration only, Fig. 23 shows a comparison of the mean and rms  $u$ -velocity profiles at  $Y = 0.5 P$  for  $Z = 1.0 D_H$  for the five (5) selected cases. A strong lateral flow would be anticipated at about  $X = 1.0 P$  and  $X = 2.0 P$ , which are the regions between the rods E-H and F-I, respectively. Both are well predicted, with a tendency for slight overprediction of peak values. The additional peak near the channel wall ( $X/P = 2.25$ ) is more difficult to understand, and is not in accord with experiment. Again, as might be anticipated, peak rms values would appear in the mid-channel locations  $X = 0.5 P$  and  $X = 1.5 P$ , and all simulations qualitatively capture this trend. In quantitative terms, the Hybrid SAS-SST results (Sp12) reproduce the amplitudes of the peaks very well, but there is a clear over-smoothing effect with the  $k-\varepsilon$  model. For the other models, apart from the RSM model, there is a tendency to underpredict the peak at  $X = 0.5 P$  but reproduce the second peak at  $X = 1.5 P$  quite well.

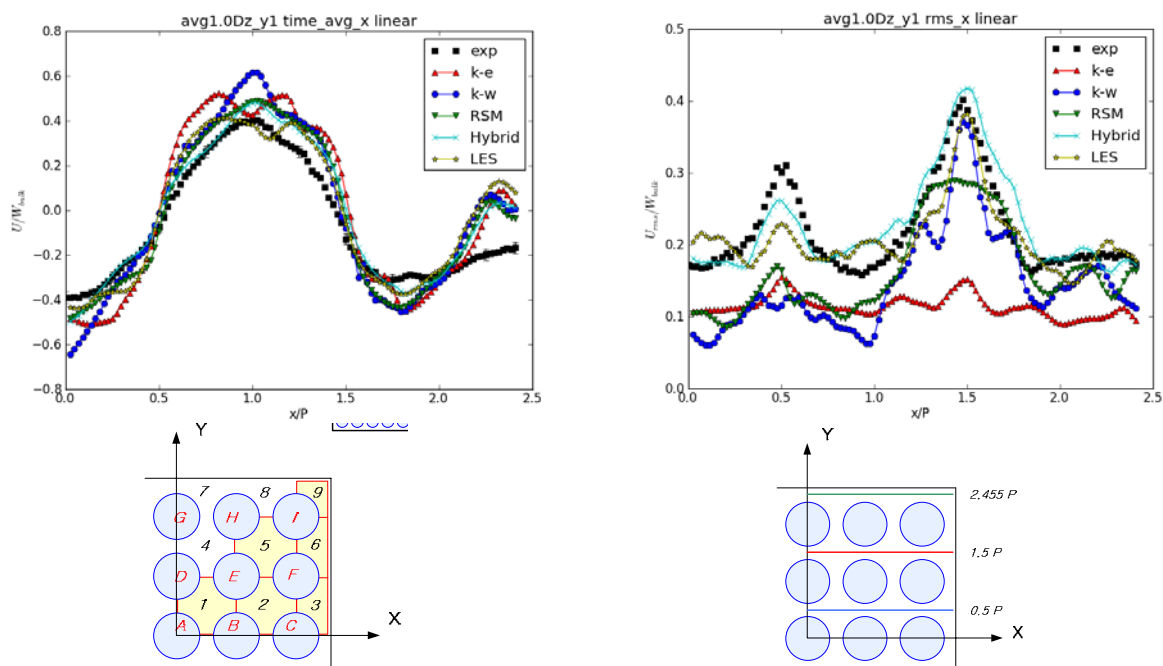


Fig. 23: Mean and rms  $u$ -velocity components at  $Z = 1.0 D_H$ .

Looking at the profiles of the  $v$  and  $w$  components of velocity at the  $Z = 1.0 D_H$  downstream location (not shown here), similar trends may be noted. Further downstream, the SAS-SST model continues to perform well, while for the 2-equation RANS models,  $k$ - $\epsilon$  and  $k$ - $\omega$ , the rms values are too small, indicating a too rapid turbulence decay, even though the mean profiles remain quite acceptable. The RSM model does somewhat better, but best comparisons are obtained using the SAS-SST and LES models. A more in-depth analysis is contained in the official synthesis report [23].

It should be emphasised that this is not a straight comparison of turbulence models, since each participant adopted quite different mesh discretisations. The benchmark analysts make the point [23] that perhaps part of the success of the SAS-SST model in this application is due to the extra effort made to produce a hexahedral mesh over most of the flow domain. There is also the issue of the time discretisation. Submission Sp09 utilised the  $k$ - $\epsilon$  turbulence model, and was run as a steady-state calculation. This means that the rms values could only be derived from the turbulent kinetic energy,  $k$ , assuming isotropy. The Sp09 results are clearly over-diffusive for the rms values. In contrast, the other simulations were run as unsteady calculations, and the time-averaging was undertaken statistically using the transient data. Even for submission Sp17, which employed the  $k$ - $\omega$  turbulence model, also isotropic, results were an improvement over those of Sp09. Submission Sp19, which employed the anisotropic RSM model, showed little improvement over Sp17; both were run as URANS calculations, indicating that the anisotropy of the mean velocity field is not an important factor in this application.

#### 5.5.4 Use of Periodic Boundary Conditions

Most participants submitted results based on the full  $5 \times 5$  bundle geometry; that is, with no assumption made concerning the inherent symmetry of the configuration, though this was assumed in the experiment, for which measurements were made only in a  $1/4$  section of the bundle cross-section. However, there were two submissions which considered only a portion of the flow channel, and imposed periodic boundary conditions on the symmetry surfaces. For the split vane case, Submission Sp05 deals only with a four sub-channel configuration, applying periodic boundary conditions at all ends, as shown in Fig. 24.

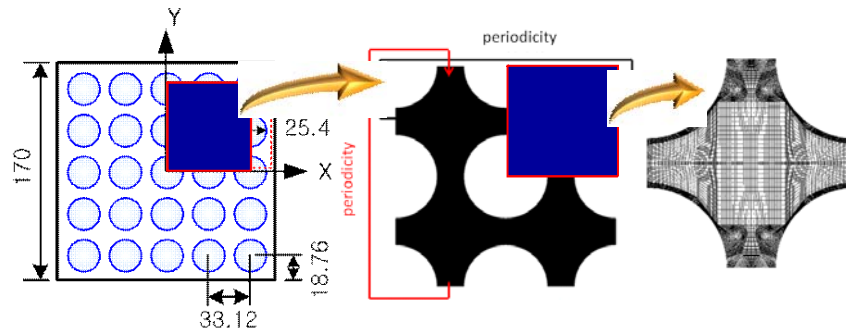


Fig. 24: Geometry for the 2x2 sub-channel simulation Sp05.

Comparing with the case of simulating the full rod bundle, this submission gives an opportunity to investigate the periodicity effect. About 20M control volumes were used for the  $1/4$ - $1/5$  scaled-down geometry, which would correspond to over 100M control volumes for the full 5x5 geometry. However, note that the regions adjacent to the channel walls have not been included in this analysis, so this information, which was requested in the Benchmark Specifications (Annex 2), could not be supplied. For this reason, this submission was not included in the ranking procedure.

The mean and rms velocity profiles for Sp05 at both  $Z = 1.0 D_H$  and  $Z = 4.0 D_H$  are compared in Figs. 25 and 26 against one of the top-ranked 5x5 simulations, Sp12, and with measured data. Note that for the mean  $w$ -component of velocity in Fig. 25, the Sp02 profile ends at the periodic boundary located at  $X/P = 2.0$  and does not correctly reproduce the profile for this plane. This is a direct consequence of the imposed periodicity, since the value is constrained to follow that at  $X/P = 0$ , and represents a fundamental limitation of this approach. Further towards the bundle centre, the magnitudes of the peaks and troughs are seriously overpredicted in 25(a). For the rms values at  $Z = 1.0 D_H$ , magnitudes are reproduced very well in the rod gaps at  $X/P = 0.5$  and  $X/P = 1.5$ , but are badly underestimated elsewhere. It should be noted that both the resolved and modelled fluctuations were considered for obtaining the rms profile in the case of Sp05.

The trend of overprediction of the peaks and troughs in the mean  $w$ -velocity component is also seen further downstream at  $Z = 4.0 D_H$ , Fig. 26, though less exaggerated. The rms values are slightly underestimated at this location, but can be considered satisfactory.

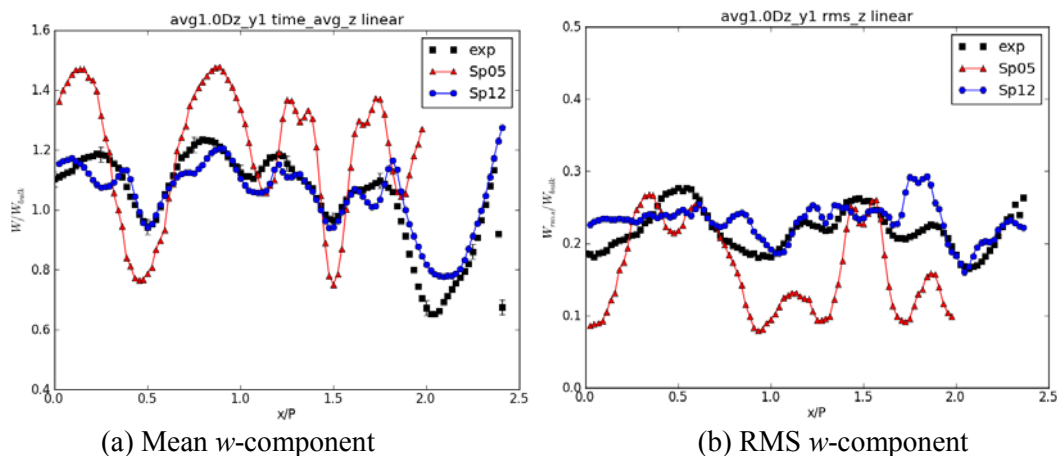


Fig. 25: Comparison of mean and rms  $w$ -velocity profiles at  $Z = 1.0 D_H$  for the 2x2 (Sp05) and a top-ranked 5x5 (Sp12) bundle simulation.

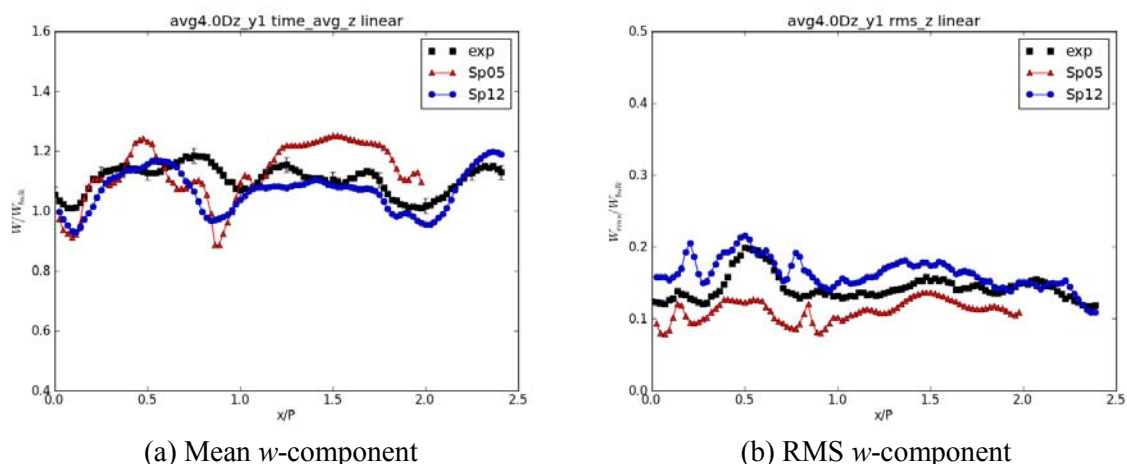


Fig. 26: Comparison of mean and rms  $w$ -velocity profiles at  $Z = 4.0 D_H$  for the 2x2 (Sp05) and a top-ranked 5x5 (Sp12) bundle simulation.

The typical pattern of the circulation profile is a (negative) maximum located at  $Z = 1.0 D_H$  and then monotonic decay downstream (Fig. 28); this trend follows the measured data. In contrast, that for the 2x2 sub-channel simulation (not shown in Fig. 28) has the maximum closer to the spacer grid at  $Z = 0.5 D_H$ , and thereafter decreases monotonically downstream. Locally, the strong positive vorticity near the rod surfaces is seen for the 2x2 calculation, as well as for the ligament region of near-after vane region, as a consequence of the fine mesh adopted for this reduced-domain study.

### 5.5.5 Time-Averaged Circulation in a Sub-Channel

The circulation data, which had also been requested, was not always supplied, and was anyway judged to be misleading, since vortices of positive sign generated near the rod surfaces tended to cancel that of negative sign in the central part of the sub-channel once integration over the entire sub-channel volume had been performed. As a consequence, the integral value was unrepresentative of the degree of swirl present, and therefore unsuitable for a ranking analysis. There was also a problem with the unacceptable errors in the measured velocities close to the rod surfaces, which meant that no trustworthy estimate of the vorticity was available in these regions. It is therefore decided to discuss the main trends only, using selected submissions by way of illustration.

Figure 27 illustrates the decay in vorticity  $\omega_z$  downstream of the spacer grid in sub-channel 2 (see Fig. 23). A large-scale, elliptical vortex is generated in the centre of the sub-channel by the vane arrangement at the back of the spacer grid. The vortex dissipates downstream, and moves off-centre. At  $Z = 10.0 D_H$ , the vortex has essentially disappeared. At the mid-downstream plane,  $Z = 4.0 D_H$ , the vortex has already moved away from the centre of the sub-channel, and the CFD simulations (not shown here) capture this behaviour quite well.

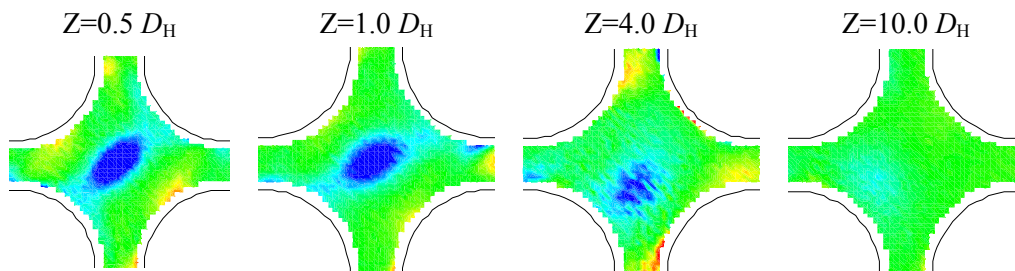


Fig. 27: Measured vorticity contours in the range:  $-350 < \omega_z < 350 \text{ (s}^{-1}\text{)}$ .

Figure 28 shows the development of the integrated circulation along the sub-channel. Even though submission Sp12 correctly predicts the overall velocity field, it does not reproduce the flow behaviour in the far downstream. At  $Z = 10.0 D_H$ , the counter-clockwise vortex, shifted south-west from the centreline (Fig. 27), almost disappears, a trend followed by the other simulations. However, for Sp12, there is a residual positive value of  $z$ -vorticity in the sub-channel in a north-south direction. This kind of abnormal behaviour affects the integrated value, i.e., the circulation, which is then itself positive at  $Z = 10.0 D_H$ , as Fig. 28 depicts. Both the submissions Sp09 and Sp15 underpredict the circulation in the near-vane region, because the secondary vortices near the rod surface and the ligament of the sub-channel were captured, which then contributed to the integration for the circulation.

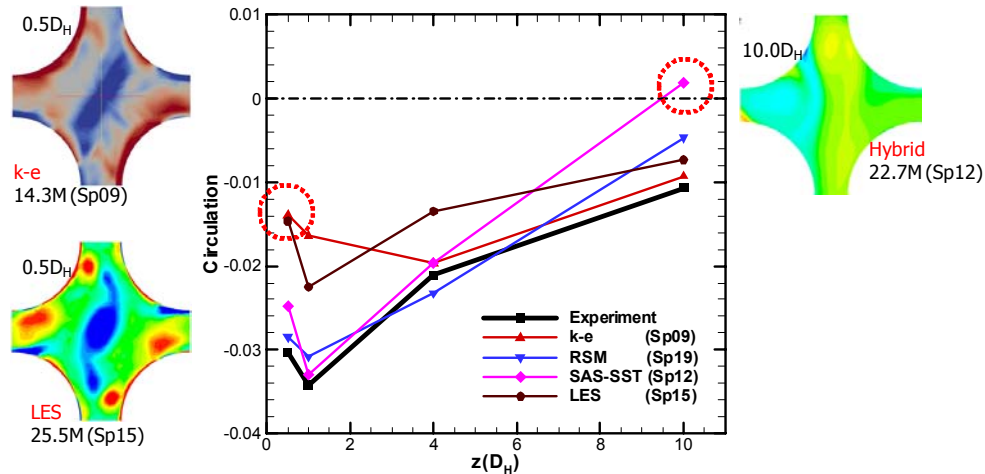


Fig. 28: Variation of circulation along the flow direction

### 5.5.6 Rankings based on combined mean and rms predictions

Starting from the principle that what could be termed a ‘best-ranked’ simulation should be one for which overall performance is judged, new insights can be obtained from amassing the individual ranking data based on the individual mean and rms tables. The method chosen for doing this is to add together the four separate ranking positions given in Tables 12 and 13 at  $Z = 1.0 D_H$  and  $Z = 4.0 D_H$  in terms of the mean and rms ranking positions into one single overall score, the lowest score representing the highest ranking. This results in the overall performance table given in Table 14. Only the top five (5) and bottom five (5) rankings are shown. Note that this procedure in terms of ranking positions was considered superior to simply summing the individual scores, which could have led to distortions due to isolated excellent performance for a single comparison item.

Table 14: Overall performance ranking derived from the mean and time-averaged rms ranking positions at  $Z = 1.0 D_H$  and  $Z = 4.0 D_H$  for the split-type spacer.

Ranking		$z = 1.0 D_H$		$z = 4.0 D_H$		Total Score
Position	Submission	Mean	RMS	Mean	RMS	
1	Sp12	1	1	4	3	9
2	Sp19	2	3	1	4	10
3	Sp15	5	5	5	6	21
4	Sp06	11	7	3	1	22
5	Sp17	6	4	8	9	27
17	Sp14	8	13	19	14	54
18	Sp22	9	18	20	25	64
19	Sp20	20	17	13	18	68
20a/20b	Sp04/Sp21	19/21	19/21	21/15	19/21	78

The top-ranked submission under this classification is Sp12, which relates to a non-steady calculation based on the SAS-SST turbulence model, the mesh featuring 13.1M control volumes, and with second-order differencing in space and time. The second-ranked submission (Sp19) is also a non-steady calculation, with second-order differencing in space and time, but based on a variant of the Reynolds Stress Model (BSL EARSM); 22.7M control volumes were employed in this case. Other highly ranked submissions featured different turbulence models: LES-Smagorinsky (Sp15), combined LES/SAS (Sp06), and SST- $k\omega$  (Sp17). All employed second-order differencing in space and time. The number of control volumes used was moderate: 25.5M (Sp15), 22.2M (Sp06) and 49M (Sp17), these being a mixture of tetrahedral, hexahedral and polyhedral types.

The lowest-ranked submissions, Sp04 and Sp21, were both steady-state simulations, but this appears not to be a major penalising factor, since other submissions of this type (not shown in Table 14) were of intermediate ranking. However, it should be pointed out that no steady-state simulation achieved a high ranking in this exercise. This could be due to the presence of the dimples supporting the rods in the MATiS-H test, a feature not common to production spacer grid design. The dimples would have induced vortex shedding in the flow, which the steady-state RANS approaches would not be able to capture. Perhaps the inherent unsteadiness of the flow manifested itself in a lack of convergence for the steady-state calculations, though this information had not been requested by the organisers, a shortcoming that should be corrected in future benchmarks in the series.

Though different choices were made in regard to turbulence model, RSM for Sp04 and SST- $k\omega$  for Sp21, and the number of control volumes employed, 22.5M and 68M, respectively, there were other submissions that performed better. The largest number of control volumes, 144M, was employed in the Sp22 submission. A variant of LES was used model turbulence, and second-order differencing in space and time was also employed. Despite these seemingly advantageous features, this submission achieved a poor overall ranking.

The ranking in terms of overall performance has highlighted some anomalies in the calculations. Submissions Sp14 and Sp22 were ranked moderate-to-high (8 and 9, respectively) in terms of their mean velocity predictions just downstream of the spacer ( $Z = 1.0 D_H$ ), but this performance was not maintained further downstream, and the ranking positions at  $Z = 4.0 D_H$  had slipped to 19 and 20, respectively. The rms rankings in both cases were low-to-moderate. There seems to be no correlation for this common behaviour, either in terms of the turbulence model used (SAS-SST and Ideal LES, respectively), or in terms of number of control volumes employed (6.5M and 144M, respectively).

Somewhat similar behaviour is seen for submission Sp16, which ranked very highly in terms of mean velocity at  $Z = 1.0 D_H$  (position 4), but which slipped to position 16 at  $Z = 4.0 D_H$ . At both downstream locations, the rms rankings were low-to-moderate. The RSM turbulence model was used for this simulation, and the number of control volumes was 33M. However, it is noted that first-order differencing was employed for both the time and space discretisations, choices that no doubt contributed to the overall poor performance.

In contrast, submissions Sp09 and Sp06 recorded mid-table positions in terms of mean velocity predictions at  $Z = 1.0 D_H$ , but this improved dramatically (positions 2 and 3, respectively) for the  $Z = 4.0 D_H$  rankings. However, in terms of rms ranking, both submissions were in the lower half of Table 13, which led to poor overall rankings in both cases (positions 17 and 18 in Table 14). The turbulence models here were  $k-\epsilon$  (Sp09) and hybrid SAS/LES (Sp06), and the number of control volumes employed was 96M (Sp09) and 22.2M (Sp06). Again, there appears to be no obvious reason, at least in terms of these parameters, why the separate ranking levels should show similar behaviour.

It is hoped that more information will be obtained by the individual participants exploring the reasons for the anomalous behaviour and learning from the experience. Though no collective post-test analysis is possible within the framework of the present benchmark exercise, it is nonetheless

anticipated that post-test simulations will be carried out in individual cases, and duly reported in the literature.

## 5.6 Rankings for Swirl-Type Spacer Simulations

### 5.6.1 Mean Velocities

The final rankings for comparisons based on mean velocity for the swirl-type spacer at the same two downstream locations  $Z = 1.0 D_H$  and  $Z = 4.0 D_H$  are given in Table 15.

Table 15: Ranking according to time-averaged mean velocities for the swirl-type spacer.

$Z=1.0 D_H$			$Z=4.0 D_H$		
Rank	Score	Submission	Rank	Score	Submission
1	11.41	<b>Sw02</b>	1	9.68	<b>Sw07</b>
2	12.51	<b>Sw12</b>	2	10.33	<b>Sw12</b>
3	13.27	<b>Sw07</b>	3	10.44	Sw03
4	13.52	Sw15	4	10.74	<b>Sw02</b>
5	14.52	Sw06	5	11.28	Sw05
6	14.74	Sw08	6	11.40	Sw08
7	15.54	Sw05	7	13.23	Sw04
8	16.66	Sw04	8	13.28	Sw09
9	19.88	Sw10	9	15.66	Sw06
10	22.76	Sw01	10	16.36	Sw10
11	22.92	Sw09	11	19.90	Sw13
12	31.58	Sw03	12	21.43	Sw15
13	47.95	Sw13	13	26.40	Sw01
14	64.87	Sw14	14	41.99	Sw14

The ranking in Table 15, unlike the case for the split-type spacer, shows that numerical predictions made using the LES turbulence model (Sw02, Sw07, Sw12) are generally in best agreement with the measured data, though the top six (6) rankings are all within a small error band (<8%).

In the Benchmark Specifications (Annex 2), participants were encouraged to submit calculation data for both the split-type and swirl-type spacer grid designs, and indeed fifteen (15) did so. However, if participants preferred to analyse just one type, it was recommended to simulate the split-vane case. From the total of 25 submissions, 15 dealt with the swirl-vane type, and among them, the three submissions Sw08, Sw11 and Sw12 focused only on this type. As explained in Section 5.5.1, the LES simulations perform rather better than (U)RANS generally.

### 5.6.2 Time-Averaged RMS Velocities

Rankings have also been made, based on the time-averaged rms velocity data for the swirl-type spacer, and these appear in Table 16. As with the split-type spacer synthesis, a high ranking for both the mean and rms velocity data are necessary for overall performance to be considered acceptable. A quantitative evaluation is presented in Section 5.6.6.

Table 16: Ranking according to time-averaged rms velocities for the swirl-type spacer.

$Z=1.0 D_H$			$Z=4.0 D_H$		
Rank	Score	Submission	Rank	Score	Submission
1	3.8	Sw08	1	2.12	Sw12
2	7.61	Sw03	2	2.51	Sw08
3	8.35	Sw12	3	2.87	Sw07
4	9.35	Sw09	4	3.48	Sw03
5	9.68	Sw07	5	4.1	Sw10
6	11.06	Sw05	6	7.59	Sw05
7	17.14	Sw10	7	8.96	Sw04
8	19.01	Sw04	8	10.02	Sw02
9	22.39	Sw02	9	10.55	Sw09
10	34.09	Sw15	10	20.22	Sw15
11	34.7	Sw13	11	22.7	Sw13
12	37.12	Sw06	12	23.17	Sw01
13	37.16	Sw01	13	23.43	Sw06
14	37.23	Sw14	14	23.48	Sw14

The results from the swirl vane calculations are described in the synthesis report from the following points of view:

- Top 3 mean velocity predictions compared;
- Top 2 rms velocity predictions compared;
- Effect of turbulence model;
- Effect of simulating some selected sub-channel(s) with periodic boundary conditions.

Highlights are given here for the first and last items only, to serve as illustration.

### 5.6.3 Best Estimation for Top-Ranked Simulations

From Table 15, the top three (3) results, ranked in terms of mean velocity, i.e. Sw02, Sw07 and Sw12, are selected here for closer. Two participants used the LES turbulence model, but employed different subgrid-scale (SGS) models: Smagorinsky for Sw07 and WALE (Wall-Adapting Local Eddy-viscosity) for Sw12. In general, it is expected that the LES-WALE model would be the more appropriate for large-scale computations on complicated geometries [27]. However, in this case, Sw07 (Smagorinsky) also shows good agreement with the measurements: in fact, this simulation produced the best agreement of all the calculations at  $Z = 4.0 D_H$ . The Sw02 calculation, which uses the hybrid SAS/LES model (SAS upstream, LES downstream), also performs well in this case. Figure 29 shows the computational mesh for the three (3) selected cases in a typical sub-channel. The number of control volumes used ranges from 20.6M (tetrahedral) for Sw02 to 110M (hexahedral) for Sw12, but both calculations are seen to perform well here. It would be a good post-test exercise to investigate the minimum number of control volumes of each type necessary to produce good comparisons with experimental data. This statement can also be applied to the simulations relating to the split-type spacer.

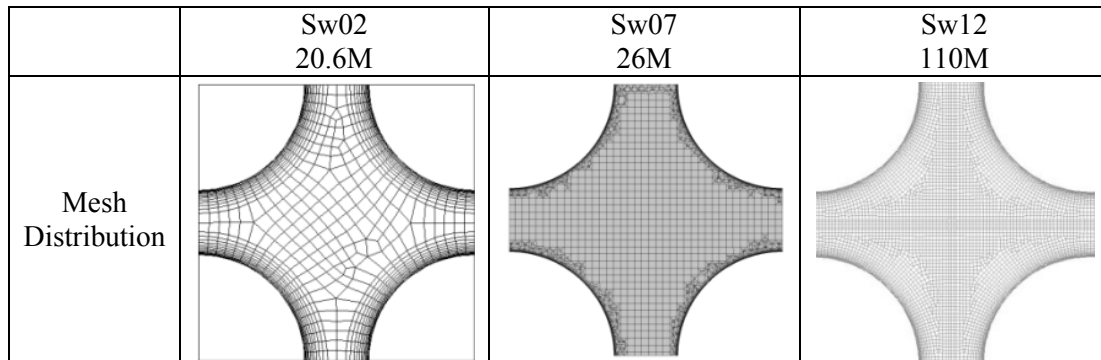


Fig. 29: Mesh distributions for the top 3 ranked results for the swirl-vane case.

Figure 30 shows time-averaged mean and rms  $u$ -velocity profiles at  $Z = 1.0 D_H$  downstream of the spacer grid. Unlike the flow behaviour observed for the split-vane case (Fig. 23), the large sinusoidal-type profile of the mean  $u$ -velocity component does not appear. Instead, the velocity profile is quite flat, but with small-scale fluctuations. All three selected simulations follow the correct trend, including the increase in velocity near the channel wall. The rms values are also smaller than in the split-vane case, but the fluctuations are more distinct. Submission Sw02 (SAS/LES) is seen to badly under-estimate the magnitude of the fluctuations, while the other (pure LES) models perform better.

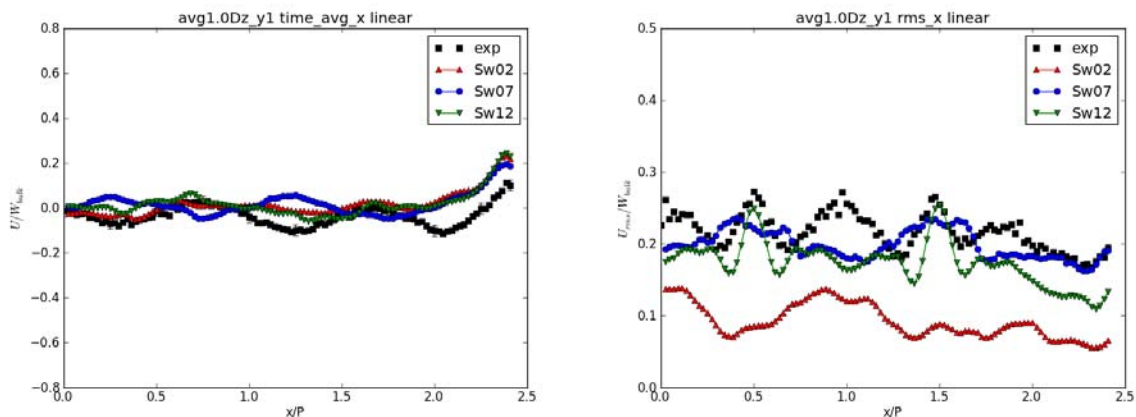


Fig. 30: Time-averaged mean and rms  $u$ -velocity profiles at  $Z = 1.0 D_H$ .

Figure 31 shows time-averaged mean and rms  $w$ -velocity profiles, also at  $Z = 1.0 D_H$  downstream of the spacer grid. This component exhibits quite distinctive periodicity in the mean field. Submission Sw12 has a tendency to overpredict the peaks, but the other calculations capture the measured profile very well, except in the region close to the channel wall, where Sw07 underpredicts the decay to zero velocity. For the rms velocity profiles, again the Sw02 submission with the hybrid (SAS/LES) turbulence model significantly underpredicts the magnitudes, perhaps as a result of the coarse mesh used in the central region, whereas the other two submissions bracket the measured profile. These trends are also reflected in the behaviour for the  $v$ -component of velocity, and repeated further downstream (details not shown here). From this information, it appears that only a full LES simulation can accurately reproduce the rms values for this application.

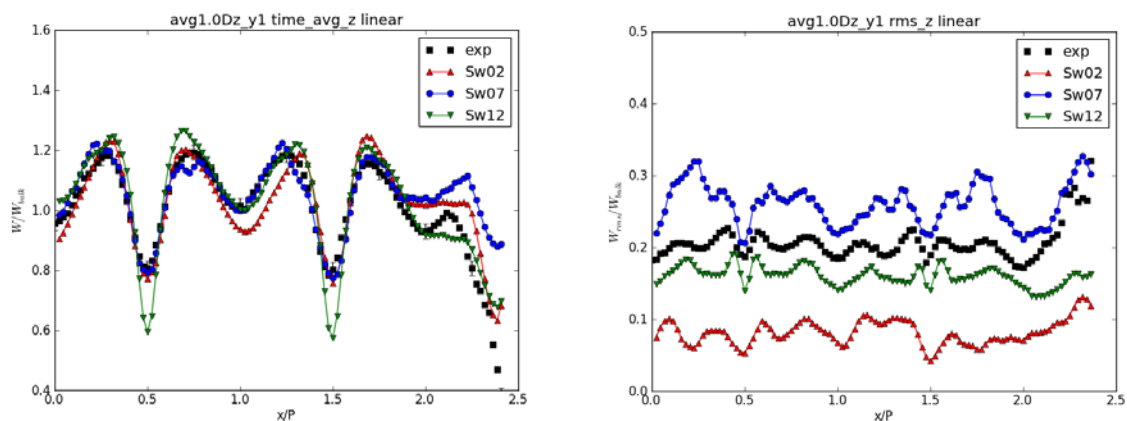


Fig. 31: Time-averaged mean and rms  $w$ -velocity profiles at  $Z = 1.0 D_H$ .

#### 5.6.4 Use of Periodic Boundary Conditions

For the swirl-vane geometry, the Sw11 submission reported results from a single sub-channel calculation, with periodic boundary conditions imposed on the free-flow domain boundaries. A hybrid mesh was constructed, consisting of a mix of 3M hexahedral/tetrahedral control volumes. Some details are shown in the Fig. 32. The RANS-based SST- $k\omega$  turbulence model was employed for this simulation.

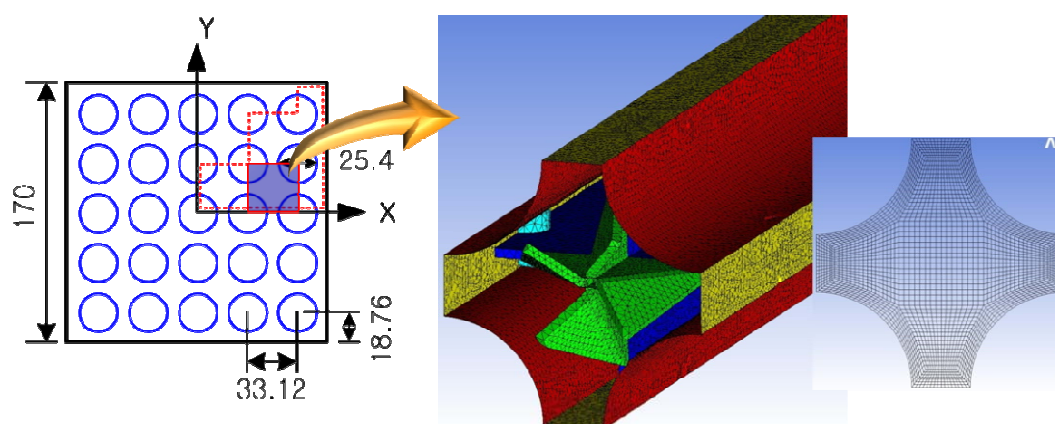


Fig. 32: Geometry for the single sub-channel simulation Sw11

As shown already for the 2x2 split-vane simulation (Sp05), the overall behaviour of mean cross-flow velocity components  $u$  and  $v$  show qualitatively good agreement with the measurement at  $Z = 1.0 D_H$ , with considerable overestimation of the amplitudes at the extrema, compared both with the experiment and a top-ranked 5x5 simulation (Sw02), which itself reproduces the extrema very well, as seen clearly in Fig. 33. Further downstream ( $Z = 10.0 D_H$ ), the profile becomes smoother, but a slight tendency to overprediction remains.

The single sub-channel simulation (Sw11) also overpredicts the extrema of the time-averaged velocity fluctuations (not shown here). A further anomalous feature is that the fluctuations are greater in magnitude at  $Z = 10.0 D_H$  than at  $Z = 4.0 D_H$ . Such behaviour is highly suspect, and probably reflects a lack of convergence in the numerical procedure.

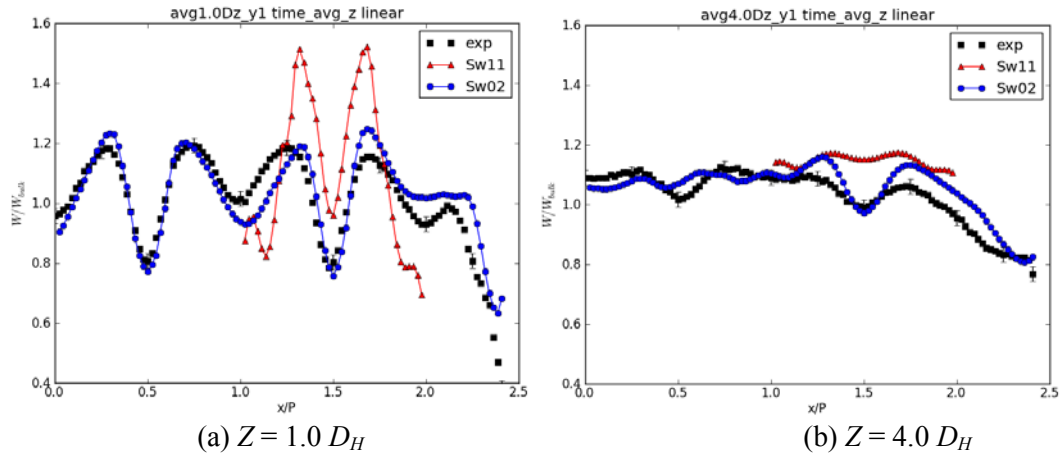


Fig. 33: Mean  $w$ -component profile for the single sub-channel simulation Sw11.

The circulation profile along the flow direction for this case (Fig. 34) also exhibits spurious behaviour, as discussed in the synthesis report [23]: the vertical structures at each measurement plane differ both from those measured and the best estimation 5x5 sub-channel simulation case (Sw02). More than one pair of secondary vortices is observed in the ligament region, which may be due the confined geometry and/or the use of periodic boundary conditions in the ligament region. As can be seen in Fig. 34, the circulation actually increases downstream, in total contrast to all other submissions to this benchmark. It can be concluded that a single sub-channel simulation of the spacer grid is not recommended in this benchmark, even as a means of capturing the overall mean flow behaviour.

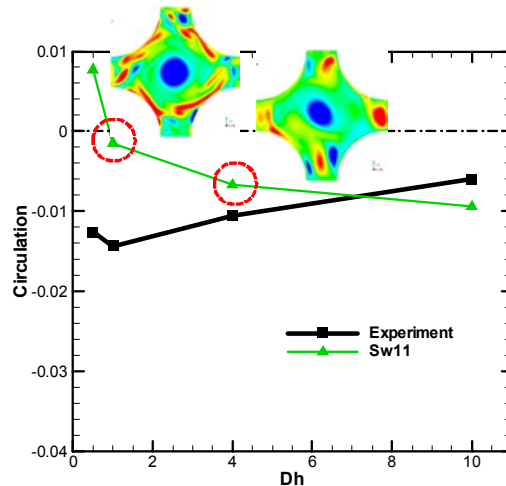


Fig. 34: Development of circulation downstream for the single sub-channel simulation Sw11.

Again, since all profiles for Sw11 across the measurement lines are truncated as a consequence of the periodicity assumption, a quantitative comparison with measurements, according to the metric defined in Eq. (1), cannot be attempted for this submission, which consequently has been excluded from the ranking procedure.

### 5.6.5 Time-Averaged Circulation Data in a Sub-Channel

Figure 35 shows in qualitative form the development of the mean vorticity component  $\omega_z$  downstream from the spacer grid in sub-channel 2 (see Fig. 23 for orientation), as derived from the velocity measurements and, by way of illustration only, those produced by Submission Sw02. In contrast to the case for the split-vane design (Fig. 27), a more circular vortex shape is generated in the centre of the sub-channel by the vane arrangement for the swirl-type spacer design, which is to be expected,

given that there are vanes in each corner of the rod channel in this case, instead of at diagonal corners, as featured for the split-type spacer. The vortex is seen to dissipate downstream, as expected, but remains centralised in the channel, again in contrast to the split-vane case, for which some drifting off-centre was noted. At  $z = 10.0 D_H$ , the vortex has essentially disappeared. The Sw02 predictions also reflect the stability of the vortex in the centre of the channel, and the decay process, very well.

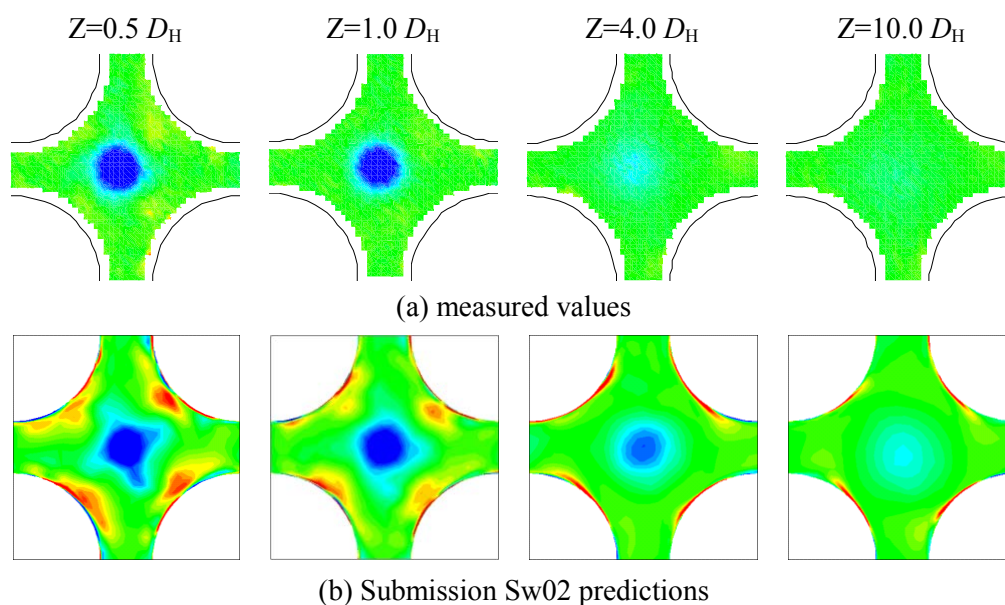


Fig. 35: Vorticity contours in the range:  $-350 < \omega_z < 350 \text{ (s}^{-1}\text{)}$ : a comparison of (a) measured values against (b) predictions from Submission Sw02.

Note the presence of a strong positive vorticity near the surfaces of the rods in Fig. 35(b). The region affected narrows downstream, but does not disappear completely, even at  $Z = 10.0 D_H$ . For the experiment, the errors in the velocity measurements close to the rod surfaces were considered too large to be acceptable, and so values for  $\omega_z$  in these regions are not included in Fig 35(a). Unfortunately, the positive contribution these high vorticity regions would make to the integration over the sub-channel for the calculations, and hence the overall measure of the circulation, makes any quantitative numerical comparisons untrustworthy. At the Open Benchmark Meeting held in Paris on May 30, 2012, it was suggested that integration over the reduced area seen in Fig. 35(a) would provide more meaningful comparisons with measured data. However, since not all participants – particularly those who had performed transient calculations – were able to respond to this very late request, a strict ranking based on circulation has not been attempted. Thus, for illustrative purposes only, the integrated circulation along the sub-channel is shown in Fig. 36 for the two (2) top-ranked simulations Sw02 and Sw07 (both full LES) and for Sw04, a middle-ranked simulation featuring the BSL RSM turbulence model.

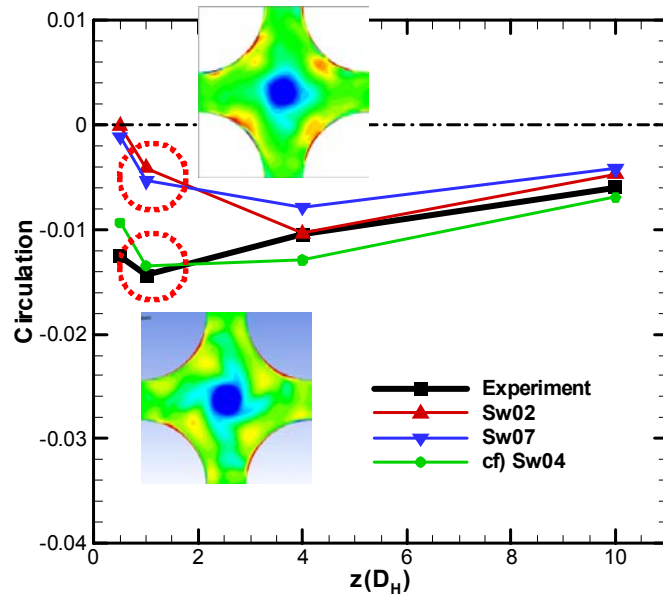


Fig. 36: Variation of circulation for the two best-ranked simulations Sw02 and Sw07, and for Sw04, for the swirl-type spacer design.

As can be seen, the circulation at  $Z = 0.5 D_H$  and  $Z = 1.0 D_H$  for Sw02 and Sw07 exhibit underpredictions. As explained above, this could be due to the positive contribution made to the integration by the vorticity close to the rod surfaces. By comparison, Sw04 shows good agreement with measured values. As the secondary vortices decay downstream, the circulations derived from the Sw02 and Sw07 results recover, and compare very well with experiment at  $Z = 10.0 D_H$ .

### 5.6.6 Rankings based on combined mean and rms predictions

As for the submissions for the split-vane spacer design (Section 5.5.6), further insights can be obtained from combining the ranking positions given in Tables 14, 15 at  $Z = 1.0 D_H$  and  $Z = 4.0 D_H$ , respectively, to obtain an estimate of overall performance. Results are presented in Table 17, with only the top five (5) and bottom five (5) positions shown.

Table 17: Overall performance ranking according to mean and time-averaged rms ranking positions at  $z = 1.0 D_H$  and  $z = 4.0 D_H$  for the swirl-type spacer.

Ranking		$z = 1.0 D_H$		$z = 4.0 D_H$		Total Score
Position	Submission	Mean	RMS	Mean	RMS	
1	Sw12	2	3	2	1	8
2	Sw07	3	5	1	3	12
3	Sw08	6	1	6	2	15
4	Sw03	12	2	3	4	21
5	Sw02	1	9	4	8	22
10	Sp15	4	10	12	10	36
11	Sw06	5	12	9	13	39
12	Sw13	13	11	11	11	46
13	Sw01	10	13	13	12	48
14	Sw14	14	14	14	14	56

The top-ranked submission, Sw12, is a calculation based on the LES WALE turbulence model, for which 110M combined hexahedral/tetrahedral control volumes were employed; second-order differencing in both space and time were adopted. As can be seen from Table 17, the high ranking is due to fully consistent mean and rms predictions at both downstream locations. The second-ranked submission, Sw07, exhibits similar consistency. This is also an LES simulation (but with the Smagorinsky SGS model), employing 26M control volumes. The third-ranked submission is very special. Again an LES (spectral damping) approach is used, but the number of control volumes employed (700K) at first glance looks to be far too small to support a turbulence model of this type. Indeed, some of the RANS model simulations featured two orders of magnitude more control volumes. The excellent performance of this simulation appears to derive from the high-order discretisation method applied (third-order in time and seventh-order in space), which seems to have compensated for the small number of control volumes used. Though the mean velocity comparisons could be improved, the rms comparisons are the best of all the submissions received for this spacer-grid type.

For the performance in terms of mean velocity comparisons, the ranking at  $Z = 4.0 D_H$  generally followed that at  $Z = 1.0 D_H$ . However, there are two exceptions: Sw15 is ranked highly (position 4) at  $Z = 1.0 D_H$ , but slips to position 12 at  $Z = 4.0 D_H$ . In contrast, Sw03 is low-ranked (position 12) at  $Z = 4.0 D_H$  but this improves markedly at  $Z = 1.0 D_H$  (position 3). However, the rms comparisons are both very good for Sw03, which lifts this submission into 4<sup>th</sup> position based on overall performance, while those of Sw15 are poor, so that overall this submission is near the bottom of the combined ranking table. The participants responsible for these simulations are advised to investigate this adverse behaviour.

Performance based on rms predictions is more consistent at the two downstream locations for the swirl-type spacer simulations than those for the split-type. The one exception is for Sw09 (URANS, SST- $k\omega$ , 63M control volumes), for which the rms comparison is good (ranking position 4) at  $z = 1.0 D_H$ , but deteriorates to mediocre (ranking position 9) at  $Z = 4.0 D_H$ .

The two simulations ranked the lowest in terms of overall performance, Sw01 and Sw14, are the only ones for the swirl-type spacer geometry to employ RANS turbulence models (RSM and SST- $k\omega$ , respectively). Likewise, simulations Sp04 and Sp21, which also featured RANS approaches (also RSM and SST- $k\omega$ , respectively), obtained lowest overall ranking for the split-type geometry case.

## 5.7 *Conclusions from the Synthesis of Results*

Certainly, there is a wealth of data to analyse arising from this benchmark exercise. A full synthesis of the results has been carried out by staff at KAERI, and the interested reader is referred to their detailed paper [23]. Only selected highlights could be presented in this report. It is hoped that individual participants will themselves follow up many of the issues raised.

As already suggested in the synthesis report for the previous T-junction benchmark exercise [24], and the OECD Best Practice Guidelines (BPGs) document for the use of CFD in nuclear reactor safety applications [3], the results from the present synthesis also confirm that the use of first-order upwind discretisation should be avoided, except to demonstrate qualitative behaviour. In the present benchmark exercise, the use of a large number of control volumes and high-grade turbulence model were not always seen to be a guarantee of a superior numerical solution. Indeed, the current trend to arbitrarily increase the number of mesh points just to take advantage of improved hardware capability is generally undesirable for industrial applications. More important is to ascertain the degree of accuracy of coarse-mesh simulations and simplified turbulence models.<sup>#</sup>

---

<sup>#</sup> The authors are grateful to K. Y. Kim for emphasising this point in his review of this document.

Mesh quality and experience of the CFD practitioner in understanding of the physical phenomena relevant to the problem, and to generate an appropriate mesh, also brings rewards in terms of numerical accuracy. In this respect, it would be helpful for less experienced CFD users to follow the checklist for producing quality CFD calculations, as proposed in the OECD Best Practice Guidelines [3] before attempting to use CFD software in nuclear reactor safety studies.

In contrast to the first benchmark exercise for the T-junction geometry [10,11,24], the LES turbulence model did not overwhelmingly show its superiority over other approaches, such as DES and URANS. This was somewhat unexpected. Also, the poor performance of the SAS-SST model for the T-junction benchmark was completely turned around in this application, with a top-3 ranking for both the split-type and swirl-type spacer simulations in this case. From the ranking tables based on overall performance at the two downstream locations  $Z = 1.0 D_H$  and  $Z = 4.0 D_H$ , it would appear that the use of steady two-equation RANS and RSM models are unsuitable for this application.



## 6. OVERALL CONCLUSIONS

The number of registered participants (48 from 22 countries, with 25 submissions ahead of the deadline) to the OECD/NEA-KAERI Rod Bundle Benchmark Exercise itself demonstrates the general level of interest in the topic. Since the design of grid spacers is highly proprietary information, it has always been difficult to organise a code-comparison exercise on the subject, and quantify predictions using test data. There were several unique features of the present benchmark activity that have contributed to the broad level of interest shown in it: (i) two grid spacers of generic design were offered by KAERI in support of this activity; (ii) as an aid to CFD grid generation, CAD files, in several standard formats, were also offered; (iii) dedicated experiments were performed in the MATiS-H facility, and the data obtained from them were kept secret to provide conditions for a “blind” benchmarking exercise; (iv) further experiments were carried out voluntarily by KAERI, and at their own expense, to allay concerns voiced on the part of some participants that the measured data may not be of “CFD-grade” quality in the accepted sense because of the proximity of the measuring plane to the outlet manifold; (v) this same concern prompted the group at EC-JRC Petten to construct a CAD file of the entire facility, including full representation of the outlet manifold, and offer it voluntarily to all participants; (vi) on the part of the sponsoring organisation, the OECD Nuclear Energy Agency, the previous success of the T-junction benchmark was a contributing factor in the level of interest shown here; and (vii) the opportunity for participants to display their work, and discuss different aspects of the modelling issues with their contemporaries, at the CFD4NRS-4 Workshop, all contributed to the success of the exercise.

The subject of spacer grid design, and the ability of CFD technology to contribute to the technology, is both topical and pertinent to the planned power upgrades at existing Gen II nuclear reactors, and to future reactors. It is expected that the application of state-of-the-art CFD codes is needed to predict the important parameters governing turbulence production and heat transfer in rod bundles, to enhance efficiency, and to increase safety margins. Though the present tests were performed under isothermal conditions, accurate prediction of the turbulence characteristics generated downstream by the vanes of the spacer grids is a obvious pre-requisite for exploring the fuel-to-coolant heat-transfer properties using the technology, and it is in this context that the present exercise has made an important contribution to the general level of understanding. Consequently, the idea of organising a CFD rod-bundle benchmark exercise proved attractive to many organisations, as reflected in the number of registrations.

Given the availability of suitable test data, and the willingness of KAERI to release the information, an organising committee was set up early in 2011 to explore the potential for an international activity on this subject. C.-H. Song, who had overseen previous tests in the MATiS-H facility, was invited to join the committee to help organise the benchmark activity. He also expressed a willingness to organise the next workshop in the CFD4NRS series, not only to continue the tradition of providing a forum for experimenters and analysts to exchange information, but to provide a meeting point for participants in the benchmark to discuss their respective results, and inspect the MATiS-H test rig first-hand.

C.-H. Song and his colleagues at KAERI, who are co-authors of this document, agreed to be responsible for the synthesis of the benchmark submissions. Because of security restrictions on the KAERI website, it was not possible for participants to automatically upload their data files. Instead, the information was sent by email. This, less-automated form of data transfer placed a heavy burden on KAERI staff, and should be avoided in any future benchmarking activity of this sort. Better would be to have a dedicated website for which participants are given limited access, a procedure it was possible to follow for the previous T-junction CFD benchmark exercise in this series.

Of the 25 participants who submitted results by the deadline (originally set for April 30, 2012, but extended to May 29, 2012), the majority used commercial CFD software packages (>75%). The number of control volumes used varied from 700 K to 144 M. The majority (15) chose a RANS model of turbulence modelling, while others (2) chose a hybrid model, while the remainder (8) elected for some form of Large Eddy Simulation (LES) model.

There is a mass of data available for analysis, and it is hoped that the individual participants will explore the possibilities in connection with their own simulations. In the context of an overall assessment, some salient points have been alluded to in Section 5 of this report. The submissions were ranked according to two (2) separate metrics for the time-averaged mean and rms velocity components in all three directions at four (4) specified locations downstream of the spacer grid, and then summed to give an overall score. The positions changed somewhat when ranked according to correspondence with the time-averages rms velocity data. Only those with high rankings for both the mean and rms predictions were considered to have performed well in this benchmark. This point was taken up quantitatively by combining the separate mean and rms velocity rankings into an overall ranking.

A circulation metric was also constructed, but not used. This is because of the strong influence on the integrated vorticity over the sub-channel resulting from the vorticity generated near the rod surfaces for which the measurements had large errors. Consequently, only a qualitative analysis was carried out for this data item.

Overall, it can be stated with confidence that the rod-bundle benchmark has been very successful. Active participation was high (25), reflecting the level of generic interest in the issue. All registered participants (48) received CAD files of the two spacer grid designs, and the official benchmark specifications. In addition, they received regular updates of the extra efforts made by KAERI to answer the queries that had arisen since the first release of the specifications. On the positive side, the CAD files were correct at the time of issue. Some specific software packages had problems in reading them, though others did not. Perhaps this reflects the present state-of-the-art of the technology. On the negative side, there were a few inconsistencies between the electronic versions of the geometry and that reproduced in the printed specifications. All of these problems were ultimately resolved, but some participants voiced frustration that the information was not as “clean” as they would have hoped. However, since the computations generally were not as computer intensive as they were with the T-junction benchmark, no major problems were reported.

Another positive aspect was the initiative taken by the EU JRC Petten group in producing a CAD file of the entire MATiS-H facility, which did not exist before. Though it was not possible to quality assure its accuracy within the confines of the benchmark exercise, the file does represent a valuable addition to the information officially distributed, and hopefully will be used in any follow-up studies.

Another aspect of this benchmark, in contrast to the T-junction exercise, is that there was still time for the attendees at the kick-off meeting to influence the set up of the experiment, and many of the suggestions made – particularly in regard to the specification of inlet conditions, and the influence of the outlet boundary conditions on the measurements – were followed up positively by KAERI, in the spirit of the activity. These involved performing additional experiments in the facility, at their own

expense, to provide the requested information. The efforts made by the organisation in this regard are major contributing factors in the success of the benchmark activity, and are gratefully acknowledged.

Different codes, different modelling approaches, and different numbers of control volumes have been adopted by the various participants, and there is even useful information forthcoming from those who used the same code and/or similar modelling approaches. From the outset, the modus operandi for this exercise was that the numerical analysts were given the challenge of choosing, and then employing, what they considered to be their best attempt at supplying the information requested by the benchmark organisers. In other words, their judgment and CFD expertise were also considered part of the challenge proffered by the exercise. The participants are to be congratulated in accepting this challenge.

As a result of the synthesis of the results performed, the following observations can be made.

- Though different assumptions were made regarding the most appropriate upstream boundary conditions to employ – uniform, developed, measured – the choice appears not to be crucial for this application, presumably because of the complete regeneration of the flow characteristics by the spacer grid.
- In line with the established Best Practice Guidelines (BPGs) for CFD simulations, this exercise has reinforced the need for at least second-order accurate discretisation algorithms (these days often the default option for commercial CFD software) to avoid degrading results by excessive numerical diffusion.
- There appears to be no direct correlation between the quality of code predictions and the absolute number of discrete control volumes employed and/or their type. For example, submission Sp22 offered the most (144M) control volumes used in this exercise, these were of combined tetrahedral and hexahedral type, the turbulence model chosen was a variant of LES, and second-order discretisation in both space and time were adopted for the calculation. In addition, care was taken concerning inlet conditions, which were derived on the basis of a full-length channel simulation. In short, all the ingredients appeared to be in place to ensure a trustworthy numerical simulation of the bundle test. Instead, an overall ranking of 18/21 was obtained. In contrast, submission Sp19, which employed the pseudo-RSM turbulence model BSL EARSM, which is still ultimately RANS-based, produced excellent results from a combination of 22.7M tetrahedral and hexahedral mesh types, and was ranked 2/21 in the present analysis.
- Of the simulations for the split-type spacer design, best overall ranking derived from use of different turbulence modelling approaches: SAS-SST (Sp12), BSL EARSM (Sp19), LES (Sp15), Hybrid SAS/LES (Sp06) and SST- $k\omega$  (Sp17).
- From simulations of the swirl-type spacer design, top five (5) rankings were all derived from calculations in which some variant of the LES turbulence model was employed.
- Lowest-ranked simulations, for both the split-type and swirl-type spacer designs were all based on steady-state calculations: Sp04, Sp21 and Sw14, Sw01, respectively. However, other steady-state simulations performed much better: Sp09 (position 6), Sp18 (position 7) and Sw10 (position 8). Thus, it appears that the steady-state assumption may be limiting, though not disastrous, for this application. This may be due to unsteady vortex shedding phenomena associated with the cylindrical pins used to support the rods, a feature which is rather atypical for industrial spacer designs. The inability of the RANS approaches would have manifested itself in a lack of convergence of (particularly) the mass residuals, a data item unfortunately not requested by the benchmark organisers.<sup>‡</sup>
- It is regrettable that a ranking based on circulation in a typical sub-channel could not be derived during this exercise. This is due to the unexpected appearance of intense vorticity filaments produced near the rod surfaces, where velocity measurements had large errors and

---

<sup>‡</sup> The authors are grateful to E. Baglietto for identifying this shortcoming in the specifications.

the lack of time needed in correcting for this within the time-scale of the benchmark. However, new estimates of sub-channel circulation were derived from the measured velocity data and made available to all contributors. It is hoped that many will subsequently use this information outside the confines of the benchmark exercise.

- The discretisation algorithm used for the transport equations of turbulence quantities such as  $k$ ,  $\epsilon$ ,  $\omega$  etc. was not requested by the benchmark organisers. This may have been an oversight in the light of recent work on rod-bundle simulation using CFD [28], since some commercial codes still retain first-order differencing by default for these quantities.

## ACKNOWLEDGMENTS

The authors of this document are indebted to their colleagues on the benchmark organising committee for their technical support to this initiative, their assistance in finalising the benchmark specifications, and their many helpful tips and guidance. In alphabetical order, thanks are due to Abdallah Amri (OECD), Dominique Bestion (CEA), John Mahaffy (privately) and Ghani Zigh (US NRC). Abdallah Amri, in particular, as the member of the NEA secretariat, deserves special thanks for organising the meetings at the NEA Headquarters in Paris, for the writing of the Minutes of these meetings, for coordinating the multifarious organiser/participant exchanges, and for providing help in structuring the benchmark activity according to accepted NEA standards.

Thanks are also due to staff at JRC Petten, Netherlands, for voluntarily producing a CAD file of the MATiS-H test section, including the inlet duct and outlet manifold, and offering it free of charge to all participants in the benchmark exercise. The authors of this document are grateful to H. Wilkening and his co-workers for this initiative.

Special thanks are extended to E. Baglietto of the Nuclear Engineering Department of the Massachusetts Institute of Technology, USA for his careful review of the draft version of this document, and the many suggestions and corrections offered by him in improving the text. In addition, very valuable observations have been made by K. Y. Kim of INHA University, S. Korea, acting as an external consultant to KAERI, in his careful review of this document. All information from these sources have been reviewed by the authors, and imbedded into the text, as appropriate.

Finally, it should be emphasised that KAERI staff have supplied, at considerable expense in terms of capital outlay and manpower, supplementary information over and above that committed in the original benchmark specifications. This additional investment has contributed significantly to the success of this benchmark exercise.



## REFERENCES

- [1] “Exploratory meeting of experts to define an action plan on the application of Computational Fluid Dynamics (CFD) to nuclear reactor safety problems”, Aix en Provence, 15-16 May 2002, CSNI Report NEA/CSNI/R(2002)16.
- [2] “Use of Computational Fluid Dynamics (CFD) Codes for Safety Analysis of Reactor Systems including Containment”, Pisa, Italy, 11-14 Nov., 2002.
- [3] Mahaffy, J. (ed.) “Best Practice Guidelines for the Use of CFD in Nuclear Reactor Safety Applications”, OECD, Nuclear Energy Agency, Technical Report, CSNI/R(2007)5, April 2007
- [4] Smith, B.L. (ed.) “Assessment of Computational Fluid Dynamics (CFD) for Nuclear Reactor Safety Problems”, OECD Nuclear Energy Agency, Technical Report, NEA/CSNI/R(2007)13, Jan. 2008.
- [5] Bestion, D. (ed.) “Extension of CFD Codes to Two-Phase Flow Safety Problems”, OECD, Nuclear Energy Agency, Technical Report, NEA/CSNI/R(2010)2, March 2010.
- [6] CFD4NRS: Benchmarking of CFD Codes for Application to Nuclear Reactor Safety, Garching, Munich, Germany, 5-7 Sept. 2006 (CD-ROM).
- [7] Smith, B. L., Hassan, Y. (eds.) “CFD4NRS: Benchmarking of CFD Codes for Application to Nuclear Reactor Safety”, *Special Issue, Nucl. Eng. Des.*, **238**(3), 443-785 (2008).
- [8] Smith, B.L., Bestion, D., Hassan, Y. (eds.) “Experiments and CFD Code Applications to Nuclear Reactor Safety (XCFD4NRS)”, *Special Issue, Nucl. Eng. Des.*, **240**(9), 2075-2382 (2010).
- [9] <http://meta.wikimedia.org/wiki/Help:Introduction>
- [10] Smith, B.L., Mahaffy, J.H, Angele, K, Westin, J. “Report of the OECD/NEA—Vattenfall T-Junction Benchmark Exercise”, OECD, Nuclear Energy Agency, Technical Report, NEA/CSNI/R(2011)5, May 2011.
- [11] Smith, B.L., Mahaffy, J.H., Angele K., “A CFD Benchmarking Exercise based on Flow Mixing in a T-Junction”, Paper 145, 14<sup>th</sup> Int. Topical Mtg. on Nuclear Thermal Hydraulics (NURETH-14), 25-30 Sept. 2011, Toronto, Canada, CD-ROM, 2011 (ISBN 978-1-926773-05-6).
- [12] Rheme, K., Tripe, G. “Pressure Drop and Velocity Distribution in Rod Bundles with Spacer Grids”, *Nucl. Eng. Des.*, **62**, 349 (1980).
- [13] Shah, V.N. *et al.* “Assessment of Field Experience Related to Pressurized Water Reactor Primary System Leaks”, Proc. ASME Pressure Vessel and Piping Conf., Boston, MA, USA,

August 1-5, 1999.

- [14] Yao, S.C., Hochreiter, L.E., Leech, W.J. “Heat-Transfer Augmentation in Rod Bundles near Grid-Spacers”, *J. Heat Transfer*, **104**, 76 (1982).
- [15] Shen, Y.F., Cao, Z.D., Yu, Q.G. “An Investigation of Cross-Flow Mixing Effect caused by a Grid Spacer with Mixing Blades in a Rod Bundle”, *Nucl. Eng. Des.*, **125**, 111 (1991).
- [16] Karoutas, Z., Gu, C.Y., Scholin, B. “3-D Flow Analyses for Design of Nuclear Fuel Spacer”, Proc. 7<sup>th</sup> Int. Meeting on Nuclear Thermal Hydraulics (NURETH-7), Saratoga Springs, New York, Sept. 10-15, 1995.
- [17] McClusky, H.L., Holloway, M.V., *et al.*, “Mapping of the Internal Flow Field in Typical Subchannels of a Support Grid with Vanes”, *J. Fluids Eng.*, **125**, 987 (2003).
- [18] In, W.K., Oh, D.S., Chun, T.H., “Simulation of Turbulent Flow in Rod Bundles using Eddy Viscosity Models and the Reynolds Stress Model”, Proc. 10<sup>th</sup> Int. Topical Meeting on Nuclear Reactor Thermal Hydraulics (NURETH-10), Seoul, S. Korea, Oct. 5-9, 2003.
- [19] Chang, S.K. *et al.* “Phenomenological Investigations on the Turbulent Flow Structures in a Rod Bundle Array with Mixing Devices”, *Nucl. Eng. Des.*, **238**, 600-609 (2008).
- [20] Kang, H.S., Chang, S.K., Song, C.-H., “CFD Analysis of the MATiS-H Experiments on the Turbulent Flow Structures in a 5x5 Rod Bundle with Mixing Devices”, Proc. CFD4NRS-3 Workshop, Washington DC, USA, Sept. 12-14, 2010.
- [21] Summary record of the Kick-Off Meeting of the OECD/NEA-KAERI Rod Bundle Benchmark 28 April 2011, OECD/NEA Headquarters, Paris, France, NEA/SEN/SIN/AMA(2011)3.
- [22] Chang, S.K., Kim, S., Song, C.H. “OECD/NEA—KAERI Rod Bundle CFD Benchmark Exercise Test”, Proc. CFD4NRS-4 Workshop, Daejeon, S. Korea, Sept. 10-12, 2012.
- [23] Lee, J.R., Kim, J.W., Song, C.-H. “Synthesis of the OECD/NEA-KAERI Rod Bundle CFD Benchmark Exercise”, Proc. CFD4NRS-4 Workshop, Daejeon, S. Korea, Sept. 10-12, 2012.
- [24] Mahaffy, J.H. “Synthesis of Results of the T-Junction Benchmark”, Proc. CFD4NRS-3 Workshop, Washington DC, USA, Sept. 12-14, 2010.
- [25] [www.python.org](http://www.python.org)
- [26] Ikeda, K. *et al.*, “Study of Spacer Grid Span Pressure Loss under High Reynolds Number Flow Condition”, Paper 75925, Proc. 17<sup>th</sup> Int. Conf. on Nucl. Engng. (ICONE17), Brussels, Belgium, July 12-16, 2009.
- [27] Nicoud, S., Ducros, F. “Subgrid-Scale Stress Modelling Based on the Square of the Velocity Gradient Tensor”, *Flow, Turbulence and Combustion*, **62**, 183-200 (1999).
- [28] Connor, M.E. *et al.*, “CFD Methodology and Validation for Single-Phase Flow in PWR Fuel Assemblies”, *Nucl. Eng. Des.*, **240**, 2088-2095 (2010).

## ANNEX 1: ANNOUNCEMENT

### OECD/NEA Sponsored CFD Benchmark Exercise: Turbulent Flow in a Rod Bundle with Spacers

#### Invitation to Kick-Off Meeting

NEA Headquarters, 12 boulevard des Iles  
Issy-les-Moulineaux, Paris, FRANCE

28 April, 2011

#### Background

The spacer grids that support the fuel rods in a nuclear reactor core also act as turbulence-enhancing devices to improve the heat transfer from the hot surfaces of the rods to the surrounding coolant stream. The design of the spacer grids is therefore an important optimization parameter for reactor vendors. Traditional approach to spacer design by experiments is now being supplemented by Computational Fluid Dynamics (CFD). But what are the best modelling options to capture the essential features of the turbulent structures downstream of the spacer, and ultimately the heat transfer mechanism?



Split-Type Spacer



Swirl-Type Spacer

The increasing maturity and trustworthiness of CFD software, coupled with spectacular advances in computer hardware, means that the technology can be employed by industry on a cost-effective basis in any design strategy, but must always be underpinned by suitable validation tests to measure the quality of the numerical predictions. Spacer grid designs are highly proprietary, and so the extent of appropriate validation data available to the CFD modelling community is severely limited.

#### A Blind CFD Benchmark Exercise

In March 2011, a cold rod 5x5 bundle test is being performed in the MATIS-H facility of the Korea Atomic Energy Research Institute (KAERI) in Daejeon, S. Korea. Data from this test have been reserved specifically for this CFD benchmark exercise, and will be kept secret for its duration.

## CFD SIMULATIONS ARE INVITED

Participants in the exercise will be given details of the test geometry (flow channel, rod array and spacer grids), operating conditions (boundary conditions at the channel inlet) and upstream parameters. Both split-type and swirl-type spacer designs will be featured in this benchmark. **To aid mesh construction, CAD files of the spacer designs will be made available.** Following numerical simulation, participants will supply to the organizers results in the form of lateral (cross-stream) and axial velocity components, and turbulence intensity profiles at specified locations downstream of the spacer.

A synthesis of the results, including comparisons against measured data, will be carried out, and reported in the form of a Keynote Lecture at the forthcoming OECD/NEA-IAEA Workshop CFD4NRS-4, which will take place at the Daejeon Convention Center in the fall of 2012. Participants will have the opportunity to present their work in the form of a dedicated Poster Session at this workshop.

Those wishing to participate in the benchmark exercise are requested to register their interest with the OECD/NEA Secretariat: Abdallah.AMRI@oecd.org, with a copy to Brian.Smith@psi.ch. All registered participants will receive:

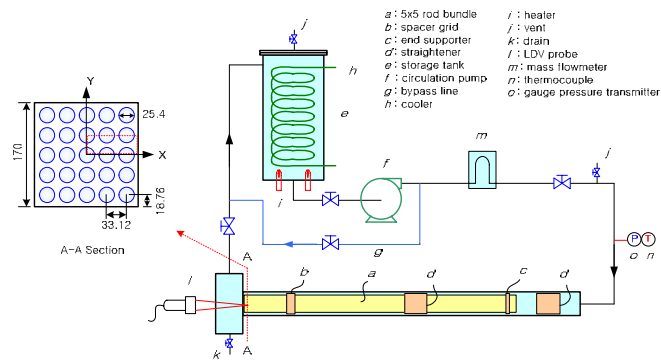
1. Further information and updates of the organization and progress of the benchmark activity;
2. A copy of the draft Benchmark Specifications, as soon as these are available.

The Specifications will be finalized at a **Kick-Off Meeting**, to be held at the NEA Headquarters in Paris, France on **Thursday, April 28, 2011**. Please register your attendance at this meeting in advance with the NEA Secretariat: Abdallah.AMRI@oecd.org, with a copy to Brian.Smith@psi.ch, so proper arrangements can be made. An agenda of the meeting will be circulated in due course.

### The KAERI Rod Bundle Experiment

The experiment is conducted in a water circulation loop at ambient pressure and temperature. The test section comprises a square Plexiglas sub-channel of inner dimensions 170 x 170 mm containing a 5x5 rod bundle array over part of its length. To enable good visualization of the lateral flow structure between the rods, the test section is fabricated 2.6 times larger than the prototypic size of PWR fuel bundles. The total channel length is 4900 mm and the section containing the rod bundle arrangement 1700 mm. A 2-D LDA system is positioned end-on to measure the lateral velocities in the bundle at every point in the flow sub-channel. The axial velocity component is measured by changing the location of the LDA probe to the side of the test section. The rods are arranged in a square lattice: the rod diameter is 25.4 mm, the pitch is 33.12 mm, and the wall pitch 18.76 mm. The measuring points were closely distributed with a resolution of 0.75 mm.

Flow is maintained by a water storage tank and circulation pump. The tank contains a heater and a cooler to maintain constant temperature conditions during operation of the loop. The water flow rate is controlled by changing the pump speed: maximum discharge 2 m<sup>3</sup>/min.



**Schematic of the MATIS-H Test Loop**  
 (MATIS-H: Measurements & Analysis of Turbulence in Subchannels - Horizontal)

### **Preliminary Agenda of the Kick-Off Meeting**

A detailed agenda is being compiled, but items to be included are:

- Plan of the Benchmark Activity      Brian L. Smith, PSI, Switzerland
- OECD/NEA requirements      Abdallah Amri, NEA, France
- Test Facility and Instrumentation      Chul-Hwa Song, KAERI, Republic of Korea
- Keynote Speaker      To be Announced
- Benchmark Specifications      Brian L. Smith
- Synthesis and Reporting Procedure      Chul-Hwa Song, KAERI, Republic of Korea
- Open Forum Discussion

### **Organising Committee**

Brian L. Smith, Paul Scherrer Institute, Switzerland  
Chul-Hwa Song, Korea Atomic Energy Research Institute, Republic of Korea  
Dominique Bestion, Commissariat à l’Energie Atomique, France  
Ghani Zigh, US Nuclear Regulatory Commission, USA  
John H. Mahaffy, US Nuclear Regulatory Commission, USA  
Abdallah Amri, OECD Nuclear Energy Agency, France (Secretariat)  
Milorad Dusic, IAEA, Vienna (co-sponsor).

### **Dates & Deadlines**

April 16, 2011	Registration for Attendance at Kick-Off Meeting
April 28, 2011-	Kick-Off Meeting of OECD/NEA – KAERI Benchmark
June 10, 2011	Distribution of Final Benchmark Specifications by Organizers
April 30, 2012	Deadline for Receipt of Simulation Results
May 31, 2012	Latest Date for Open Benchmark Meeting & Release of Test Data
Sept. 10, 2012	Presentation of Synthesis at CFD4NRS-4 Workshop

## ANNEX 2: SPECIFICATIONS

### OECD/NEA–MATiS-H BENCHMARK FINAL BENCHMARK SPECIFICATIONS

#### A0. PRELIMINARY REMARKS

Contained in this document are the final specifications of the benchmark, and supersede all previous versions.

The figures in this document are included for orientation purposes. High-quality versions of all figures on which dimensions need to be read are supplied in a separate .pdf file accompanying this text.

To aid mesh generation, new CAD files of both the split-type and swirl-type spacer grid geometries are also being supplied. These have been created using CATIA 5 software. File extension in both cases is .stp and is in ASCII format, so should be easily read by most grid generation packages. However, if participants wish to have .igs versions, or the original .CATPart files, these will be supplied upon request.

#### A1. GEOMETRICAL DATA

A schematic of the test facility, which is located at the Korea Atomic Energy Research Institute (KAERI), Daejeon, Korea, is illustrated in Fig. A1. This cold loop test facility, with the acronym MATiS-H (Masurement and Analysis of Turbulent Mixing in Subchannels – Horizontal), is used to perform hydraulic tests in a rod bundle array at normal pressure and temperature conditions. The rig consists of a water storage tank (*e*), a circulation pump (*f*) and a test section (*a*). The volume of the water storage tank and the maximum flow rate of the circulation pump are 0.9 m<sup>3</sup> and 2 m<sup>3</sup>/min., respectively. The flow rate in the loop during operation is controlled by adjusting the rotational speed of the pump, and the loop coolant temperature is also accurately maintained within a range of  $\pm 0.5^\circ\text{C}$  by controlling the heater (*i*) and the cooler (*h*) in the water storage tank. For monitoring and controlling the loop parameters (flow rate, pressure and temperature), a mass flowmeter (*m*), a gauge pressure transmitter (*o*) and a thermocouple (*n*) are installed at the inlet to the test section. The specifications of these instruments are given in Table A1.

Table A1: Instruments for loop monitoring and control.

Instrument	Model	Calibration Range	Instrument Accuracy
System Pressure ( $P_{\text{sys}}$ )	Rosemount 3051CG	0 ~ 350 kPa	$\pm 0.15\%$ of span
System Temperature ( $T_{\text{sys}}$ )	Watlow, T-type, Unground	0 ~ 350°C	$\pm 0.50^\circ\text{C}$
Mass Flow Rate ( $\dot{m}$ )	Micro Motion CMF300M	0 ~ 37.8 kg/s	$\pm 0.1\%$

The test section (*a*) consists of a 5x5 rod bundle array (*p*) installed in a horizontal position. Section A-A in Fig. A1 shows the cross-section of the rod bundle in the square duct (170 x 170 mm), comprising

25 rods of 25.4 mm outer diameter. The rods are deliberately selected to have a 2.67 times larger diameter than the real size (9.5 mm) of a fuel rod in order to improve the measurement resolution. The rod and the wall pitches are set at 33.12 mm and 18.76 mm, respectively, consistent with the increase in rod diameter. Consequently, the hydraulic diameter of the channel cross-section ( $D_H$ ), which considers the flow area and the wetted perimeter in a square duct including a 5x5 rod bundle, is 24.27 mm<sup>1</sup>. The test section has been installed in a horizontal position for convenience, there being no buoyancy-induced effects. Indeed, under isothermal conditions, the differences between vertical and horizontal orientation due to the gravitational effect are expected to be negligible.

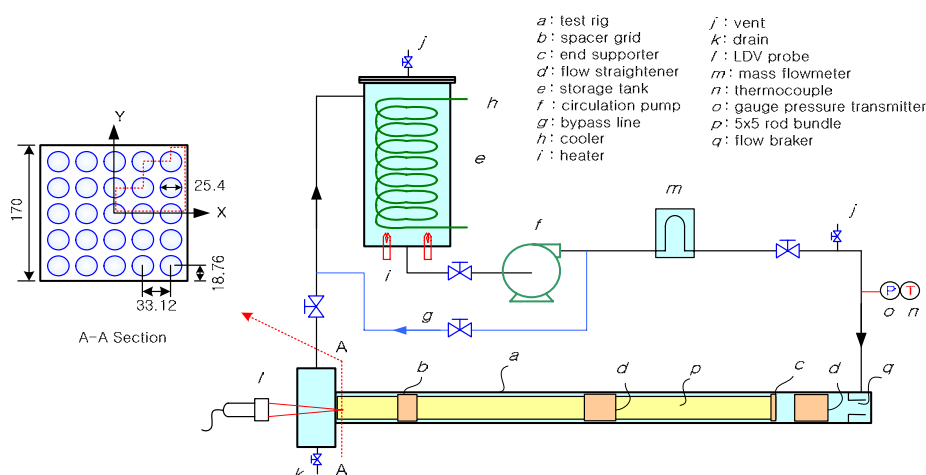


Figure A1: Schematic of MATiS-H test facility.

Water is supplied from the storage tank to the inlet to the test section by pump operation. The flow in the square duct first encounters a fixed flow straightener ( $d$ ), which comprises many small square channels in order to produce a uniform flow profile across the duct, without swirl. Downstream, the flow encounters the 5x5 rod bundle, producing a developing flow along the rods. Further downstream, there is a second flow straightener ( $d$ ), placed across the rod bundle, to redistribute the profile again to one of uniform flow. From this location, the flow advances to the spacer grid ( $b$ ), once more changing to a developing flow. There is sufficient distance ( $> 90 D_H$ ) between the 2<sup>nd</sup> flow straightener and the spacer grid for the flow to be expected to be fully developed. With this inlet flow condition at the upstream side of the spacer grid, the flow on the downstream side would be totally redistributed by the complicated vane arrangement of the spacer grid geometry.

A more detailed geometrical configuration of the test section itself is given in Fig. A2, with close-up details of the front end in Fig. A2a. The total length is 4970 mm, the most part made up of the square duct containing the 5x5 rod bundle. At the far upstream end, the inlet pipe ( $\phi$  105 mm) is attached vertically. Once the flow has been turned through 90°, in which a flow braker is positioned to make the flow profile less biased, it encounters the first of the flow straighteners, which is 150 mm long. A further 250 mm downstream is the start of the rod bundle. This extends over 3863 mm, and is fixed by support grids at both ends. The second flow straightener is located at a specified distance ( $S$  in Fig. A2) from the inlet plane of the spacer grid. The spacer grid dramatically enhances turbulent mixing in the sub-channels of the bundle due to the attached vanes at its downstream side. The main purpose of the MATiS-H experiment is to obtain accurate measurements of the cross-flows in the subchannels at various downstream locations from the spacer grid.

<sup>1</sup> $D_H = 4 * (\text{flow area}) / (\text{wetted perimeter}) = 4 * (170^2 - 25 * \pi / 4 * 25.4^2) / (25 * \pi * 25.4 + 4 * 170) = 24.27 \text{ (mm)}$

The measurement section is fixed at a position 10 mm upstream of the end of the rod bundle. This arrangement makes the installation and the calibration of the instruments more convenient. To increase the downstream distance ( $Z$ ) of the measurement section, the spacer grid can be moved upstream along its length (i.e. in the negative  $z$ -direction). For any location of the spacer grid in the rod bundle, the inlet flow conditions upstream of the spacer grid should be identical. This is as a consequence of the 2<sup>nd</sup> flow straightener. The distance  $S$  can be set to any specified value, but it is always considered advisable to have a fully developed flow profile at the inlet to the spacer grid. In this experiment,  $S$  is set at a minimum of  $100 D_H$ .

A three-legged drum ( $\phi$  560 mm, depth 290 mm) is attached at the downstream end of the square duct. A circular view window ( $\phi$  180 mm) has been fabricated at the end of the drum to enable LDA measurements of the cross-flow velocities to be made. The outlet flow from the drum is through the three outlet pipes, which are attached symmetrically (i.e. at  $120^\circ$ ) at its periphery.

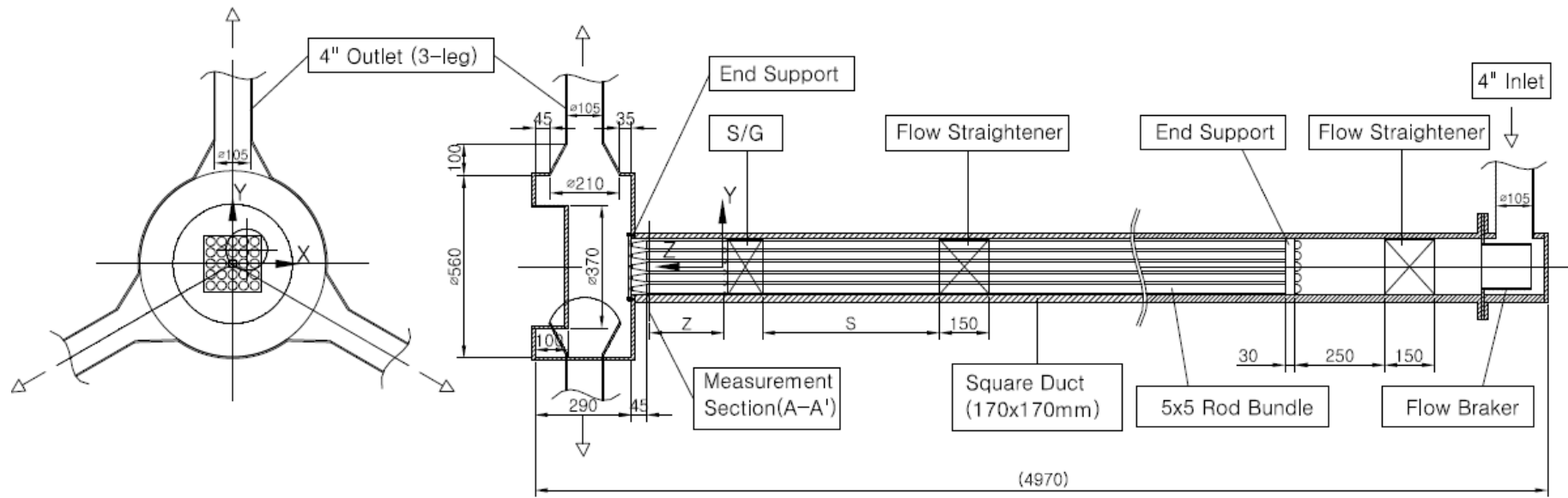


Figure A2: Geometrical data of the test section.

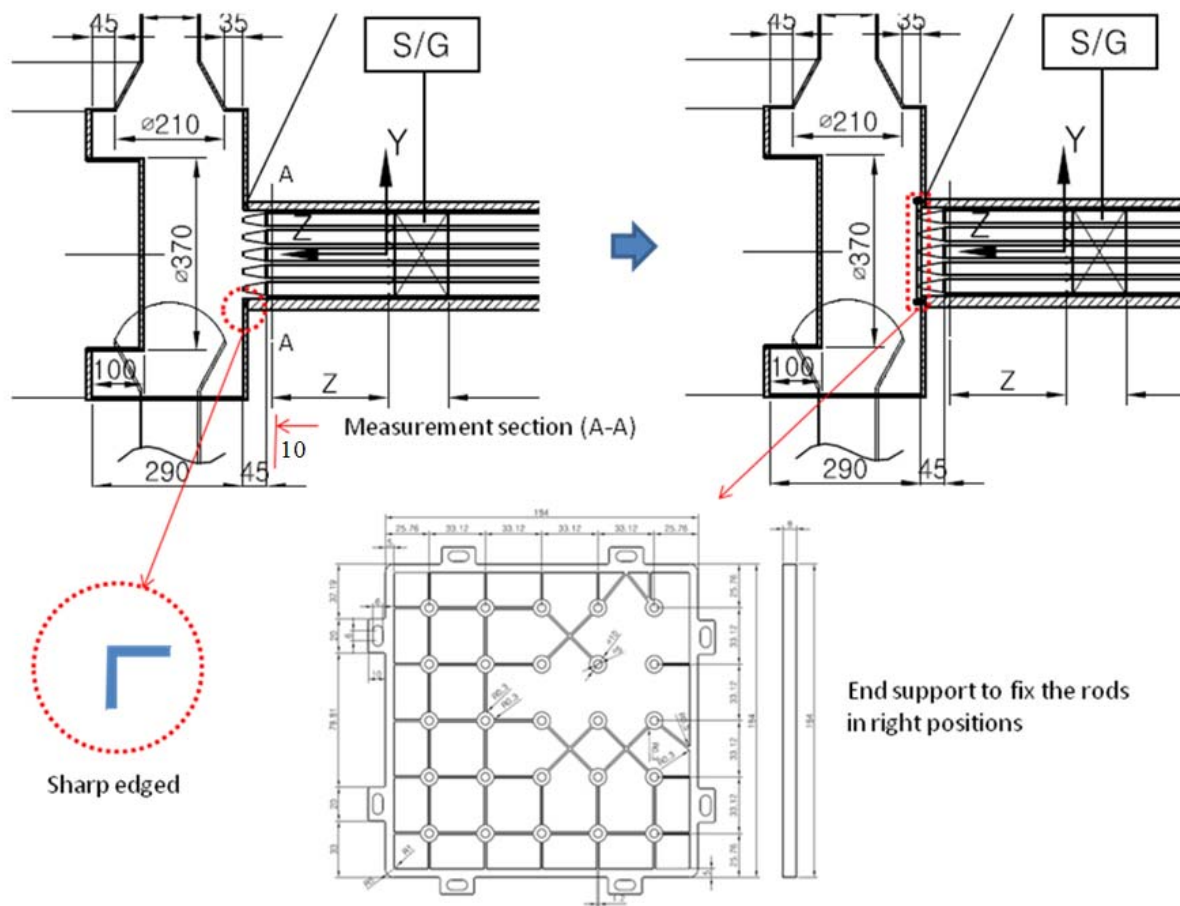


Figure A2a: Close-up details of the square duct outlet manifold connection.



fabrication, the standard flow straightener, illustrated in Fig. A5(a), has been divided into two pieces, and 25 holes machined into the grid to effect the rod penetration.

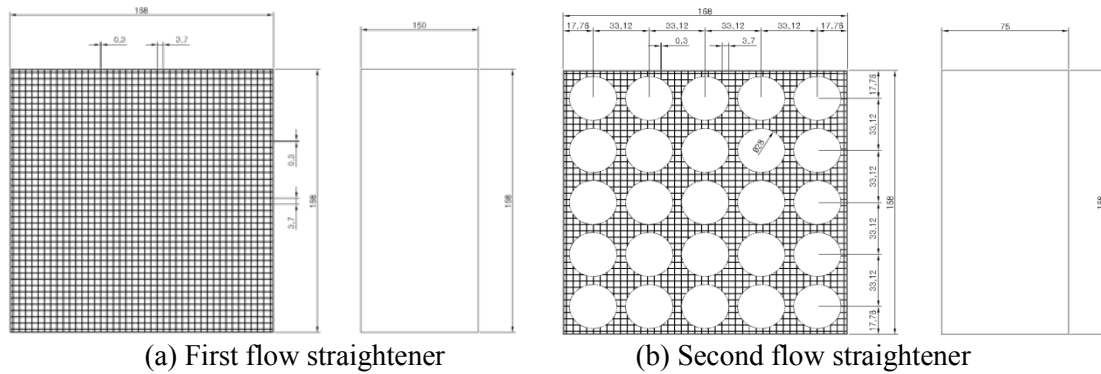


Figure A5: Geometrical data of the flow straighteners.

The detailed specifications of the spacer grids are shown in Figs. A6-A8. The basic common arrangement, except for the vane configuration, is given in Fig. A6. The strap thickness of the 5x5 square grid is 1.2 mm, and the grid length is 103.1 mm. There are 4x2 buttons in every square channel to fix each rod in the correct position.

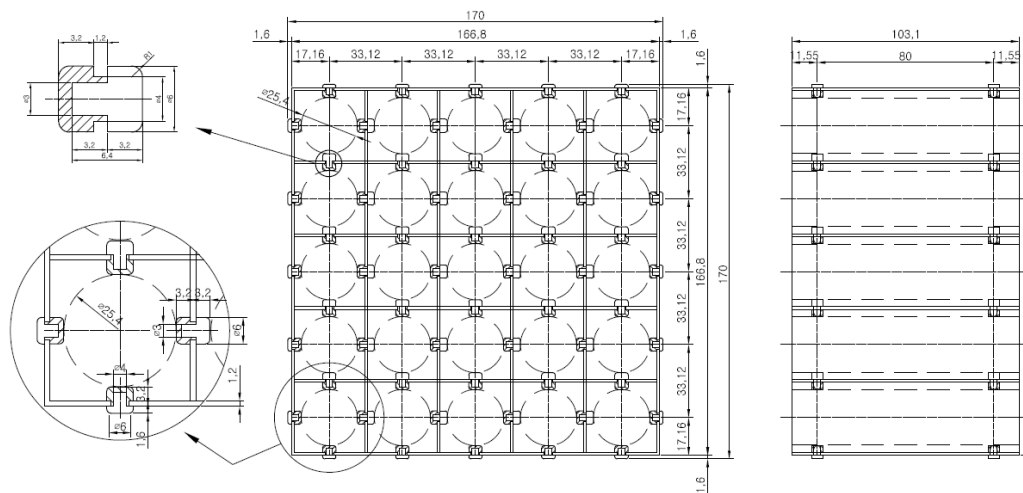


Figure A6: Geometrical data of the grid strap.

One of the spacer grids employed in this experimental series is of the “split-type”, which features two vanes at each crossing of the grid straps, as illustrated in Fig. A7. The vanes are bent through 30° with respect to the horizontal, as seen in Fig. A7(a), and each vane is oriented on the grid strap as illustrated in Fig. A7(b); the notations R, L, U and D depict the bending directions of the vanes according to Right, Left, Up and Down, respectively.

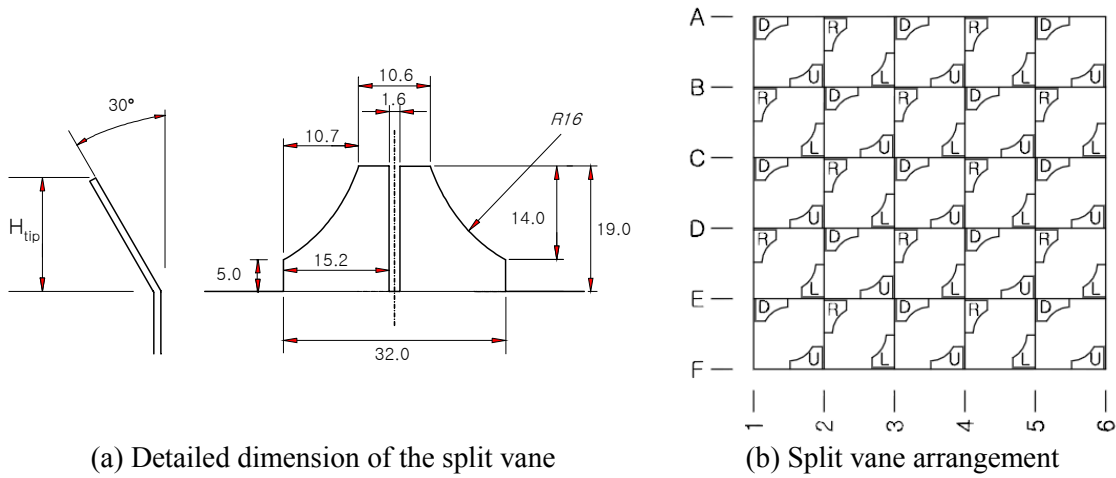


Figure A7: Geometrical data and arrangement of the split-vane spacer.

The other spacer grid is of the “swirl type”, which has four vanes at every cross of the grid strap, as seen in Fig. A8. In this case, the vanes are bent through 35°, based on the diagonal line, as shown in Fig. A8(a). Each vane is oriented on the grid strap as shown in Fig. A8(b), with the notations of R, L, U and D being as defined above.

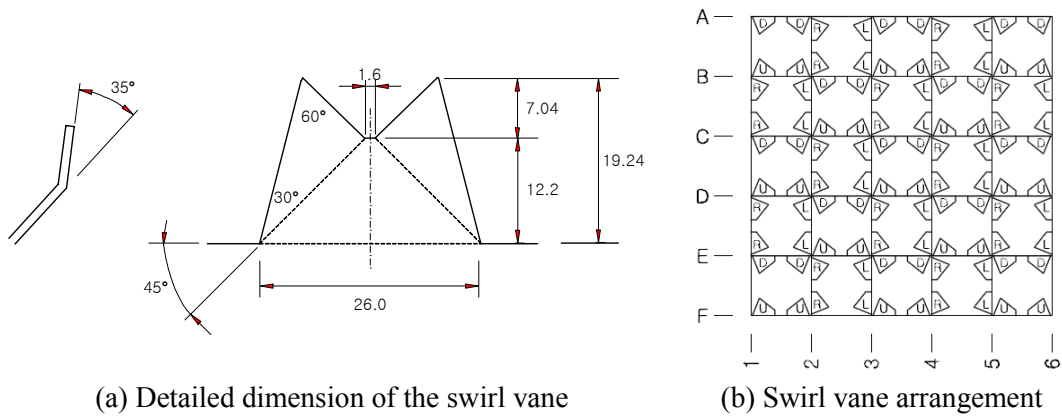
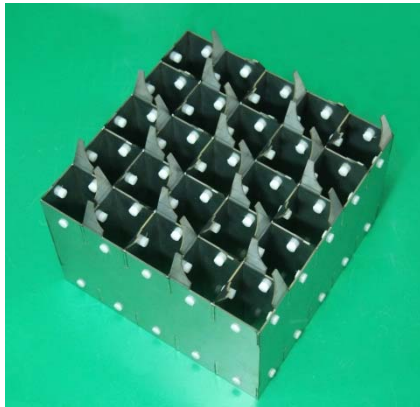
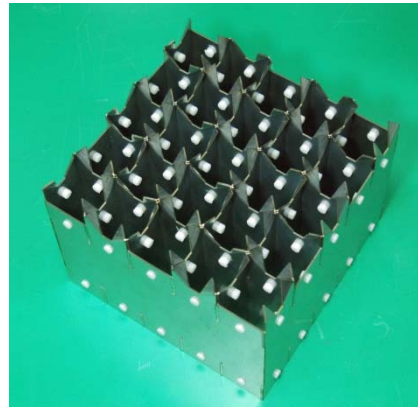


Figure A8: Geometrical data and the arrangement of the swirl vanes.

Visually, the fabricated spacer grids described in the text above appear as in Fig. A9.



(a) Split-type spacer grid



(b) Swirl-type spacer grid

Figure A9: Test spacer grids used in this experiment.

## A2. MATERIAL PROPERTIES

De-mineralized water is used as the working fluid in the experiment, the water temperature during operation being maintained at 35°C, at ambient pressure.

The enclosing material of the test section is made of stainless steel and acrylic. The upper plates of the square duct are made of acrylic plate, and the other parts constructed of stainless steel. All components included in the test section, i.e. the 5x5 rod bundle array, the spacer grid and flow straighteners, are made from stainless steel.

### A3. INLET BOUNDARY CONDITIONS

As noted before, fully developed flow conditions in the 5x5 rod bundle geometry are anticipated upstream of the spacer grid in this experiment. To confirm this, an additional experiment has been conducted, with details as follows. The inlet length of about  $100 D_H$  upstream of the spacer grid was originally chosen to ensure fully developed flow on the upstream side of the spacer grid. However, it is nonetheless desirable to have an inlet boundary condition at about  $10 D_H$  upstream of the spacer grid from the viewpoint of the CFD simulations. Consequently, a flow profile at  $90 D_H$  has been given for use as the inlet boundary condition for the CFD calculations.

To measure details of the flow profile at  $90 D_H$ , an additional experiment has been performed using a LDA system, as illustrated in Fig. A10. Here, the flow straightener is placed  $90 D_H$  upstream of the A-A measurement section, but with the spacer grid removed, as shown in Fig. A10(b). For the measurements of the axial velocity profile, the LDA probe is placed at the side wall of the test rig as shown in Fig. A10(a). The measurements are restricted to the gap regions in the inner subchannels due to the blockage of the beam caused by the rod structures in the 5x5 rod bundle array. Therefore, the measurement region was taken with the three gap regions at a quadrant section marked in red in Fig. A10(c).

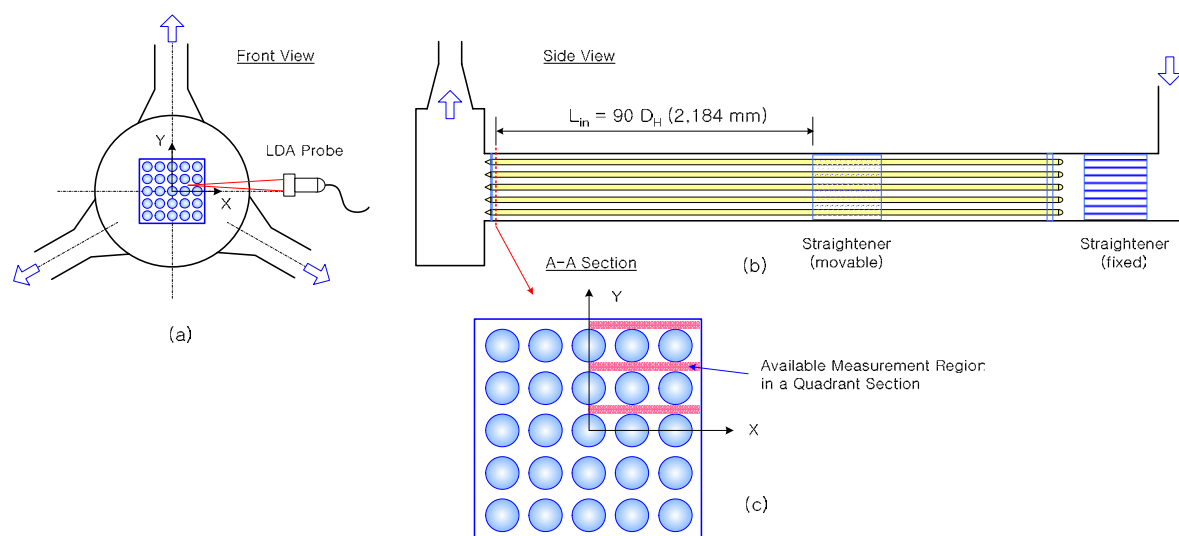


Figure A10: Axial velocity ( $W$ ) measurements (in 1/4 section).

During the test to determine the inlet boundary conditions, the temperature of the test rig was maintained at the target value ( $35^{\circ}\text{C}$ ) using the heater and cooler in the water storage tank. The mass flow rate was also maintained by keeping the inverter at a constant frequency of the circulation pump. Consequently, the loop parameters were properly controlled during the test. These loop conditions also gave stable flow parameters for bulk velocity and Reynolds number. The mean values, and their uncertainties, of the loop operating conditions are summarised in Table A2.

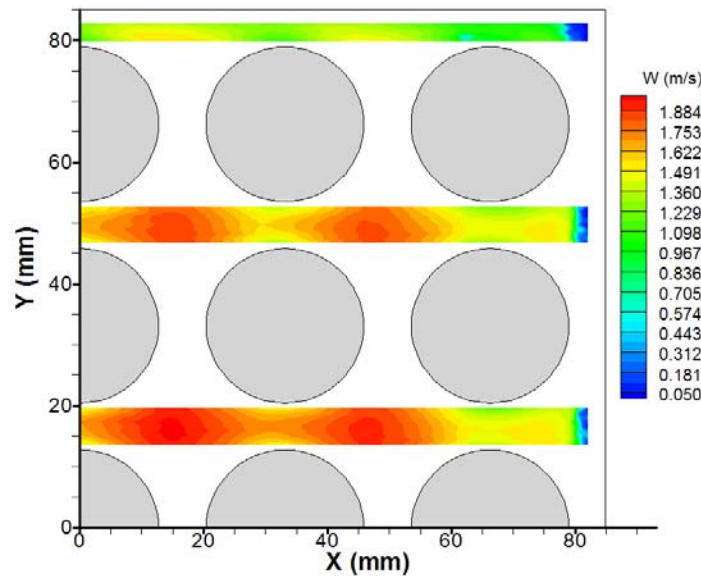
Table A2: Loop operating conditions.

Parameter		Mean Value	Overall Uncertainty (%)	Measuring Location
Loop Parameter	Mass Flow Rate (kg/s)	24.2	0.29	Pump Discharge
	Temperature (°C)	35	2.90	Test Rig Inlet
	Pressure (kPa)	156.9	0.39	Test Rig Inlet
Flow Parameter	Bulk Velocity, $W_{Bulk}$ (m/s)	1.50	0.37	Test Section
	Reynolds Number, $Re^{\#}$	50 250	2.01	Test Section

$$\# Re = \frac{\rho \cdot W_{Bulk} \cdot D_H}{\mu}$$

The axial ( $z$ -direction) velocities, and their turbulence properties in terms of the turbulence intensity, have been measured simultaneously using the above LDA set-up. The available measurement region in the quadrant section in Fig. A10 is comprised of three gaps (i.e. lower gap, middle gap and upper gap). For a precision measurement, nine measurement lines were deployed in the  $y$ -direction for the lower and the middle gaps, and five measurement lines were arranged for the upper gap. Each measurement line has 110 equally spaced measurement points (0.75 mm resolution). Therefore, the total number of measurement points for the available measurement region in the quadrant section is 2530 ( $= 110 \times 9 + 110 \times 9 + 110 \times 5$ ). The measurement section in the test rig is placed at the 10 mm inner location of the outlet end of the 5x5 rod bundle, as shown in Fig. A2a.

From all the measurements taken in the available region of the quadrant section, the axial velocity contour can be mapped, as shown in Fig. A11.

Figure A11: Contours of the mean axial velocity ( $W$ ) in the quadrant section.

The peaks of the axial velocity in the subchannels occur at around the centres of the open flow regions, but with some degree of bias against the wall. The velocity profiles have been extracted from the above contour map, as described below. All the velocity components are normalized with respect to the bulk velocity,  $W_{bulk}$  (1.50 m/s). For convenience, the lengths in the  $xy$ -plane are scaled with respect to the rod-to-rod pitch,  $P$  (33.12 mm), while the lengths in  $z$ -direction are scaled with respect to the hydraulic diameter,  $D_H$  (24.27 mm). Figure A12 shows the locations of the measurement lines in the three gaps in the quadrant section, as shown in A10(c), based on the normalized scales.

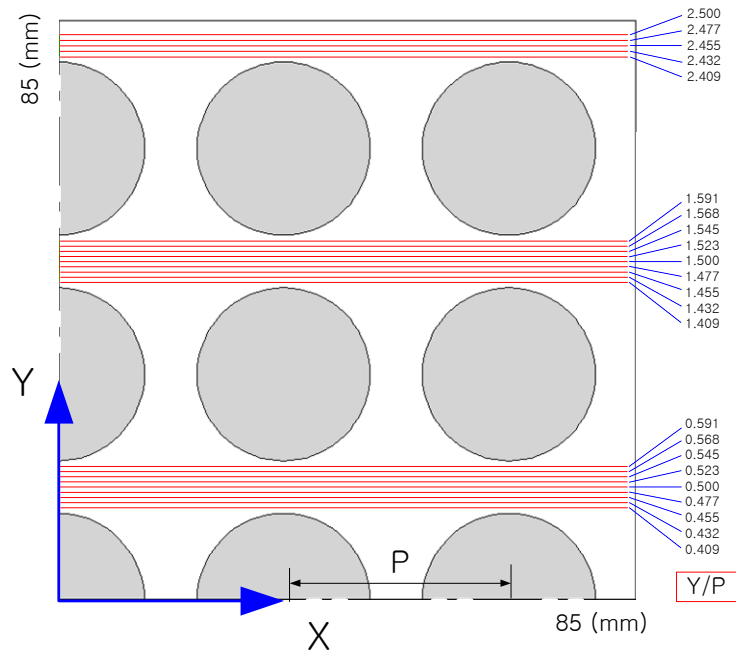
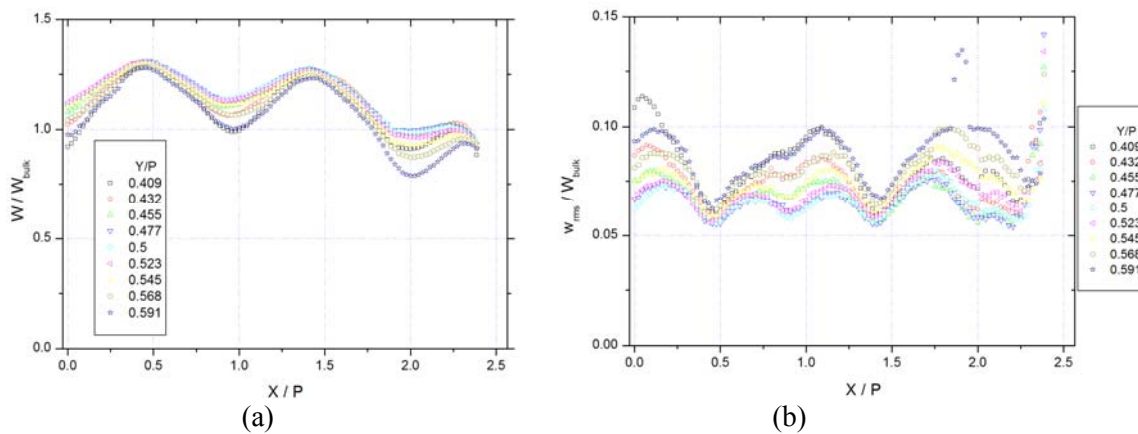


Figure A12: LDA measurement trajectories in the quadrant section.

Figure A13 gives the axial velocities and their turbulence intensity profiles along each measurement trajectory. The waviness of the velocity profiles reflects the geometrical configurations of the rods, and the presence of the wall in the flow channel, as could be easily anticipated. The axial turbulence intensities are mostly in the range from 5% to 10% of the axial bulk velocity, depending on the rod-to-wall distance.



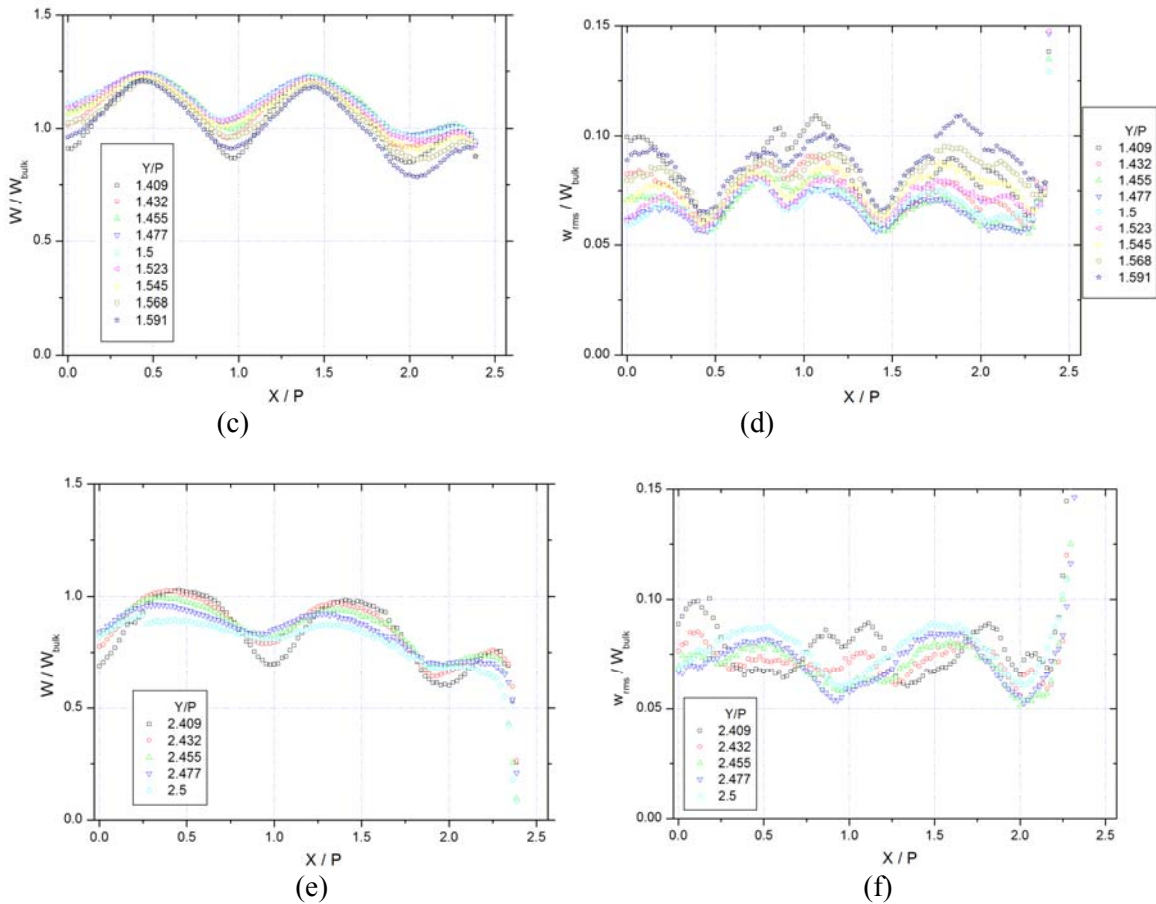


Figure A13: Velocity and turbulence intensity profiles in each measurement trajectory at the three gaps: (a), (b) in the lower gap; (c), (d) in the middle gap; (e), (f) in the upper gap.

For these LDA measurements, the data quality in the near-wall region was identified to be much lower than for the measurements taken away from the wall, because of the beam dispersion close to the duct wall.

The definitions of the mean velocity and the turbulence intensity used in this test are given as follows:

$$\text{Mean} \quad W = \bar{w} = \frac{1}{n} \sum_{i=1}^n w_i$$

$$\text{RMS} \quad W_{rms} = \left\{ \overline{(w - \bar{w})^2} \right\}^{1/2}$$

Three measurement trajectories, those representing the centrelines in each gap, have been selected to highlight the turbulent properties of the flow in a typical rod bundle, as illustrated in Fig. A14. Figure A14(a) shows the differences in the axial velocity profiles along the centrelines for each of the three gaps. These reflect the positioning of the rods and the presence of the wall in the flow channel. The turbulence intensity distributions shown in Fig. A14(b) are restricted to the range 5% to 8% of the axial bulk velocity. Figure A14(c) shows the presence of small inward-directed, vertical cross-flows in the subchannels. The turbulence intensities of these cross-flows are at a level of 5% of the axial bulk velocity, as given in Fig. A14(d). Reynolds stress data for the two measured velocity components  $V$  and  $W$  are shown in Fig. A14(e).

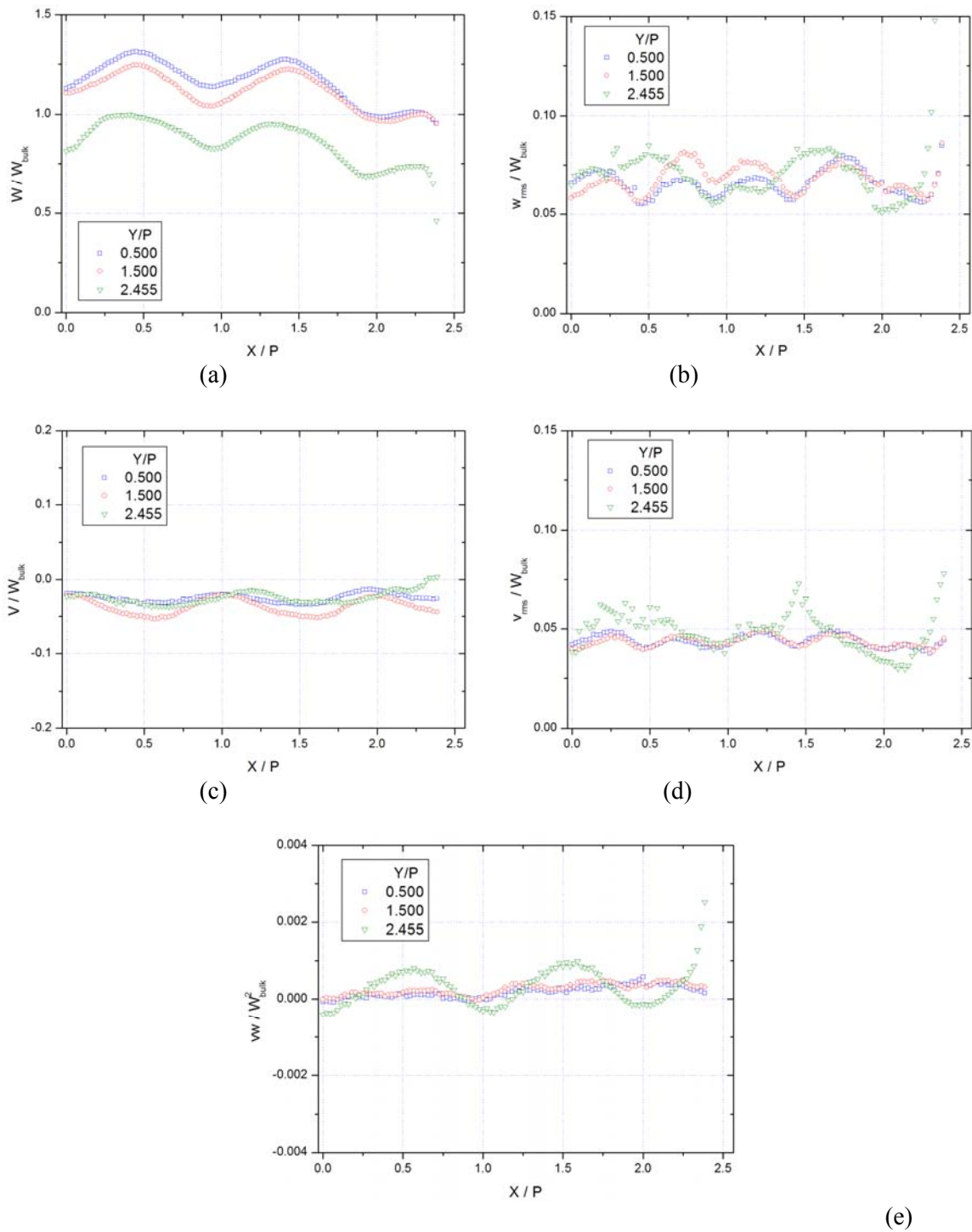


Figure A14: Flow properties along the centrelines of the three gaps:  
 (a) axial velocity profiles; (b) axial turbulence intensity profiles; (c) vertical cross-flow profiles;  
 (d) vertical turbulence intensity profiles; (e) Reynolds stress distributions.

For analyzing the uncertainties in the LDA measurements, two types of uncertainties (i.e. random and systematic errors) have been considered. The factors contributing to the systematic uncertainty include the uncertainty due to the resolution of the motorized stage, the alignment of the LDA probe, and the LDA

instrument uncertainty itself. Consequently, the combined uncertainty with 95% confidence level of the LDA velocity measurements in this upstream test is estimated to be between 4.8% and 5%.

All the data presented in Figs. A13 and A14 are also available in tabular form in the Appendix to this document. For convenience, electronic versions of these data are also provided to the participants in the form of Excel files.

## A4. DOWNSTREAM NUMERICAL DATA REQUESTED

### A4.1 Introduction

It is hoped that most participants will submit calculated results for both the split-type and the swirl-type spacer grid geometries, though results for just one type will be accepted and included in the synthesis. For participants who wish to submit the results for just one type, the split-type spacer grid is recommended.

Only very basic quantities are requested from this benchmark, to permit flexibility in the choice of summary results, and to ensure uniform processing of the results. Prior to the reporting of the data requested, for those participants who pursue a transient modelling approach, it is their own responsibility to run a long enough time interval for time-averaged quantities to become statistically meaningful.

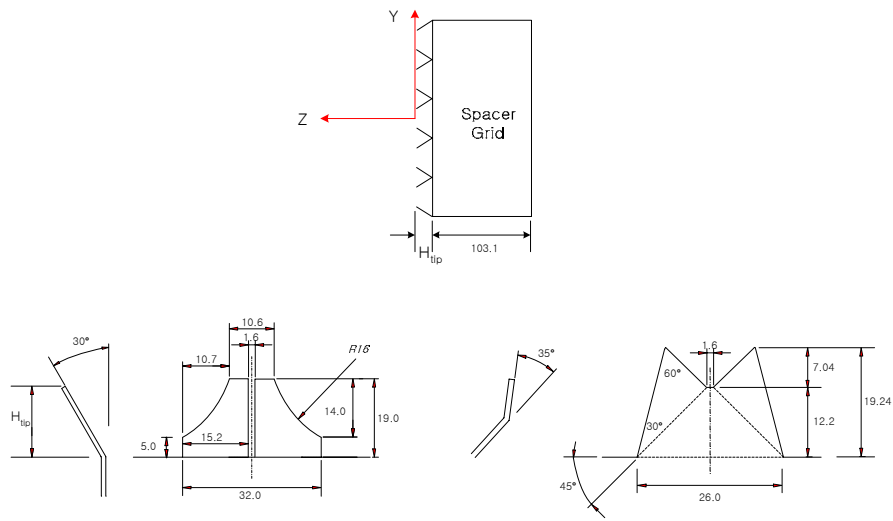
In addition to the basic data, we request characterization of the CFD methodology and mesh in an accompanying document. An example is supplied in the file *Information.doc*, which should be used as a template. Note that the information requested includes: the order(s) of the numerical scheme(s); the total number of volumes used in the calculation; the range of  $y^+$  (wall-normal coordinate); minimum cell edge length; maximum cell edge length; details of the turbulence model used; computer resources and calculation time; vorticity contours; and files supplied for synthesis.

### A4.2 Coordinate System used for Reporting

The same Cartesian coordinate system developed for earlier tests in this facility will be used, as seen in the A-A Section of Fig. A1, the  $x,y,z$  coordinates forming a right-handed set with  $z$  increasing in the direction of flow and  $y$  vertically upwards. The origin of the coordinate system is the geometric centre of the cross-plane of the tips of the vanes of the spacer grid, as shown on Fig. A15. Note that the distance  $H_{tip}$ <sup>2</sup> is different for the split and swirl spacer grid types, the values being indicated in Fig. A15. In the following discussion, the standard notation of  $u,v,w$  for the  $x,y,z$  components of velocity, respectively, are used.

---

<sup>2</sup> These values are estimated ideally from the dimensions of the drawing. However, in the CAD files provided, which reflect the dimensions of the actual fabricated objects, these values can be slightly different due to the unavoidable curvature at the bending line during the fabrication process. Please note that downstream experiments will be performed with the coordinate determined by the vane tip end of the actual fabricated objects shown in the CAD files.



$$H_{tip} = 19 \cdot \cos(30^\circ) = 16.45 \text{ mm}$$

Split-vane type

$$H_{tip} = 12.20 + 7.04 \cdot \cos(35^\circ) = 17.97 \text{ mm}$$

Swirl-vane type

Figure A15. Origin and orientation of the coordinate system to be used.

### A4.3 Time-Averaged Data to be Reported

Participants should be prepared to supply information in the cross planes  $0.5 D_H$ ,  $1.0 D_H$ ,  $4.0 D_H$  and  $10.0 D_H$  from the downstream face of the spacer grid, as shown in Fig. A15. Participants are requested to provide:

- time-averaged values for all three velocity components in the measuring planes;
- time-averaged rms values of the fluctuating components of all three velocity components;
- the circulation in one sub-channel  $\Gamma = \iint \omega_z dx dy$ , where  $\omega_z$  is the z-component of vorticity.

The integration is to be carried out for the sub-channel marked in Fig. A16.

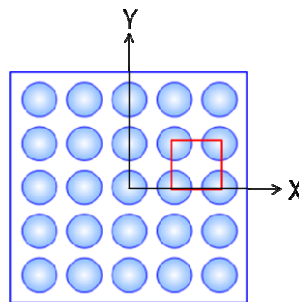


Figure A16: The subchannel (marked in red) for calculating the flow circulation.

All the results, except the circulation, should be reported along the three line segments:  $y = 16.56 \text{ mm}$ ,  $49.68 \text{ mm}$  and  $81.29 \text{ mm}$  in the region marked in red in Figs. A1 (left) and A4. Hereafter,  $y_1$ ,  $y_2$ ,  $y_3$  denote the three y-direction positions:  $y = 16.56 \text{ mm}$ ,  $49.68 \text{ mm}$  and  $81.29 \text{ mm}$ , respectively.

### A4.3.1 Time-Averaged Data File Formats

All files shall be written in ASCII text format, with space-delimited fields. Time-averaged values shall be written with 8 significant digits (e.g. 1.2345678 or 1.2345678E-2). Values for times and locations may be written with fewer significant digits, if appropriate.

The first column in the files for the time-averaged data is for the  $x$ -positions at which the values for the mean velocity components and their fluctuating components are located; the values of  $x$ -positions are to be given in mm, and all the values relating to the velocities are to be given in m/s. The second column shall contain time-averaged values for the  $x$ -component of velocity  $u; \bar{u}$  at the locations provided in the first column. The third column shall contain time-averaged values for the  $y$ -component of velocity  $v; \bar{v}$ , and the fourth column the time-averaged values of the  $z$ -component of velocity  $w; \bar{w}$ . Columns five through seven shall contain time-averaged rms values of the  $x,y,z$  components of the velocity fluctuations  $u',v',w'$ , respectively.

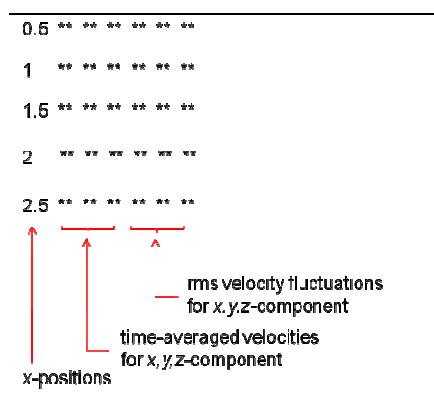


Figure A17: Example of the format of the files containing time-averaged velocity data.

Also, one additional file, entitled *circulation.dat*, shall be supplied for the circulation in the sub-channel marked in red in Fig. A16. The first column in the file is for the four  $z$ -positions (i.e. downstream cross-sections) at which the circulations have been calculated ( $0.5D_H$ ,  $1.0D_H$ ,  $4.0D_H$  and  $10.0D_H$ ), and then the subsequent column shall contain the value of the circulation at the  $z$ -locations provided in the first column; the values of  $z$ -positions are to be given mm, and the values of the circulation are to be given in  $m^2/s$ .

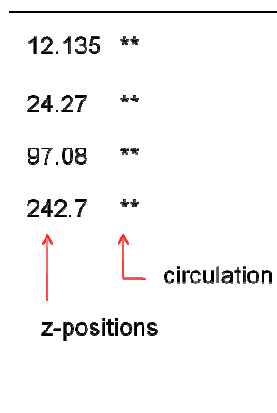


Figure A18: Example of the format of file giving the circulation, as defined in Section A4.3.

### A4.3.2 Time-Averaged Data File Names

To enable automated processing of results, all data files must follow the same naming convention. Files shall be generated according to the axial location used to sample the data in the experiment. The specific file names are to be as follows:

avg0.5Dz\_y1.txt time-averaged data 0.5 diameters downstream of the spacer grid at y = 16.56 mm  
 avg0.5Dz\_y2.txt time-averaged data 0.5 diameters downstream of the spacer grid at y = 49.68 mm  
 avg0.5Dz\_y3.txt time-averaged data 0.5 diameters downstream of the spacer grid at y = 81.29 mm  
 avg1.0Dz\_y1.txt time-averaged data one diameters downstream of the spacer grid at y = 16.56 mm  
 avg1.0Dz\_y2.txt time-averaged data one diameters downstream of the spacer grid at y = 49.68 mm  
 avg1.0Dz\_y3.txt time-averaged data one diameters downstream of the spacer grid at y = 81.29 mm  
 avg4.0Dz\_y1.txt time-averaged data 4 diameters downstream of the spacer grid at y = 16.56 mm  
 avg4.0Dz\_y2.txt time-averaged data 4 diameters downstream of the spacer grid at y = 49.68 mm  
 avg4.0Dz\_y3.txt time-averaged data 4 diameters downstream of the spacer grid at y = 81.29 mm  
 avg10.0Dz\_y1.txt time-averaged data 10 diameters downstream of the spacer grid at y = 16.56 mm  
 avg10.0Dz\_y2.txt time-averaged data 10 diameters downstream of the spacer grid at y = 49.68 mm  
 avg10.0Dz\_y3.txt time-averaged data 10 diameters downstream of the spacer grid at y = 81.29 mm

The above files shall all be placed in a directory entitled *Split* or *Swirl*, according to the grid-spacer type considered. Also, each directory shall contain a file entitled *circulation.dat*, as explained in Section A4.3 above.

### A4.4 Transmission of Results

Start by creating a text file named *Information.doc* using the supplied template. The first line of the file is to contain a comma-delimited list of the authors of the study. The second line is to contain the name of your parent organization, and the third line is to contain the name of the CFD program that you used. The fourth line is to contain an acronym, or brief phrase, describing your choice of turbulence modelling. For example:

B. Smith, G. Zigh  
 OECD/NEA  
 ANSYS-CFX  
 SAS-SST

Use GNU, tar or a zip utility to create a compressed archive containing *Information.doc* and the two directories entitled *Split* and/or *Swirl*, each containing the 12 files of time-averaged values, and the one file for the circulation values, as described in Section A4.3.1.

The file shall have a name that begins with “MATISHResults”, followed by a hyphen, followed by the initials of the first listed participant, followed by another hyphen, followed by initials for the participating organization. The suffix for the file name will be either tgz or zip. Examples are “MATISHResults-JHM-USNRC.tgz” or “MATISHResults-BS-PSI.zip”

## A5. CONCLUDING REMARKS

### A5.1 Organizing Committee

Brian L. Smith, Paul Scherrer Institute, Switzerland  
Chul-Hwa Song, Korea Atomic Energy Research Institute, Republic of Korea  
Dominique Bestion, Commissariat à l'Énergie Atomique, France  
Ghani Zigh, US Nuclear Regulatory Commission, USA  
John H. Mahaffy, US Nuclear Regulatory Commission, USA  
Abdallah Amri, OECD Nuclear Energy Agency, France (Secretariat)

### A5.2 Schedule

April 28, 2011	Kick-Off Meeting
June 17, 2011	Distribution of Geometric Specifications by Organizers
June 30, 2011	Deadline for Queries and Comments from Participants
July 15, 2011	Distribution of Final Benchmark Specifications by Organizers
May 15, 2012	Deadline for Receipt of Simulation Results
May 31, 2012	Latest Date for Open Benchmark Meeting and Release of Test Data
Sept. 10, 2012	Presentation of Synthesis at CFD4NRS-4 Workshop

A preliminary version of the benchmark specifications giving the precise geometry data was distributed on June 17, 2011. Participants were requested to communicate any queries/comments within 15 days. The inquiries which were made by participants were all answered by the organizers, and clarifications embodied into this document. The participants have 10 months to perform the simulations, and to submit their results to the organizers.

This benchmark activity is an integral part of the CFD4NRS-4 Workshop, and the scheduling is part due to the timing of this event in the Autumn of 2012. However, it is intended to release the data ahead of this time to enable participants to assess, and perhaps build on, their *blind* predictions. Consequently, an Open Benchmark Meeting, to take place in Paris, will be organized in May 2012, at which time the measured data downstream of the spacer grid will be released for the first time.

The synthesis of the blind benchmark results will be undertaken by KAERI, who will present their findings in an Invited Lecture at the CFD4NRS-4 Workshop, which will take place in Daejeon, S. Korea on 10-12 September 2012. The Workshop will be under joint OECD/NEA and IAEA promotion. A paper will also be prepared to accompany the Invited Lecture, and will be part of the official conference proceedings to be issued by the OECD/NEA during 2013.

It is hoped that many participants will take the opportunity to display their results at this Workshop, and a special *Poster Session* will be organized for this purpose. It will not be necessary to produce an accompanying paper in support of the poster. However, if more than the blind benchmark simulation has been undertaken, for example a comparison of several turbulence modelling approaches, and/or results following the application of Best Practice Guidelines, a full paper can be submitted to the Workshop in the usual way for consideration for inclusion in the technical programme. The numbers of such papers will be restricted, however.

### A5.3 Submittal Procedures

In order to be able to efficiently handle and compare calculated and measured data, all participants are requested to adhere STRICTLY to the formatting requested in Section A4. Datasets not conforming to the specified norms will be returned to the participant for correction. As an aid to submission, a script (most likely written in Python, [www.python.org](http://www.python.org)) will be issued to all participants. It is a requirement of all participants that their data sets can be read by the script prior to submission in order to verify data compatibility. Failure to do this may result in the deletion of the submitted data ahead of the deadline date from the set chosen for synthesis.

The deadline for submission of code predictions is May 15, 2012. Earlier submissions will be very welcome, and will considerably ease the burden on the organizers. Later submissions will be accepted, or refused, at the discretion of the organizing committee. Only one submission per participant will be processed.

A special dropbox will be created on the KAERI website to which participants will be able to upload their results. Details will be distributed once the webpage is functional. Individual usernames and passwords will be allocated, and all data sets will be regarded as confidential. Complete access to the data will only be available to the benchmark organizers. After uploading, participants are advised to download their datasets and compare with the originals to ensure that perfect transmission has been accomplished. Each participant will have the opportunity to exchange the dataset submitted for a newer version, but only up to the time of the deadline (May 15, 2012) at which time no further access to the dropbox will be possible. After the test data are released at the Open Benchmark Meeting in the second half of May 2012 (actual date to be announced), no further submissions will be accepted. Additionally, participants will thereafter not be permitted to withdraw their submissions.

Participants are free to repeat their calculations once they have the test data, and display any new results at the special Poster Session at the CFD4NRS-4 Workshop, as desired. However, only the *blind* code predictions will be considered for the synthesis.

### REFERENCES

Chang, S.K., Moon, S.K., Baek, W.P. and Choi, Y.D., "Phenomenological investigations on the turbulent flow structures in a rod bundle array with mixing devices", *Nucl. Eng. Des.*, **238**, 600-609 (2008).

Kang, H. S., Chang, S. K. and Song, C.-H., "CFD analysis of the MATIS-H experiments on the turbulent flow structures in a rod bundle with mixing vanes", Proc. CFD4NRS-3, Washington, D.C., USA, Sept. 14-16, 2010.

## APPENDIX: TABLES OF INLET VELOCITY DATA

(Note that distances are scaled according to rod pitch ( $P = 33.12$  mm))

## 1. UPSTREAM DIGIT DATA (Figure A13)

a)  $W/W_{\text{bulk}}$ 

X/P	Y= 0.409P	Y= 0.432P	Y= 0.455P	Y= 0.477P	Y= 0.5P	Y= 0.523P	Y= 0.545P	Y= 0.568P	Y= 0.591P
0.000	0.921	1.021	1.081	1.107	1.116	1.125	1.103	1.042	0.977
0.023	0.936	1.035	1.087	1.113	1.125	1.137	1.110	1.055	0.975
0.045	0.957	1.044	1.099	1.127	1.136	1.145	1.124	1.063	0.990
0.068	0.986	1.062	1.109	1.140	1.147	1.155	1.128	1.070	1.016
0.091	1.013	1.080	1.135	1.149	1.151	1.166	1.142	1.089	1.024
0.114	1.042	1.106	1.150	1.163	1.163	1.173	1.154	1.098	1.047
0.136	1.067	1.125	1.162	1.172	1.181	1.189	1.169	1.114	1.078
0.159	1.097	1.143	1.171	1.190	1.190	1.199	1.180	1.127	1.087
0.182	1.118	1.160	1.188	1.205	1.200	1.213	1.190	1.143	1.108
0.205	1.139	1.176	1.199	1.217	1.210	1.223	1.207	1.159	1.129
0.227	1.164	1.195	1.213	1.228	1.226	1.240	1.216	1.168	1.139
0.250	1.182	1.210	1.228	1.239	1.233	1.247	1.227	1.181	1.152
0.273	1.198	1.226	1.242	1.249	1.243	1.257	1.239	1.200	1.172
0.295	1.218	1.239	1.252	1.259	1.256	1.266	1.250	1.219	1.187
0.318	1.234	1.252	1.264	1.270	1.265	1.273	1.263	1.230	1.221
0.341	1.249	1.267	1.275	1.280	1.280	1.287	1.277	1.242	1.243
0.364	1.265	1.279	1.288	1.290	1.287	1.296	1.286	1.254	1.257
0.386	1.273	1.290	1.296	1.301	1.297	1.301	1.293	1.276	1.271
0.409	1.285	1.296	1.302	1.304	1.301	1.305	1.297	1.277	1.276
0.432	1.289	1.301	1.307	1.305	1.305	1.306	1.300	1.281	1.279
0.455	1.291	1.303	1.307	1.310	1.310	1.307	1.299	1.284	1.281
0.477	1.287	1.300	1.308	1.309	1.307	1.305	1.298	1.285	1.277
0.500	1.282	1.290	1.303	1.305	1.302	1.295	1.291	1.281	1.270
0.523	1.276	1.282	1.301	1.296	1.298	1.291	1.283	1.270	1.261
0.545	1.266	1.274	1.284	1.285	1.285	1.283	1.274	1.263	1.248
0.568	1.255	1.262	1.271	1.282	1.275	1.269	1.264	1.249	1.232
0.591	1.243	1.253	1.260	1.269	1.269	1.259	1.254	1.236	1.223
0.614	1.233	1.242	1.250	1.264	1.254	1.250	1.241	1.222	1.206
0.636	1.218	1.231	1.240	1.252	1.245	1.240	1.231	1.217	1.199
0.659	1.206	1.219	1.229	1.243	1.237	1.231	1.217	1.200	1.182
0.682	1.190	1.206	1.221	1.235	1.223	1.220	1.208	1.190	1.170

0.705	1.173	1.187	1.204	1.223	1.211	1.207	1.196	1.175	1.154
0.727	1.155	1.176	1.190	1.213	1.202	1.197	1.181	1.165	1.137
0.750	1.139	1.161	1.177	1.200	1.193	1.186	1.174	1.150	1.126
0.773	1.117	1.143	1.165	1.188	1.180	1.174	1.161	1.141	1.109
0.795	1.095	1.125	1.150	1.177	1.170	1.161	1.148	1.128	1.090
0.818	1.074	1.109	1.141	1.164	1.159	1.152	1.137	1.114	1.072
0.841	1.053	1.094	1.127	1.152	1.148	1.146	1.129	1.098	1.058
0.864	1.034	1.082	1.117	1.147	1.143	1.138	1.121	1.090	1.039
0.886	1.018	1.073	1.109	1.139	1.141	1.133	1.113	1.081	1.027
0.909	1.005	1.067	1.104	1.132	1.138	1.131	1.111	1.072	1.018
0.932	0.995	1.062	1.106	1.133	1.138	1.131	1.111	1.067	1.011
0.955	0.989	1.062	1.107	1.131	1.140	1.134	1.109	1.064	1.004
0.977	0.992	1.068	1.111	1.132	1.144	1.137	1.113	1.066	1.003
1.000	0.994	1.071	1.118	1.140	1.148	1.141	1.118	1.068	1.007
1.023	1.004	1.080	1.123	1.146	1.154	1.144	1.117	1.074	1.016
1.045	1.016	1.091	1.133	1.154	1.160	1.151	1.126	1.080	1.021
1.068	1.035	1.103	1.141	1.160	1.167	1.156	1.134	1.088	1.032
1.091	1.052	1.116	1.152	1.166	1.173	1.164	1.141	1.099	1.046
1.114	1.076	1.128	1.162	1.180	1.179	1.170	1.146	1.103	1.060
1.136	1.095	1.145	1.172	1.188	1.191	1.180	1.154	1.112	1.071
1.159	1.117	1.158	1.180	1.196	1.197	1.186	1.162	1.121	1.085
1.182	1.133	1.173	1.193	1.203	1.204	1.194	1.171	1.136	1.106
1.205	1.154	1.185	1.205	1.216	1.214	1.204	1.186	1.150	1.126
1.227	1.170	1.199	1.216	1.224	1.224	1.211	1.195	1.156	1.140
1.250	1.188	1.214	1.227	1.236	1.233	1.222	1.207	1.175	1.158
1.273	1.202	1.225	1.237	1.243	1.240	1.235	1.215	1.190	1.171
1.295	1.220	1.236	1.248	1.251	1.250	1.242	1.226	1.201	1.189
1.318	1.234	1.247	1.256	1.258	1.258	1.250	1.238	1.215	1.206
1.341	1.244	1.256	1.263	1.266	1.264	1.256	1.246	1.224	1.218
1.364	1.251	1.266	1.265	1.272	1.268	1.263	1.252	1.233	1.224
1.386	1.259	1.266	1.271	1.271	1.270	1.264	1.257	1.240	1.228
1.409	1.262	1.269	1.275	1.275	1.274	1.266	1.257	1.244	1.232
1.432	1.261	1.269	1.271	1.272	1.267	1.265	1.255	1.245	1.233
1.455	1.261	1.264	1.266	1.266	1.264	1.261	1.250	1.239	1.233
1.477	1.256	1.256	1.263	1.257	1.256	1.252	1.240	1.234	1.225
1.500	1.246	1.252	1.252	1.253	1.250	1.244	1.234	1.225	1.212
1.523	1.237	1.242	1.245	1.241	1.240	1.231	1.223	1.214	1.203
1.545	1.224	1.230	1.235	1.233	1.230	1.217	1.212	1.202	1.188

1.568	1.214	1.232	1.220	1.219	1.221	1.209	1.194	1.187	1.169
1.591	1.195	1.221	1.209	1.207	1.204	1.193	1.184	1.172	1.157
1.614	1.183	1.213	1.197	1.196	1.191	1.179	1.169	1.158	1.136
1.636	1.169	1.196	1.181	1.180	1.180	1.167	1.155	1.142	1.126
1.659	1.149	1.182	1.170	1.166	1.165	1.157	1.142	1.128	1.105
1.682	1.132	1.169	1.155	1.152	1.154	1.140	1.127	1.109	1.089
1.705	1.115	1.149	1.138	1.137	1.137	1.121	1.111	1.086	1.065
1.727	1.096	1.131	1.116	1.121	1.113	1.105	1.087	1.056	1.050
1.750	1.074	1.111	1.103	1.104	1.099	1.092	1.067	1.057	1.030
1.773	1.053	1.088	1.084	1.086	1.084	1.069	1.049	1.033	1.008
1.795	1.030	1.075	1.066	1.072	1.066	1.053	1.030	1.015	0.979
1.818	1.007	1.058	1.050	1.052	1.049	1.037	1.012	0.994	0.954
1.841	0.988	1.037	1.035	1.037	1.042	1.019	0.997	0.969	0.927
1.864	0.953	1.015	1.018	1.022	1.023	1.003	0.976	0.951	0.892
1.886	0.928	0.996	0.998	0.997	0.999	0.984	0.953	0.922	0.865
1.909	0.913	0.991	0.990	0.994	0.991	0.975	0.938	0.914	0.841
1.932	0.917	0.983	0.989	0.998	0.996	0.975	0.942	0.892	0.823
1.955	0.915	0.979	0.990	0.997	0.991	0.972	0.936	0.884	0.803
1.977	0.911	0.974	0.988	0.995	0.988	0.968	0.931	0.880	0.794
2.000	0.910	0.976	0.984	0.994	0.988	0.966	0.929	0.873	0.790
2.023	0.914	0.977	0.987	0.996	0.988	0.966	0.927	0.874	0.789
2.045	0.916	0.978	0.986	0.996	0.990	0.964	0.929	0.877	0.794
2.068	0.922	0.983	0.994	0.999	0.990	0.967	0.934	0.880	0.803
2.091	0.931	0.989	0.992	1.002	0.993	0.968	0.934	0.885	0.813
2.114	0.940	0.996	0.998	1.005	0.996	0.972	0.943	0.892	0.829
2.136	0.952	0.996	1.005	1.006	1.000	0.977	0.944	0.903	0.838
2.159	0.961	1.005	1.010	1.012	1.005	0.983	0.953	0.912	0.854
2.182	0.973	1.014	1.016	1.017	1.007	0.989	0.958	0.922	0.870
2.205	0.986	1.018	1.015	1.017	1.012	0.993	0.963	0.929	0.885
2.227	0.993	1.024	1.019	1.018	1.015	0.997	0.970	0.937	0.897
2.250	1.000	1.028	1.022	1.016	1.011	0.998	0.978	0.949	0.913
2.273	1.002	1.028	1.015	1.012	1.007	0.995	0.978	0.952	0.923
2.295	1.000	1.022	1.008	1.005	1.003	0.994	0.978	0.957	0.937
2.318	0.994	1.017	0.995	0.994	0.990	0.983	0.970	0.956	0.938
2.341	0.980	0.997	0.984	0.979	0.978	0.972	0.959	0.948	0.934
2.364	0.963	0.970	0.962	0.959	0.961	0.954	0.948	0.936	0.928
2.386	0.883	0.924	0.939	0.932	0.935	0.928	0.928	0.915	0.914
2.409	0.693	0.813	0.824	0.779	0.803	0.702	0.845	0.818	0.853

2.432	0.646	0.565	0.448	0.284	0.598	0.400	0.275	0.186	0.618
2.455	0.234	0.172	0.240	0.302	0.083	0.100	0.140	0.080	0.322
2.477	0.119	0.101	0.269	0.184	0.044	0.098	0.222	0.087	0.102

X/P	Y= 1.409P	Y= 1.432P	Y= 1.455P	Y= 1.477P	Y= 1.5P	Y= 1.523P	Y= 1.545P	Y= 1.545P	Y= 1.591P
0.000	0.911	1.016	1.067	1.100	1.104	1.092	1.065	1.026	0.961
0.023	0.909	1.025	1.072	1.098	1.104	1.093	1.069	1.026	0.969
0.045	0.924	1.029	1.079	1.104	1.109	1.105	1.073	1.039	0.978
0.068	0.936	1.043	1.088	1.113	1.115	1.105	1.079	1.043	0.984
0.091	0.969	1.054	1.099	1.121	1.123	1.115	1.091	1.028	0.998
0.114	0.985	1.070	1.106	1.131	1.128	1.120	1.093	1.032	1.011
0.136	1.009	1.086	1.118	1.137	1.136	1.130	1.099	1.049	1.027
0.159	1.038	1.100	1.129	1.145	1.149	1.133	1.114	1.063	1.043
0.182	1.063	1.114	1.141	1.158	1.157	1.144	1.125	1.075	1.060
0.205	1.082	1.128	1.152	1.160	1.142	1.155	1.129	1.083	1.067
0.227	1.097	1.144	1.163	1.174	1.159	1.165	1.147	1.091	1.089
0.250	1.118	1.153	1.169	1.183	1.160	1.173	1.156	1.110	1.108
0.273	1.133	1.164	1.183	1.193	1.174	1.189	1.169	1.113	1.125
0.295	1.148	1.178	1.190	1.201	1.181	1.192	1.176	1.127	1.145
0.318	1.159	1.194	1.205	1.213	1.195	1.204	1.193	1.147	1.152
0.341	1.183	1.202	1.213	1.221	1.197	1.214	1.206	1.171	1.172
0.364	1.192	1.218	1.223	1.229	1.213	1.224	1.217	1.170	1.185
0.386	1.204	1.221	1.231	1.236	1.222	1.229	1.220	1.189	1.199
0.409	1.220	1.229	1.239	1.240	1.226	1.237	1.225	1.203	1.205
0.432	1.225	1.236	1.234	1.241	1.231	1.236	1.229	1.207	1.209
0.455	1.226	1.236	1.237	1.243	1.232	1.233	1.226	1.206	1.207
0.477	1.231	1.236	1.237	1.242	1.236	1.233	1.225	1.206	1.205
0.500	1.229	1.229	1.231	1.235	1.233	1.228	1.220	1.206	1.198
0.523	1.223	1.223	1.231	1.227	1.226	1.218	1.214	1.198	1.186
0.545	1.221	1.216	1.225	1.217	1.219	1.208	1.203	1.188	1.176
0.568	1.209	1.206	1.218	1.209	1.208	1.201	1.190	1.176	1.164
0.591	1.194	1.194	1.204	1.199	1.195	1.183	1.178	1.162	1.148
0.614	1.190	1.182	1.197	1.188	1.185	1.177	1.169	1.148	1.134
0.636	1.169	1.169	1.183	1.177	1.175	1.164	1.154	1.138	1.119
0.659	1.166	1.154	1.175	1.159	1.160	1.149	1.144	1.121	1.107
0.682	1.146	1.139	1.157	1.151	1.144	1.142	1.127	1.108	1.092
0.705	1.121	1.120	1.140	1.129	1.128	1.125	1.111	1.093	1.069
0.727	1.104	1.101	1.130	1.122	1.117	1.109	1.096	1.078	1.053
0.750	1.088	1.079	1.117	1.103	1.104	1.095	1.083	1.063	1.036
0.773	1.067	1.065	1.098	1.089	1.088	1.084	1.067	1.050	1.016

0.795	1.037	1.039	1.084	1.075	1.076	1.069	1.047	1.032	0.995
0.818	0.996	1.020	1.047	1.060	1.064	1.052	1.040	1.012	0.973
0.841	0.978	0.998	1.042	1.048	1.053	1.043	1.031	1.000	0.958
0.864	0.943	0.986	1.031	1.037	1.046	1.037	1.020	0.985	0.940
0.886	0.915	0.973	1.014	1.033	1.037	1.033	1.012	0.978	0.926
0.909	0.892	0.962	1.007	1.031	1.041	1.031	1.010	0.966	0.922
0.932	0.878	0.958	1.002	1.035	1.041	1.036	1.012	0.963	0.914
0.955	0.867	0.961	0.997	1.039	1.046	1.042	1.018	0.964	0.911
0.977	0.869	0.970	0.998	1.044	1.051	1.049	1.022	0.962	0.914
1.000	0.879	0.977	1.009	1.055	1.063	1.055	1.031	0.967	0.923
1.023	0.894	0.991	1.015	1.064	1.070	1.060	1.035	0.980	0.930
1.045	0.917	1.009	1.031	1.079	1.084	1.072	1.046	0.982	0.940
1.068	0.940	1.026	1.046	1.092	1.090	1.082	1.050	0.996	0.952
1.091	0.968	1.044	1.067	1.101	1.098	1.090	1.061	1.005	0.971
1.114	0.990	1.062	1.078	1.115	1.111	1.098	1.074	1.016	0.979
1.136	1.023	1.080	1.095	1.124	1.120	1.111	1.083	1.028	0.999
1.159	1.049	1.094	1.107	1.135	1.130	1.116	1.094	1.045	1.017
1.182	1.075	1.117	1.126	1.146	1.141	1.129	1.099	1.056	1.041
1.205	1.098	1.133	1.142	1.157	1.153	1.141	1.115	1.078	1.052
1.227	1.117	1.146	1.152	1.167	1.158	1.146	1.130	1.085	1.067
1.250	1.136	1.162	1.165	1.180	1.173	1.163	1.137	1.102	1.084
1.273	1.153	1.175	1.174	1.186	1.181	1.170	1.155	1.121	1.102
1.295	1.168	1.186	1.186	1.197	1.192	1.179	1.164	1.130	1.121
1.318	1.178	1.198	1.197	1.205	1.203	1.195	1.175	1.145	1.135
1.341	1.193	1.203	1.206	1.212	1.205	1.201	1.186	1.160	1.150
1.364	1.204	1.214	1.215	1.218	1.215	1.211	1.195	1.169	1.162
1.386	1.211	1.223	1.222	1.224	1.220	1.214	1.197	1.180	1.175
1.409	1.214	1.223	1.231	1.227	1.224	1.211	1.202	1.186	1.174
1.432	1.216	1.223	1.229	1.223	1.222	1.207	1.203	1.190	1.181
1.455	1.214	1.221	1.228	1.221	1.221	1.205	1.205	1.190	1.181
1.477	1.212	1.216	1.222	1.216	1.210	1.201	1.195	1.184	1.173
1.500	1.205	1.209	1.218	1.211	1.206	1.193	1.186	1.179	1.159
1.523	1.196	1.201	1.210	1.200	1.196	1.189	1.175	1.168	1.150
1.545	1.184	1.191	1.204	1.189	1.180	1.173	1.166	1.158	1.133
1.568	1.176	1.183	1.188	1.177	1.173	1.164	1.149	1.143	1.126
1.591	1.163	1.169	1.176	1.166	1.163	1.152	1.136	1.126	1.101
1.614	1.150	1.155	1.173	1.153	1.149	1.137	1.122	1.111	1.090
1.636	1.135	1.147	1.165	1.145	1.139	1.123	1.110	1.091	1.071

1.659	1.125	1.131	1.145	1.132	1.125	1.112	1.093	1.078	1.051
1.682	1.107	1.117	1.133	1.121	1.111	1.101	1.085	1.061	1.034
1.705	1.090	1.102	1.127	1.108	1.101	1.085	1.076	1.050	1.020
1.727	1.072	1.084	1.106	1.096	1.089	1.075	1.054	1.036	1.002
1.750	1.047	1.069	1.090	1.081	1.077	1.063	1.041	1.027	0.987
1.773	1.022	1.046	1.077	1.067	1.064	1.049	1.027	1.004	0.974
1.795	0.998	1.026	1.061	1.051	1.050	1.035	1.016	0.992	0.951
1.818	0.973	1.006	1.038	1.036	1.040	1.022	0.999	0.976	0.924
1.841	0.953	0.987	1.025	1.024	1.025	1.005	0.984	0.957	0.909
1.864	0.915	0.962	1.008	1.009	1.008	0.989	0.966	0.932	0.878
1.886	0.887	0.938	0.993	0.990	0.992	0.976	0.951	0.917	0.855
1.909	0.872	0.933	0.988	0.985	0.986	0.970	0.938	0.911	0.838
1.932	0.864	0.927	0.973	0.980	0.983	0.965	0.935	0.894	0.824
1.955	0.858	0.919	0.971	0.973	0.974	0.959	0.929	0.891	0.810
1.977	0.848	0.920	0.965	0.975	0.973	0.962	0.920	0.878	0.795
2.000	0.851	0.919	0.966	0.971	0.967	0.954	0.911	0.873	0.794
2.023	0.853	0.921	0.968	0.971	0.965	0.950	0.910	0.864	0.787
2.045	0.862	0.925	0.970	0.973	0.965	0.947	0.907	0.863	0.785
2.068	0.874	0.932	0.973	0.973	0.966	0.949	0.909	0.866	0.791
2.091	0.885	0.940	0.976	0.978	0.970	0.944	0.910	0.869	0.793
2.114	0.901	0.950	0.978	0.985	0.972	0.949	0.915	0.866	0.807
2.136	0.913	0.958	0.990	0.987	0.977	0.946	0.921	0.875	0.821
2.159	0.929	0.969	0.994	0.992	0.984	0.956	0.923	0.882	0.829
2.182	0.945	0.978	1.002	1.001	0.983	0.959	0.932	0.894	0.850
2.205	0.957	0.986	1.006	1.002	0.989	0.968	0.942	0.901	0.862
2.227	0.975	0.995	1.014	1.008	0.996	0.973	0.951	0.912	0.879
2.250	0.984	1.001	1.019	1.010	1.000	0.984	0.953	0.925	0.892
2.273	0.991	1.005	1.019	1.009	1.005	0.982	0.963	0.924	0.902
2.295	0.992	1.003	1.008	1.004	1.004	0.985	0.965	0.940	0.897
2.318	0.994	0.993	1.001	0.995	0.999	0.984	0.962	0.941	0.912
2.341	0.984	0.983	0.988	0.981	0.990	0.973	0.952	0.935	0.916
2.364	0.972	0.970	0.972	0.963	0.967	0.956	0.943	0.929	0.914
2.386	0.943	0.933	0.939	0.929	0.941	0.926	0.882	0.874	0.877
2.409	0.797	0.608	0.486	0.724	0.738	0.660	0.807	0.777	0.665
2.432	0.258	0.179	0.226	0.379	0.211	0.316	0.299	0.232	0.254
2.455	0.136	0.113	0.158	0.324	0.061	0.121	0.050	0.058	0.230
2.477	0.111	0.213	0.109	0.089	0.026	0.118	0.005	0.007	0.031

X/P	Y=2.409P	Y=2.432P	Y=2.455P	Y=2.477P	Y=2.5P
0.000	0.689	0.777	0.826	0.842	0.821
0.023	0.706	0.785	0.838	0.849	0.835
0.045	0.729	0.809	0.849	0.868	0.842
0.068	0.747	0.830	0.869	0.877	0.852
0.091	0.771	0.852	0.880	0.895	0.868
0.114	0.806	0.867	0.898	0.908	0.872
0.136	0.839	0.893	0.914	0.915	0.890
0.159	0.874	0.916	0.937	0.930	0.897
0.182	0.887	0.935	0.947	0.936	0.895
0.205	0.884	0.960	0.952	0.948	0.911
0.227	0.906	0.973	0.973	0.946	0.912
0.250	0.929	0.991	0.981	0.952	0.916
0.273	0.965	1.002	0.988	0.960	0.877
0.295	0.980	1.009	0.990	0.957	0.882
0.318	0.996	1.017	0.994	0.963	0.892
0.341	1.008	1.018	0.997	0.961	0.888
0.364	1.007	1.021	0.994	0.961	0.886
0.386	1.023	1.026	0.990	0.958	0.894
0.409	1.023	1.025	0.988	0.958	0.892
0.432	1.024	1.022	0.990	0.954	0.897
0.455	1.028	1.017	0.987	0.946	0.889
0.477	1.024	1.010	0.979	0.944	0.890
0.500	1.018	1.007	0.976	0.938	0.891
0.523	1.017	1.004	0.972	0.935	0.889
0.545	1.017	0.995	0.963	0.927	0.881
0.568	1.010	0.992	0.960	0.923	0.880
0.591	1.004	0.986	0.954	0.916	0.874
0.614	1.001	0.973	0.948	0.912	0.880
0.636	0.990	0.964	0.939	0.903	0.869
0.659	0.982	0.951	0.929	0.899	0.866
0.682	0.969	0.945	0.921	0.894	0.858
0.705	0.944	0.924	0.912	0.888	0.847
0.727	0.928	0.915	0.903	0.876	0.851
0.750	0.897	0.896	0.891	0.869	0.849
0.773	0.885	0.882	0.881	0.860	0.841
0.795	0.853	0.861	0.871	0.855	0.833

0.818	0.835	0.843	0.855	0.848	0.839
0.841	0.800	0.825	0.846	0.838	0.827
0.864	0.784	0.814	0.837	0.835	0.822
0.886	0.754	0.800	0.838	0.833	0.816
0.909	0.732	0.794	0.826	0.834	0.812
0.932	0.717	0.789	0.819	0.835	0.810
0.955	0.700	0.791	0.812	0.833	0.811
0.977	0.696	0.790	0.816	0.847	0.809
1.000	0.697	0.794	0.822	0.855	0.808
1.023	0.701	0.802	0.824	0.859	0.817
1.045	0.726	0.822	0.841	0.866	0.818
1.068	0.733	0.836	0.841	0.876	0.823
1.091	0.760	0.850	0.858	0.882	0.830
1.114	0.782	0.868	0.867	0.891	0.838
1.136	0.815	0.885	0.881	0.898	0.843
1.159	0.839	0.904	0.891	0.912	0.847
1.182	0.862	0.916	0.903	0.913	0.854
1.205	0.889	0.931	0.917	0.916	0.861
1.227	0.908	0.943	0.921	0.916	0.863
1.250	0.927	0.955	0.927	0.921	0.868
1.273	0.942	0.959	0.935	0.921	0.871
1.295	0.952	0.961	0.937	0.922	0.875
1.318	0.961	0.971	0.939	0.916	0.872
1.341	0.973	0.966	0.941	0.921	0.868
1.364	0.973	0.973	0.941	0.911	0.874
1.386	0.979	0.964	0.938	0.904	0.869
1.409	0.983	0.963	0.935	0.901	0.864
1.432	0.980	0.958	0.935	0.898	0.865
1.455	0.972	0.955	0.930	0.893	0.852
1.477	0.979	0.949	0.925	0.882	0.854
1.500	0.975	0.948	0.913	0.876	0.840
1.523	0.967	0.936	0.909	0.874	0.833
1.545	0.959	0.931	0.911	0.859	0.830
1.568	0.955	0.923	0.893	0.851	0.817
1.591	0.942	0.913	0.889	0.843	0.817
1.614	0.935	0.894	0.878	0.827	0.814
1.636	0.929	0.874	0.884	0.822	0.798
1.659	0.892	0.862	0.875	0.809	0.782

1.682	0.862	0.848	0.851	0.821	0.778
1.705	0.858	0.826	0.840	0.801	0.779
1.727	0.831	0.803	0.820	0.795	0.751
1.750	0.796	0.782	0.803	0.774	0.744
1.773	0.776	0.759	0.789	0.765	0.726
1.795	0.746	0.735	0.769	0.744	0.734
1.818	0.709	0.712	0.744	0.734	0.717
1.841	0.668	0.690	0.720	0.728	0.709
1.864	0.642	0.669	0.688	0.699	0.695
1.886	0.628	0.655	0.698	0.705	0.681
1.909	0.612	0.642	0.697	0.703	0.681
1.932	0.613	0.643	0.697	0.701	0.681
1.955	0.601	0.649	0.691	0.697	0.680
1.977	0.606	0.659	0.694	0.692	0.678
2.000	0.600	0.663	0.703	0.703	0.680
2.023	0.614	0.669	0.699	0.705	0.680
2.045	0.620	0.675	0.705	0.708	0.680
2.068	0.638	0.692	0.712	0.708	0.685
2.091	0.650	0.702	0.722	0.708	0.685
2.114	0.674	0.715	0.730	0.710	0.685
2.136	0.690	0.724	0.731	0.710	0.677
2.159	0.710	0.733	0.734	0.719	0.673
2.182	0.722	0.741	0.739	0.704	0.660
2.205	0.736	0.745	0.734	0.701	0.658
2.227	0.746	0.753	0.735	0.704	0.653
2.250	0.759	0.759	0.730	0.701	0.641
2.273	0.754	0.750	0.730	0.686	0.635
2.295	0.756	0.738	0.718	0.671	0.602
2.318	0.700	0.721	0.660	0.651	0.548
2.341	0.690	0.700	0.428	0.615	0.421
2.364	0.529	0.595	0.257	0.537	0.180
2.386	0.255	0.265	0.096	0.211	0.083
2.409	0.164	0.085	0.101	0.047	0.032
2.432	0.161	0.085	0.077	0.041	0.031
2.455	0.071	0.036	0.052	0.049	0.028
2.477	0.004	0.000	0.005	0.007	0.010

b)  $W_{rms}/W_{bulk}$ 

X/P	Y= 0.409P	Y= 0.432P	Y= 0.455P	Y= 0.477P	Y= 0.5P	Y= 0.523P	Y= 0.545P	Y= 0.568P	Y= 0.591P
0.000E+00	1.088E-01	8.692E-02	7.546E-02	6.688E-02	6.241E-02	6.691E-02	7.392E-02	8.117E-02	9.335E-02
2.274E-02	1.123E-01	8.896E-02	7.523E-02	6.747E-02	6.432E-02	6.969E-02	7.577E-02	8.248E-02	9.368E-02
4.544E-02	1.136E-01	8.992E-02	7.737E-02	7.065E-02	6.595E-02	7.113E-02	7.735E-02	8.582E-02	9.603E-02
6.818E-02	1.125E-01	9.160E-02	7.900E-02	7.188E-02	6.875E-02	7.270E-02	7.789E-02	8.621E-02	9.714E-02
9.091E-02	1.113E-01	9.110E-02	7.970E-02	7.220E-02	6.936E-02	7.288E-02	7.852E-02	8.773E-02	9.834E-02
1.137E-01	1.091E-01	9.026E-02	7.977E-02	7.317E-02	7.108E-02	7.346E-02	7.810E-02	8.796E-02	9.880E-02
1.364E-01	1.057E-01	8.938E-02	7.925E-02	7.333E-02	7.206E-02	7.408E-02	8.027E-02	8.755E-02	9.764E-02
1.591E-01	1.007E-01	8.835E-02	7.815E-02	7.430E-02	7.332E-02	7.548E-02	8.003E-02	8.760E-02	9.805E-02
1.818E-01	9.771E-02	8.571E-02	7.643E-02	7.225E-02	7.247E-02	7.508E-02	8.083E-02	8.773E-02	9.672E-02
2.046E-01	9.580E-02	8.266E-02	7.653E-02	7.360E-02	7.365E-02	7.438E-02	7.863E-02	8.739E-02	9.510E-02
2.273E-01	9.295E-02	8.217E-02	7.473E-02	7.244E-02	7.130E-02	7.310E-02	7.801E-02	8.674E-02	9.504E-02
2.500E-01	8.951E-02	7.974E-02	7.435E-02	7.175E-02	7.288E-02	7.260E-02	7.812E-02	8.542E-02	9.311E-02
2.727E-01	8.683E-02	7.804E-02	7.216E-02	7.114E-02	7.203E-02	7.095E-02	7.565E-02	8.427E-02	9.012E-02
2.954E-01	8.349E-02	7.629E-02	7.119E-02	6.890E-02	7.078E-02	6.893E-02	7.448E-02	8.159E-02	8.919E-02
3.182E-01	8.025E-02	7.342E-02	6.932E-02	6.865E-02	6.813E-02	6.703E-02	7.252E-02	8.025E-02	8.396E-02
3.409E-01	7.685E-02	7.055E-02	6.630E-02	6.510E-02	6.548E-02	6.422E-02	6.858E-02	7.704E-02	7.842E-02
3.637E-01	7.216E-02	6.711E-02	6.390E-02	6.210E-02	6.343E-02	6.174E-02	6.494E-02	7.428E-02	7.318E-02
3.864E-01	6.947E-02	6.521E-02	6.136E-02	5.984E-02	6.031E-02	5.929E-02	6.304E-02	6.813E-02	6.892E-02
4.091E-01	6.598E-02	6.108E-02	5.905E-02	5.656E-02	5.884E-02	5.973E-02	5.991E-02	6.763E-02	6.567E-02
4.318E-01	6.250E-02	6.075E-02	5.689E-02	5.678E-02	5.805E-02	5.588E-02	5.811E-02	6.343E-02	6.471E-02
4.546E-01	6.073E-02	5.734E-02	5.551E-02	5.544E-02	5.582E-02	5.671E-02	5.964E-02	6.207E-02	6.254E-02
4.773E-01	6.102E-02	5.710E-02	5.564E-02	5.528E-02	5.552E-02	5.701E-02	5.865E-02	6.217E-02	6.615E-02
5.000E-01	6.330E-02	6.147E-02	5.748E-02	5.546E-02	5.659E-02	5.891E-02	6.053E-02	6.354E-02	6.684E-02
5.227E-01	6.487E-02	6.421E-02	5.798E-02	5.811E-02	5.928E-02	6.063E-02	6.326E-02	6.685E-02	6.859E-02
5.454E-01	6.662E-02	6.540E-02	6.248E-02	5.997E-02	6.073E-02	6.269E-02	6.469E-02	6.890E-02	7.190E-02
5.682E-01	6.956E-02	6.696E-02	6.340E-02	6.123E-02	6.296E-02	6.506E-02	6.698E-02	7.260E-02	7.476E-02
5.909E-01	7.049E-02	6.763E-02	6.469E-02	6.329E-02	6.331E-02	6.532E-02	6.892E-02	7.473E-02	7.666E-02
6.137E-01	7.351E-02	6.945E-02	6.631E-02	6.335E-02	6.566E-02	6.672E-02	7.013E-02	7.534E-02	7.671E-02
6.364E-01	7.454E-02	7.034E-02	6.676E-02	6.580E-02	6.578E-02	6.835E-02	7.039E-02	7.647E-02	7.847E-02
6.591E-01	7.738E-02	7.193E-02	6.693E-02	6.557E-02	6.678E-02	6.858E-02	7.116E-02	7.732E-02	7.792E-02
6.818E-01	7.689E-02	7.292E-02	6.861E-02	6.682E-02	6.638E-02	6.871E-02	7.267E-02	7.744E-02	8.121E-02
7.046E-01	8.017E-02	7.444E-02	6.911E-02	6.578E-02	6.578E-02	6.940E-02	7.328E-02	7.814E-02	8.231E-02
7.273E-01	8.124E-02	7.420E-02	7.042E-02	6.727E-02	6.650E-02	6.808E-02	7.276E-02	7.813E-02	8.254E-02
7.500E-01	8.243E-02	7.504E-02	7.022E-02	6.669E-02	6.589E-02	6.791E-02	7.155E-02	7.902E-02	8.353E-02
7.727E-01	8.452E-02	7.727E-02	7.088E-02	6.638E-02	6.578E-02	6.766E-02	7.170E-02	7.855E-02	8.420E-02

7.954E-01	8.660E-02	7.789E-02	7.034E-02	6.537E-02	6.461E-02	6.450E-02	7.267E-02	8.104E-02	8.571E-02
8.182E-01	8.790E-02	7.854E-02	6.930E-02	6.477E-02	6.395E-02	6.422E-02	7.019E-02	7.794E-02	8.652E-02
8.409E-01	8.786E-02	7.816E-02	6.824E-02	6.385E-02	6.048E-02	6.283E-02	6.780E-02	7.796E-02	8.592E-02
8.637E-01	8.861E-02	7.580E-02	6.817E-02	6.396E-02	5.953E-02	6.122E-02	6.814E-02	7.838E-02	8.639E-02
8.864E-01	8.759E-02	7.742E-02	6.742E-02	6.172E-02	5.838E-02	6.088E-02	6.756E-02	7.682E-02	8.560E-02
9.091E-01	8.960E-02	7.784E-02	6.772E-02	6.087E-02	5.773E-02	6.121E-02	6.804E-02	7.642E-02	8.732E-02
9.318E-01	8.993E-02	7.775E-02	6.885E-02	6.190E-02	5.964E-02	6.237E-02	6.776E-02	7.718E-02	8.765E-02
9.546E-01	9.151E-02	8.069E-02	7.134E-02	6.200E-02	6.007E-02	6.280E-02	6.918E-02	7.773E-02	8.963E-02
9.773E-01	9.352E-02	8.230E-02	7.143E-02	6.248E-02	6.128E-02	6.592E-02	7.114E-02	7.931E-02	9.135E-02
1.000E+00	9.530E-02	8.367E-02	7.313E-02	6.459E-02	6.311E-02	6.630E-02	7.453E-02	8.253E-02	9.364E-02
1.023E+00	9.767E-02	8.347E-02	7.432E-02	6.468E-02	6.370E-02	6.899E-02	7.558E-02	8.363E-02	9.465E-02
1.045E+00	9.844E-02	8.578E-02	7.457E-02	6.656E-02	6.509E-02	6.995E-02	7.720E-02	8.405E-02	9.643E-02
1.068E+00	9.898E-02	8.428E-02	7.478E-02	6.729E-02	6.635E-02	6.970E-02	7.904E-02	8.543E-02	9.764E-02
1.091E+00	9.978E-02	8.616E-02	7.431E-02	6.722E-02	6.798E-02	7.133E-02	7.983E-02	8.676E-02	9.931E-02
1.114E+00	9.663E-02	8.506E-02	7.525E-02	6.887E-02	6.812E-02	7.157E-02	7.957E-02	8.673E-02	9.811E-02
1.136E+00	9.645E-02	8.455E-02	7.462E-02	6.947E-02	6.815E-02	7.296E-02	8.015E-02	8.603E-02	9.806E-02
1.159E+00	9.483E-02	8.222E-02	7.568E-02	6.946E-02	6.840E-02	7.294E-02	8.039E-02	8.824E-02	9.683E-02
1.182E+00	9.284E-02	8.091E-02	7.476E-02	6.981E-02	6.869E-02	7.238E-02	7.908E-02	8.642E-02	9.479E-02
1.205E+00	9.066E-02	7.974E-02	7.219E-02	6.733E-02	6.893E-02	7.231E-02	7.787E-02	8.671E-02	9.314E-02
1.227E+00	8.670E-02	7.778E-02	7.131E-02	6.649E-02	6.820E-02	7.153E-02	7.675E-02	8.680E-02	9.033E-02
1.250E+00	8.334E-02	7.466E-02	6.859E-02	6.620E-02	6.624E-02	7.056E-02	7.550E-02	8.299E-02	8.942E-02
1.273E+00	8.049E-02	7.149E-02	6.658E-02	6.429E-02	6.500E-02	6.857E-02	7.317E-02	8.212E-02	8.537E-02
1.295E+00	7.618E-02	6.896E-02	6.531E-02	6.354E-02	6.406E-02	6.668E-02	7.066E-02	7.762E-02	8.241E-02
1.318E+00	7.197E-02	6.678E-02	6.209E-02	6.052E-02	6.035E-02	6.385E-02	6.837E-02	7.519E-02	7.777E-02
1.341E+00	6.821E-02	6.332E-02	6.016E-02	5.808E-02	5.907E-02	6.204E-02	6.539E-02	7.176E-02	7.392E-02
1.364E+00	6.417E-02	5.976E-02	5.800E-02	5.775E-02	5.789E-02	5.896E-02	6.393E-02	6.990E-02	7.160E-02
1.386E+00	6.217E-02	6.041E-02	5.665E-02	5.526E-02	5.590E-02	5.859E-02	6.062E-02	6.615E-02	6.881E-02
1.409E+00	5.991E-02	5.783E-02	5.552E-02	5.516E-02	5.713E-02	5.888E-02	6.171E-02	6.435E-02	6.818E-02
1.432E+00	5.975E-02	5.855E-02	5.654E-02	5.578E-02	5.777E-02	5.951E-02	6.143E-02	6.482E-02	6.693E-02
1.455E+00	6.162E-02	5.879E-02	5.747E-02	5.821E-02	5.901E-02	6.150E-02	6.392E-02	6.633E-02	6.751E-02
1.477E+00	6.178E-02	6.143E-02	5.974E-02	6.156E-02	6.134E-02	6.360E-02	6.558E-02	6.873E-02	7.098E-02
1.500E+00	6.477E-02	6.281E-02	6.127E-02	6.269E-02	6.274E-02	6.653E-02	6.897E-02	7.164E-02	7.342E-02
1.523E+00	6.761E-02	6.669E-02	6.385E-02	6.491E-02	6.498E-02	7.086E-02	7.117E-02	7.410E-02	7.630E-02
1.545E+00	6.987E-02	6.906E-02	6.542E-02	6.663E-02	6.737E-02	7.240E-02	7.249E-02	7.680E-02	7.919E-02
1.568E+00	7.186E-02	6.893E-02	6.928E-02	6.805E-02	7.058E-02	7.208E-02	7.601E-02	7.933E-02	8.261E-02
1.591E+00	7.384E-02	7.106E-02	7.094E-02	7.081E-02	7.204E-02	7.514E-02	7.732E-02	8.199E-02	8.470E-02
1.614E+00	7.679E-02	7.170E-02	7.203E-02	7.262E-02	7.368E-02	7.562E-02	7.913E-02	8.294E-02	8.567E-02
1.636E+00	7.906E-02	7.363E-02	7.453E-02	7.269E-02	7.442E-02	7.623E-02	8.066E-02	8.321E-02	8.681E-02

1.659E+00	8.022E-02	7.603E-02	7.364E-02	7.474E-02	7.484E-02	7.824E-02	8.145E-02	8.451E-02	8.948E-02
1.682E+00	8.122E-02	7.513E-02	7.651E-02	7.554E-02	7.577E-02	7.981E-02	8.300E-02	8.688E-02	9.039E-02
1.705E+00	8.336E-02	7.845E-02	7.639E-02	7.509E-02	7.779E-02	7.962E-02	8.433E-02	8.770E-02	9.319E-02
1.727E+00	8.572E-02	7.906E-02	7.819E-02	7.689E-02	7.741E-02	8.001E-02	8.552E-02	8.950E-02	9.434E-02
1.750E+00	8.408E-02	7.936E-02	7.269E-02	7.581E-02	7.993E-02	8.339E-02	8.996E-02	9.728E-02	9.622E-02
1.773E+00	8.459E-02	7.956E-02	7.262E-02	7.588E-02	7.848E-02	8.308E-02	9.092E-02	9.899E-02	9.670E-02
1.795E+00	8.553E-02	7.918E-02	7.164E-02	7.361E-02	7.659E-02	8.383E-02	9.028E-02	9.889E-02	9.830E-02
1.818E+00	8.386E-02	7.731E-02	7.197E-02	7.394E-02	7.694E-02	8.305E-02	8.971E-02	9.895E-02	9.839E-02
1.841E+00	8.318E-02	7.502E-02	7.079E-02	6.963E-02	7.504E-02	8.051E-02	8.762E-02	9.896E-02	9.939E-02
1.864E+00	8.004E-02	7.105E-02	6.743E-02	6.657E-02	7.147E-02	8.014E-02	8.660E-02	9.873E-02	1.213E-01
1.886E+00	8.058E-02	6.831E-02	6.505E-02	6.501E-02	7.010E-02	7.753E-02	8.768E-02	9.825E-02	1.326E-01
1.909E+00	7.673E-02	6.720E-02	6.238E-02	6.343E-02	6.718E-02	7.475E-02	8.458E-02	9.687E-02	1.347E-01
1.932E+00	7.525E-02	6.549E-02	6.148E-02	6.060E-02	6.644E-02	7.435E-02	8.429E-02	9.458E-02	1.292E-01
1.955E+00	7.347E-02	6.380E-02	5.817E-02	6.119E-02	6.466E-02	7.269E-02	8.322E-02	9.138E-02	9.984E-02
1.977E+00	7.253E-02	6.234E-02	5.908E-02	5.798E-02	6.424E-02	7.235E-02	8.162E-02	9.109E-02	9.880E-02
2.000E+00	7.179E-02	6.195E-02	5.600E-02	5.829E-02	6.484E-02	7.296E-02	8.018E-02	9.001E-02	9.927E-02
2.023E+00	7.715E-02	6.650E-02	5.947E-02	5.814E-02	6.048E-02	6.895E-02	7.666E-02	8.481E-02	9.896E-02
2.045E+00	7.986E-02	6.614E-02	5.983E-02	5.742E-02	6.143E-02	6.838E-02	7.675E-02	8.536E-02	9.869E-02
2.068E+00	8.610E-02	6.555E-02	5.902E-02	5.906E-02	6.106E-02	6.824E-02	7.695E-02	8.621E-02	9.869E-02
2.091E+00	7.965E-02	6.459E-02	6.079E-02	5.945E-02	6.168E-02	6.993E-02	7.713E-02	8.513E-02	9.691E-02
2.114E+00	7.827E-02	6.553E-02	6.039E-02	5.790E-02	6.216E-02	6.984E-02	7.559E-02	8.622E-02	9.567E-02
2.136E+00	7.580E-02	6.292E-02	5.908E-02	5.672E-02	6.084E-02	6.764E-02	7.576E-02	8.452E-02	9.295E-02
2.159E+00	7.330E-02	6.246E-02	5.847E-02	5.776E-02	5.911E-02	6.885E-02	7.288E-02	8.156E-02	9.142E-02
2.182E+00	6.969E-02	6.115E-02	5.605E-02	5.445E-02	5.852E-02	6.478E-02	7.190E-02	7.971E-02	8.860E-02
2.205E+00	6.598E-02	5.873E-02	5.501E-02	5.385E-02	5.835E-02	6.226E-02	6.960E-02	7.777E-02	8.596E-02
2.227E+00	6.480E-02	6.057E-02	5.846E-02	5.907E-02	5.756E-02	6.396E-02	6.973E-02	7.772E-02	8.594E-02
2.250E+00	6.638E-02	5.962E-02	5.823E-02	5.822E-02	5.703E-02	6.118E-02	6.556E-02	7.203E-02	8.010E-02
2.273E+00	7.047E-02	6.990E-02	6.510E-02	6.407E-02	5.910E-02	6.512E-02	6.621E-02	7.088E-02	7.556E-02
2.295E+00	7.600E-02	8.425E-02	7.232E-02	7.201E-02	6.385E-02	7.006E-02	6.641E-02	7.184E-02	7.274E-02
2.318E+00	9.222E-02	9.971E-02	8.704E-02	9.111E-02	7.529E-02	7.454E-02	7.138E-02	7.365E-02	7.539E-02
2.341E+00	9.391E-02	9.272E-02	8.980E-02	9.107E-02	8.042E-02	7.592E-02	7.486E-02	7.511E-02	7.397E-02
2.364E+00	1.015E-01	1.066E-01	9.232E-02	9.848E-02	8.032E-02	8.350E-02	7.635E-02	8.313E-02	7.868E-02
2.386E+00	2.578E-01	2.193E-01	1.270E-01	1.420E-01	1.079E-01	1.341E-01	1.105E-01	1.237E-01	1.037E-01
2.409E+00	4.527E-01	4.023E-01	3.717E-01	4.177E-01	3.686E-01	4.430E-01	3.262E-01	3.604E-01	2.978E-01
2.432E+00	5.674E-01	5.729E-01	5.507E-01	4.835E-01	5.582E-01	5.275E-01	4.742E-01	4.044E-01	5.520E-01
2.455E+00	4.420E-01	3.829E-01	4.574E-01	4.907E-01	2.728E-01	2.962E-01	3.577E-01	2.671E-01	5.065E-01
2.477E+00	2.997E-01	2.749E-01	4.309E-01	3.658E-01	1.908E-01	2.827E-01	4.109E-01	2.612E-01	2.863E-01

X/P	Y= 1.409P	Y= 1.432P	Y= 1.455P	Y= 1.477P	Y= 1.5P	Y= 1.523P	Y= 1.545P	Y= 1.545P	Y= 1.591P
0.000E+00	9.935E-02	8.259E-02	7.077E-02	6.158E-02	5.904E-02	6.102E-02	7.073E-02	7.994E-02	8.894E-02
2.274E-02	9.769E-02	8.297E-02	7.231E-02	6.273E-02	5.911E-02	6.315E-02	7.070E-02	7.976E-02	9.149E-02
4.544E-02	9.910E-02	8.295E-02	7.097E-02	6.277E-02	6.034E-02	6.368E-02	7.258E-02	8.192E-02	9.253E-02
6.818E-02	9.951E-02	8.426E-02	7.225E-02	6.450E-02	6.152E-02	6.637E-02	7.393E-02	8.308E-02	9.160E-02
9.091E-02	9.934E-02	8.307E-02	7.237E-02	6.524E-02	6.281E-02	6.825E-02	7.503E-02	8.147E-02	9.241E-02
1.137E-01	9.803E-02	8.236E-02	7.150E-02	6.466E-02	6.405E-02	6.834E-02	7.721E-02	8.240E-02	9.263E-02
1.364E-01	9.630E-02	8.254E-02	7.202E-02	6.624E-02	6.805E-02	7.080E-02	7.681E-02	8.571E-02	9.399E-02
1.591E-01	9.477E-02	7.945E-02	7.223E-02	6.753E-02	6.716E-02	7.078E-02	7.745E-02	8.491E-02	9.359E-02
1.818E-01	9.074E-02	7.857E-02	7.149E-02	6.597E-02	6.673E-02	7.204E-02	7.682E-02	8.545E-02	9.169E-02
2.046E-01	8.864E-02	7.784E-02	7.003E-02	6.736E-02	6.849E-02	7.302E-02	7.743E-02	8.562E-02	9.126E-02
2.273E-01	8.723E-02	7.772E-02	7.170E-02	6.700E-02	6.904E-02	7.133E-02	7.808E-02	8.373E-02	9.099E-02
2.500E-01	8.075E-02	7.676E-02	6.977E-02	6.635E-02	6.898E-02	7.044E-02	7.710E-02	8.344E-02	8.801E-02
2.727E-01	7.946E-02	7.406E-02	6.781E-02	6.549E-02	6.827E-02	6.896E-02	7.527E-02	8.249E-02	8.574E-02
2.954E-01	7.808E-02	7.235E-02	6.693E-02	6.454E-02	6.759E-02	6.686E-02	7.356E-02	8.191E-02	8.129E-02
3.182E-01	7.599E-02	7.148E-02	6.665E-02	6.318E-02	6.608E-02	6.506E-02	7.047E-02	7.988E-02	8.030E-02
3.409E-01	7.276E-02	6.701E-02	6.363E-02	6.227E-02	6.492E-02	6.306E-02	6.859E-02	7.504E-02	7.557E-02
3.637E-01	6.984E-02	6.411E-02	6.239E-02	5.988E-02	6.215E-02	6.195E-02	6.381E-02	7.418E-02	7.079E-02
3.864E-01	6.842E-02	6.365E-02	5.964E-02	5.701E-02	6.141E-02	5.940E-02	6.139E-02	6.984E-02	6.776E-02
4.091E-01	6.424E-02	6.150E-02	5.654E-02	5.699E-02	5.922E-02	5.687E-02	6.014E-02	6.561E-02	6.540E-02
4.318E-01	6.121E-02	5.940E-02	5.628E-02	5.653E-02	5.717E-02	5.658E-02	5.994E-02	6.431E-02	6.533E-02
4.546E-01	6.010E-02	5.825E-02	5.717E-02	5.601E-02	5.738E-02	5.881E-02	6.113E-02	6.443E-02	6.499E-02
4.773E-01	5.778E-02	5.890E-02	5.698E-02	5.803E-02	5.758E-02	6.019E-02	6.123E-02	6.313E-02	6.680E-02
5.000E-01	6.076E-02	6.133E-02	5.807E-02	5.980E-02	6.104E-02	6.287E-02	6.679E-02	6.526E-02	6.768E-02
5.227E-01	6.196E-02	6.300E-02	6.034E-02	6.392E-02	6.504E-02	6.536E-02	6.772E-02	6.821E-02	7.354E-02
5.454E-01	6.376E-02	6.606E-02	6.258E-02	6.626E-02	6.655E-02	6.786E-02	6.901E-02	7.032E-02	7.706E-02
5.682E-01	6.648E-02	6.822E-02	6.635E-02	6.888E-02	6.985E-02	7.143E-02	7.388E-02	7.483E-02	7.950E-02
5.909E-01	7.006E-02	7.106E-02	6.760E-02	7.096E-02	7.120E-02	7.478E-02	7.578E-02	7.784E-02	8.107E-02
6.137E-01	7.295E-02	7.525E-02	7.107E-02	7.429E-02	7.341E-02	7.551E-02	7.657E-02	7.972E-02	8.363E-02
6.364E-01	7.753E-02	7.673E-02	7.291E-02	7.444E-02	7.508E-02	7.860E-02	7.903E-02	8.129E-02	8.466E-02
6.591E-01	7.623E-02	7.897E-02	7.458E-02	7.672E-02	7.619E-02	7.902E-02	8.027E-02	8.319E-02	8.489E-02
6.818E-01	8.095E-02	8.067E-02	7.604E-02	7.999E-02	7.959E-02	8.011E-02	8.226E-02	8.547E-02	9.023E-02
7.046E-01	8.413E-02	8.354E-02	7.764E-02	7.991E-02	8.037E-02	8.153E-02	8.302E-02	8.530E-02	9.171E-02
7.273E-01	8.933E-02	8.586E-02	8.190E-02	8.066E-02	8.118E-02	8.084E-02	8.321E-02	8.785E-02	9.162E-02
7.500E-01	9.051E-02	8.628E-02	8.186E-02	8.035E-02	8.001E-02	8.153E-02	8.219E-02	8.725E-02	9.102E-02
7.727E-01	9.398E-02	8.767E-02	8.309E-02	8.016E-02	7.840E-02	8.056E-02	8.282E-02	8.886E-02	9.229E-02
7.954E-01	9.691E-02	8.726E-02	8.252E-02	7.985E-02	7.793E-02	7.859E-02	8.054E-02	8.721E-02	9.221E-02

8.182E-01	9.887E-02	8.646E-02	8.021E-02	7.448E-02	7.459E-02	7.475E-02	8.027E-02	8.848E-02	9.199E-02
8.409E-01	1.029E-01	8.431E-02	8.023E-02	7.352E-02	7.131E-02	7.272E-02	7.721E-02	8.536E-02	9.098E-02
8.637E-01	1.034E-01	8.445E-02	8.029E-02	7.090E-02	6.831E-02	7.008E-02	7.444E-02	8.425E-02	8.839E-02
8.864E-01	1.006E-01	8.055E-02	7.737E-02	6.779E-02	6.617E-02	6.839E-02	7.275E-02	8.416E-02	8.657E-02
9.091E-01	9.404E-02	8.097E-02	7.654E-02	6.781E-02	6.587E-02	6.694E-02	7.207E-02	8.012E-02	8.670E-02
9.318E-01	9.446E-02	8.292E-02	7.475E-02	6.928E-02	6.761E-02	7.037E-02	7.179E-02	8.077E-02	8.851E-02
9.546E-01	9.696E-02	8.445E-02	7.579E-02	7.052E-02	6.679E-02	7.022E-02	7.485E-02	8.240E-02	9.072E-02
9.773E-01	1.000E-01	8.710E-02	7.630E-02	7.278E-02	6.882E-02	7.294E-02	7.687E-02	8.125E-02	9.140E-02
1.000E+00	1.022E-01	8.811E-02	7.860E-02	7.335E-02	7.110E-02	7.436E-02	7.851E-02	8.448E-02	9.413E-02
1.023E+00	1.051E-01	9.063E-02	7.972E-02	7.479E-02	7.351E-02	7.799E-02	7.921E-02	8.726E-02	9.749E-02
1.045E+00	1.075E-01	9.076E-02	8.186E-02	7.507E-02	7.583E-02	7.791E-02	8.284E-02	8.840E-02	9.781E-02
1.068E+00	1.091E-01	9.057E-02	8.133E-02	7.587E-02	7.515E-02	7.979E-02	8.391E-02	8.832E-02	9.904E-02
1.091E+00	1.077E-01	8.969E-02	8.206E-02	7.538E-02	7.544E-02	7.930E-02	8.470E-02	9.126E-02	9.984E-02
1.114E+00	1.055E-01	8.990E-02	8.058E-02	7.573E-02	7.656E-02	8.013E-02	8.563E-02	9.045E-02	1.008E-01
1.136E+00	1.041E-01	8.767E-02	8.105E-02	7.532E-02	7.453E-02	7.979E-02	8.535E-02	9.130E-02	9.875E-02
1.159E+00	1.000E-01	8.531E-02	7.979E-02	7.288E-02	7.529E-02	8.078E-02	8.555E-02	9.206E-02	9.941E-02
1.182E+00	9.526E-02	8.340E-02	7.601E-02	7.334E-02	7.511E-02	7.848E-02	8.588E-02	9.132E-02	9.807E-02
1.205E+00	9.147E-02	7.961E-02	7.575E-02	7.192E-02	7.474E-02	7.723E-02	8.461E-02	9.036E-02	9.577E-02
1.227E+00	8.824E-02	7.926E-02	7.546E-02	7.195E-02	7.275E-02	7.886E-02	8.253E-02	9.011E-02	9.517E-02
1.250E+00	8.431E-02	7.500E-02	7.485E-02	7.001E-02	7.339E-02	7.556E-02	8.262E-02	8.835E-02	9.417E-02
1.273E+00	7.942E-02	7.352E-02	7.172E-02	6.873E-02	7.120E-02	7.541E-02	7.769E-02	8.565E-02	8.938E-02
1.295E+00	7.605E-02	7.136E-02	6.976E-02	6.679E-02	6.871E-02	7.440E-02	7.715E-02	8.436E-02	8.651E-02
1.318E+00	7.261E-02	6.848E-02	6.711E-02	6.440E-02	6.744E-02	7.080E-02	7.480E-02	8.044E-02	8.423E-02
1.341E+00	6.824E-02	6.482E-02	6.485E-02	6.211E-02	6.413E-02	6.922E-02	7.049E-02	7.706E-02	7.823E-02
1.364E+00	6.430E-02	6.026E-02	6.311E-02	6.000E-02	6.114E-02	6.557E-02	6.769E-02	7.456E-02	7.478E-02
1.386E+00	6.052E-02	5.856E-02	6.080E-02	5.757E-02	5.851E-02	6.342E-02	6.471E-02	6.990E-02	7.087E-02
1.409E+00	5.893E-02	5.688E-02	5.764E-02	5.626E-02	5.775E-02	6.245E-02	6.401E-02	6.788E-02	6.832E-02
1.432E+00	5.809E-02	5.791E-02	5.721E-02	5.700E-02	5.920E-02	6.151E-02	6.173E-02	6.527E-02	6.604E-02
1.455E+00	5.688E-02	5.775E-02	5.606E-02	5.748E-02	5.724E-02	6.104E-02	6.254E-02	6.511E-02	6.662E-02
1.477E+00	5.878E-02	5.832E-02	5.665E-02	5.853E-02	6.008E-02	6.175E-02	6.419E-02	6.689E-02	6.784E-02
1.500E+00	5.991E-02	5.933E-02	5.824E-02	6.067E-02	6.203E-02	6.411E-02	6.747E-02	6.994E-02	7.210E-02
1.523E+00	6.128E-02	6.178E-02	5.989E-02	6.254E-02	6.521E-02	6.660E-02	7.093E-02	7.123E-02	7.556E-02
1.545E+00	6.473E-02	6.392E-02	6.240E-02	6.504E-02	6.834E-02	6.947E-02	7.235E-02	7.601E-02	7.861E-02
1.568E+00	6.650E-02	6.445E-02	6.405E-02	6.657E-02	6.805E-02	7.133E-02	7.463E-02	7.827E-02	8.207E-02
1.591E+00	6.764E-02	6.634E-02	6.688E-02	6.772E-02	7.094E-02	7.307E-02	7.806E-02	8.170E-02	8.399E-02
1.614E+00	6.981E-02	6.834E-02	6.614E-02	6.972E-02	7.143E-02	7.664E-02	7.879E-02	8.312E-02	8.480E-02
1.636E+00	7.095E-02	6.909E-02	6.773E-02	6.865E-02	7.154E-02	7.652E-02	8.062E-02	8.586E-02	8.769E-02
1.659E+00	7.236E-02	7.030E-02	6.886E-02	7.050E-02	7.281E-02	7.581E-02	8.062E-02	8.375E-02	8.843E-02

1.682E+00	7.606E-02	7.078E-02	6.992E-02	7.125E-02	7.506E-02	7.638E-02	8.106E-02	8.590E-02	9.011E-02
1.705E+00	7.813E-02	7.330E-02	6.945E-02	7.056E-02	7.445E-02	7.770E-02	8.208E-02	8.813E-02	9.072E-02
1.727E+00	8.101E-02	7.564E-02	7.166E-02	7.058E-02	7.326E-02	7.713E-02	8.132E-02	8.796E-02	8.975E-02
1.750E+00	8.295E-02	7.426E-02	7.028E-02	7.119E-02	7.469E-02	7.948E-02	8.614E-02	9.331E-02	9.992E-02
1.773E+00	8.468E-02	7.510E-02	7.164E-02	7.079E-02	7.496E-02	7.929E-02	8.800E-02	9.323E-02	1.010E-01
1.795E+00	8.808E-02	7.766E-02	7.266E-02	6.978E-02	7.458E-02	7.940E-02	8.599E-02	9.520E-02	1.036E-01
1.818E+00	8.941E-02	7.855E-02	7.165E-02	6.961E-02	7.301E-02	7.906E-02	8.640E-02	9.498E-02	1.049E-01
1.841E+00	8.980E-02	7.857E-02	7.136E-02	6.785E-02	7.135E-02	7.774E-02	8.665E-02	9.428E-02	1.061E-01
1.864E+00	8.890E-02	7.839E-02	7.026E-02	6.621E-02	7.071E-02	7.667E-02	8.378E-02	9.420E-02	1.088E-01
1.886E+00	8.643E-02	7.554E-02	6.820E-02	6.492E-02	7.010E-02	7.580E-02	8.477E-02	9.442E-02	1.091E-01
1.909E+00	8.530E-02	7.379E-02	6.630E-02	6.460E-02	6.876E-02	7.422E-02	8.326E-02	9.317E-02	1.070E-01
1.932E+00	8.292E-02	7.184E-02	6.362E-02	6.320E-02	6.602E-02	7.382E-02	8.156E-02	9.120E-02	1.051E-01
1.955E+00	8.079E-02	7.000E-02	6.201E-02	6.133E-02	6.510E-02	7.438E-02	8.183E-02	8.975E-02	1.035E-01
1.977E+00	7.775E-02	6.718E-02	6.061E-02	6.444E-02	6.401E-02	7.222E-02	8.111E-02	8.874E-02	1.023E-01
2.000E+00	7.665E-02	6.615E-02	5.857E-02	7.045E-02	6.305E-02	7.166E-02	8.058E-02	8.793E-02	1.007E-01
2.023E+00	8.571E-02	7.155E-02	6.076E-02	5.942E-02	6.056E-02	6.973E-02	7.918E-02	8.613E-02	9.365E-02
2.045E+00	8.407E-02	7.094E-02	5.962E-02	5.690E-02	6.090E-02	7.027E-02	7.876E-02	8.619E-02	9.347E-02
2.068E+00	8.393E-02	7.037E-02	5.992E-02	5.818E-02	6.175E-02	7.064E-02	7.869E-02	8.536E-02	9.307E-02
2.091E+00	8.298E-02	7.008E-02	5.991E-02	5.781E-02	6.242E-02	7.171E-02	7.865E-02	8.736E-02	9.545E-02
2.114E+00	8.113E-02	6.893E-02	5.956E-02	5.853E-02	6.331E-02	7.249E-02	7.847E-02	8.838E-02	9.381E-02
2.136E+00	7.945E-02	6.825E-02	5.818E-02	5.790E-02	6.266E-02	7.263E-02	7.802E-02	8.697E-02	9.300E-02
2.159E+00	7.708E-02	6.628E-02	5.786E-02	5.771E-02	6.200E-02	7.270E-02	7.804E-02	8.523E-02	9.221E-02
2.182E+00	7.351E-02	6.422E-02	5.738E-02	5.680E-02	6.208E-02	7.142E-02	7.578E-02	8.355E-02	9.064E-02
2.205E+00	7.200E-02	6.228E-02	5.620E-02	5.626E-02	6.424E-02	6.881E-02	7.466E-02	8.245E-02	8.897E-02
2.227E+00	6.744E-02	6.062E-02	5.767E-02	5.591E-02	6.356E-02	6.835E-02	7.177E-02	7.970E-02	8.740E-02
2.250E+00	6.349E-02	5.886E-02	5.756E-02	5.724E-02	6.056E-02	6.561E-02	6.846E-02	7.764E-02	8.330E-02
2.273E+00	6.298E-02	6.119E-02	5.539E-02	5.741E-02	6.168E-02	6.515E-02	6.636E-02	7.741E-02	8.031E-02
2.295E+00	6.669E-02	6.076E-02	5.804E-02	6.143E-02	6.168E-02	6.442E-02	6.528E-02	7.335E-02	8.051E-02
2.318E+00	7.028E-02	7.894E-02	6.918E-02	6.986E-02	6.987E-02	6.757E-02	6.611E-02	7.322E-02	7.712E-02
2.341E+00	7.598E-02	7.351E-02	7.123E-02	7.206E-02	6.851E-02	6.908E-02	7.218E-02	7.319E-02	7.479E-02
2.364E+00	7.314E-02	7.553E-02	7.507E-02	7.823E-02	7.683E-02	7.633E-02	7.408E-02	7.873E-02	7.860E-02
2.386E+00	1.382E-01	1.622E-01	1.348E-01	1.464E-01	1.292E-01	1.475E-01	2.208E-01	2.094E-01	1.761E-01
2.409E+00	4.170E-01	5.004E-01	4.895E-01	4.482E-01	4.305E-01	4.837E-01	3.819E-01	4.198E-01	4.635E-01
2.432E+00	4.723E-01	4.064E-01	4.347E-01	5.272E-01	4.358E-01	5.094E-01	4.858E-01	4.479E-01	4.775E-01
2.455E+00	3.473E-01	3.190E-01	3.746E-01	4.893E-01	2.359E-01	3.357E-01	2.125E-01	2.261E-01	4.390E-01
2.477E+00	2.908E-01	3.870E-01	2.870E-01	2.737E-01	1.476E-01	3.091E-01	6.505E-02	7.846E-02	1.576E-01

X/P	Y=2.409P	Y=2.432P	Y=2.455P	Y=2.477P	Y=2.5P
0.000E+00	8.876E-02	7.658E-02	6.914E-02	6.695E-02	6.823E-02
2.274E-02	9.226E-02	7.939E-02	7.456E-02	6.634E-02	7.035E-02
4.544E-02	9.560E-02	8.013E-02	7.276E-02	6.923E-02	7.085E-02
6.818E-02	9.784E-02	8.497E-02	7.477E-02	6.995E-02	7.181E-02
9.091E-02	9.883E-02	8.448E-02	7.448E-02	6.981E-02	7.321E-02
1.137E-01	9.917E-02	8.531E-02	7.568E-02	6.886E-02	7.687E-02
1.364E-01	9.627E-02	8.384E-02	7.371E-02	6.941E-02	7.621E-02
1.591E-01	9.388E-02	8.064E-02	7.327E-02	7.123E-02	7.630E-02
1.818E-01	1.004E-01	7.838E-02	7.287E-02	7.317E-02	7.693E-02
2.046E-01	9.158E-02	7.540E-02	7.402E-02	7.299E-02	7.753E-02
2.273E-01	8.764E-02	7.550E-02	7.045E-02	7.304E-02	8.133E-02
2.500E-01	8.276E-02	7.049E-02	7.104E-02	7.574E-02	8.151E-02
2.727E-01	7.879E-02	7.043E-02	7.174E-02	7.525E-02	8.316E-02
2.954E-01	7.743E-02	6.832E-02	7.313E-02	7.671E-02	8.280E-02
3.182E-01	7.015E-02	6.774E-02	7.473E-02	7.732E-02	8.520E-02
3.409E-01	6.866E-02	7.029E-02	7.442E-02	7.932E-02	8.474E-02
3.637E-01	6.809E-02	7.012E-02	7.785E-02	7.950E-02	8.547E-02
3.864E-01	6.537E-02	6.961E-02	7.748E-02	8.109E-02	8.638E-02
4.091E-01	6.732E-02	7.292E-02	7.930E-02	8.049E-02	8.658E-02
4.318E-01	6.722E-02	7.239E-02	7.672E-02	8.043E-02	8.612E-02
4.546E-01	6.841E-02	7.245E-02	7.897E-02	8.054E-02	8.677E-02
4.773E-01	6.744E-02	7.406E-02	7.885E-02	8.155E-02	8.694E-02
5.000E-01	6.722E-02	7.221E-02	7.772E-02	8.185E-02	8.697E-02
5.227E-01	6.728E-02	7.167E-02	7.993E-02	8.163E-02	8.766E-02
5.454E-01	6.737E-02	7.158E-02	7.984E-02	8.114E-02	8.751E-02
5.682E-01	6.604E-02	7.218E-02	7.697E-02	7.964E-02	8.545E-02
5.909E-01	6.679E-02	7.232E-02	7.733E-02	8.035E-02	8.482E-02
6.137E-01	6.438E-02	7.095E-02	7.504E-02	7.759E-02	8.351E-02
6.364E-01	6.483E-02	7.096E-02	7.327E-02	7.809E-02	8.235E-02
6.591E-01	6.709E-02	7.270E-02	7.559E-02	7.597E-02	8.224E-02
6.818E-01	6.790E-02	6.994E-02	7.266E-02	7.457E-02	8.080E-02
7.046E-01	6.975E-02	7.051E-02	7.043E-02	7.212E-02	8.024E-02
7.273E-01	7.287E-02	7.121E-02	7.079E-02	6.911E-02	7.593E-02
7.500E-01	7.588E-02	6.927E-02	6.668E-02	6.756E-02	7.573E-02
7.727E-01	7.909E-02	7.031E-02	6.539E-02	6.656E-02	7.527E-02
7.954E-01	8.095E-02	6.910E-02	6.371E-02	6.376E-02	7.028E-02

8.182E-01	8.314E-02	6.797E-02	6.585E-02	6.147E-02	6.999E-02
8.409E-01	8.305E-02	6.518E-02	5.861E-02	5.864E-02	6.669E-02
8.637E-01	8.616E-02	6.767E-02	6.155E-02	5.708E-02	6.440E-02
8.864E-01	8.322E-02	6.685E-02	6.368E-02	5.552E-02	6.306E-02
9.091E-01	8.298E-02	6.796E-02	5.926E-02	5.379E-02	6.093E-02
9.318E-01	8.076E-02	6.770E-02	5.837E-02	5.358E-02	6.038E-02
9.546E-01	7.835E-02	6.859E-02	5.781E-02	5.519E-02	5.992E-02
9.773E-01	7.881E-02	7.321E-02	5.847E-02	5.906E-02	6.111E-02
1.000E+00	8.058E-02	7.129E-02	5.909E-02	5.789E-02	6.110E-02
1.023E+00	8.206E-02	7.385E-02	6.026E-02	5.873E-02	6.251E-02
1.045E+00	8.580E-02	7.523E-02	6.377E-02	6.045E-02	6.298E-02
1.068E+00	8.661E-02	7.561E-02	6.265E-02	6.124E-02	6.355E-02
1.091E+00	8.844E-02	7.573E-02	6.365E-02	6.152E-02	6.619E-02
1.114E+00	8.919E-02	7.356E-02	6.313E-02	6.179E-02	6.796E-02
1.136E+00	8.732E-02	7.407E-02	6.384E-02	6.274E-02	6.925E-02
1.159E+00	8.435E-02	6.946E-02	6.366E-02	6.370E-02	7.133E-02
1.182E+00	8.279E-02	6.622E-02	6.267E-02	6.469E-02	7.146E-02
1.205E+00	7.776E-02	6.537E-02	6.207E-02	6.561E-02	7.307E-02
1.227E+00	7.341E-02	6.720E-02	6.317E-02	6.703E-02	7.416E-02
1.250E+00	6.806E-02	6.213E-02	6.357E-02	6.823E-02	7.431E-02
1.273E+00	6.506E-02	6.095E-02	6.456E-02	7.135E-02	7.764E-02
1.295E+00	6.216E-02	6.302E-02	6.862E-02	7.530E-02	7.907E-02
1.318E+00	6.137E-02	6.212E-02	6.973E-02	7.579E-02	8.054E-02
1.341E+00	6.025E-02	6.527E-02	6.967E-02	7.631E-02	8.111E-02
1.364E+00	6.170E-02	6.719E-02	7.180E-02	7.862E-02	8.318E-02
1.386E+00	6.186E-02	7.065E-02	7.495E-02	8.175E-02	8.355E-02
1.409E+00	6.301E-02	6.949E-02	7.697E-02	8.151E-02	8.527E-02
1.432E+00	6.481E-02	7.162E-02	7.863E-02	8.203E-02	8.561E-02
1.455E+00	6.730E-02	7.307E-02	7.846E-02	8.329E-02	8.747E-02
1.477E+00	6.688E-02	7.302E-02	7.825E-02	8.464E-02	8.883E-02
1.500E+00	6.714E-02	7.494E-02	8.038E-02	8.337E-02	8.825E-02
1.523E+00	6.814E-02	7.812E-02	7.927E-02	8.431E-02	8.831E-02
1.545E+00	6.909E-02	7.484E-02	7.867E-02	8.396E-02	8.815E-02
1.568E+00	6.896E-02	7.580E-02	7.973E-02	8.411E-02	8.818E-02
1.591E+00	7.051E-02	7.855E-02	8.076E-02	8.435E-02	8.693E-02
1.614E+00	7.168E-02	7.673E-02	7.985E-02	8.405E-02	8.674E-02
1.636E+00	7.435E-02	7.978E-02	7.864E-02	8.399E-02	8.869E-02
1.659E+00	7.651E-02	7.903E-02	7.935E-02	8.515E-02	8.611E-02

1.682E+00	8.318E-02	7.957E-02	7.847E-02	8.092E-02	8.614E-02
1.705E+00	8.185E-02	8.070E-02	8.125E-02	8.103E-02	8.369E-02
1.727E+00	8.506E-02	7.862E-02	7.796E-02	8.010E-02	8.173E-02
1.750E+00	8.520E-02	7.751E-02	7.454E-02	7.750E-02	8.097E-02
1.773E+00	8.696E-02	7.785E-02	7.316E-02	7.432E-02	7.805E-02
1.795E+00	8.799E-02	7.778E-02	7.340E-02	7.223E-02	7.768E-02
1.818E+00	8.885E-02	7.676E-02	7.162E-02	7.166E-02	7.669E-02
1.841E+00	8.706E-02	7.600E-02	7.003E-02	6.879E-02	7.373E-02
1.864E+00	8.623E-02	7.416E-02	6.830E-02	6.534E-02	7.381E-02
1.886E+00	8.246E-02	7.026E-02	6.606E-02	6.394E-02	6.900E-02
1.909E+00	7.716E-02	6.807E-02	6.098E-02	6.091E-02	6.649E-02
1.932E+00	7.290E-02	6.415E-02	5.908E-02	5.894E-02	6.532E-02
1.955E+00	7.024E-02	6.159E-02	5.601E-02	5.761E-02	6.283E-02
1.977E+00	6.786E-02	5.909E-02	5.466E-02	5.641E-02	6.186E-02
2.000E+00	6.564E-02	5.609E-02	5.153E-02	5.556E-02	6.178E-02
2.023E+00	7.245E-02	6.542E-02	5.358E-02	5.245E-02	6.086E-02
2.045E+00	7.526E-02	6.645E-02	5.426E-02	5.402E-02	6.148E-02
2.068E+00	7.430E-02	6.777E-02	5.346E-02	5.652E-02	6.310E-02
2.091E+00	7.541E-02	6.642E-02	5.589E-02	5.887E-02	6.650E-02
2.114E+00	7.293E-02	6.063E-02	5.654E-02	6.014E-02	7.021E-02
2.136E+00	7.173E-02	6.142E-02	5.580E-02	6.384E-02	7.268E-02
2.159E+00	6.885E-02	5.899E-02	5.697E-02	6.581E-02	7.802E-02
2.182E+00	6.825E-02	6.103E-02	6.264E-02	7.211E-02	8.307E-02
2.205E+00	8.504E-02	7.159E-02	7.154E-02	7.573E-02	8.744E-02
2.227E+00	9.175E-02	7.163E-02	8.017E-02	7.768E-02	9.138E-02
2.250E+00	1.107E-01	8.117E-02	1.000E-01	8.363E-02	1.020E-01
2.273E+00	1.445E-01	1.200E-01	1.096E-01	9.682E-02	1.089E-01
2.295E+00	1.591E-01	1.544E-01	1.252E-01	1.163E-01	1.511E-01
2.318E+00	2.349E-01	1.620E-01	2.112E-01	1.462E-01	2.111E-01
2.341E+00	2.394E-01	1.694E-01	3.657E-01	1.833E-01	2.770E-01
2.364E+00	3.667E-01	2.799E-01	3.800E-01	2.475E-01	2.692E-01
2.386E+00	3.779E-01	3.601E-01	2.912E-01	3.256E-01	2.122E-01
2.409E+00	3.594E-01	2.632E-01	3.551E-01	1.942E-01	1.464E-01
2.432E+00	3.642E-01	2.596E-01	2.898E-01	1.985E-01	1.498E-01
2.455E+00	2.287E-01	1.390E-01	1.889E-01	1.614E-01	1.140E-01
2.477E+00	4.271E-02	1.572E-02	3.660E-02	3.996E-02	4.388E-02

## 2. UPSTREAM DIGIT DATA (Figure A14)

## a) Y/P=0.5

X/Pi	W/W <sub>bulk</sub>	V/W <sub>bulk</sub>	W <sub>rms</sub> /W <sub>bulk</sub>	V <sub>rms</sub> /W <sub>bulk</sub>	v <sub>w</sub> /(W <sub>bulk</sub> ) <sup>2</sup>
0.000E+00	1.128E+00	-1.888E-02	6.605E-02	4.200E-02	-5.897E-05
2.274E-02	1.137E+00	-1.874E-02	6.629E-02	4.295E-02	-4.457E-05
4.544E-02	1.142E+00	-1.877E-02	6.749E-02	4.324E-02	-7.667E-05
6.818E-02	1.158E+00	-1.942E-02	6.932E-02	4.440E-02	-8.122E-05
9.091E-02	1.165E+00	-1.918E-02	7.065E-02	4.416E-02	-1.002E-05
1.137E-01	1.178E+00	-1.988E-02	7.073E-02	4.468E-02	2.059E-05
1.364E-01	1.190E+00	-2.040E-02	7.201E-02	4.707E-02	6.834E-05
1.591E-01	1.203E+00	-2.056E-02	7.271E-02	4.684E-02	6.195E-05
1.818E-01	1.211E+00	-2.237E-02	7.248E-02	4.690E-02	1.031E-04
2.046E-01	1.222E+00	-2.240E-02	7.190E-02	4.796E-02	1.373E-04
2.273E-01	1.232E+00	-2.415E-02	7.052E-02	4.819E-02	5.222E-05
2.500E-01	1.245E+00	-2.564E-02	7.188E-02	4.869E-02	9.635E-05
2.727E-01	1.258E+00	-2.430E-02	7.111E-02	4.806E-02	3.376E-05
2.954E-01	1.265E+00	-2.652E-02	6.820E-02	4.797E-02	1.358E-04
3.182E-01	1.274E+00	-2.797E-02	6.640E-02	4.801E-02	1.171E-04
3.409E-01	1.286E+00	-2.615E-02	6.360E-02	4.578E-02	8.942E-05
3.637E-01	1.295E+00	-2.753E-02	6.265E-02	4.475E-02	8.862E-05
3.864E-01	1.303E+00	-2.768E-02	6.016E-02	4.356E-02	7.630E-05
4.091E-01	1.307E+00	-2.985E-02	6.324E-02	4.204E-02	7.743E-05
4.318E-01	1.313E+00	-3.011E-02	5.541E-02	4.118E-02	4.921E-05
4.546E-01	1.314E+00	-3.037E-02	5.521E-02	3.969E-02	9.888E-05
4.773E-01	1.309E+00	-3.310E-02	5.549E-02	4.070E-02	1.381E-04
5.000E-01	1.310E+00	-3.204E-02	5.712E-02	4.041E-02	1.405E-04
5.227E-01	1.303E+00	-3.048E-02	5.679E-02	4.134E-02	8.064E-05
5.454E-01	1.298E+00	-3.076E-02	6.020E-02	4.200E-02	8.984E-05
5.682E-01	1.286E+00	-3.198E-02	6.203E-02	4.277E-02	1.234E-04
5.909E-01	1.274E+00	-3.125E-02	6.511E-02	4.382E-02	1.310E-04
6.137E-01	1.266E+00	-3.159E-02	6.465E-02	4.486E-02	1.139E-04
6.364E-01	1.257E+00	-3.177E-02	6.543E-02	4.501E-02	1.305E-04
6.591E-01	1.248E+00	-3.152E-02	6.699E-02	4.486E-02	1.046E-04
6.818E-01	1.236E+00	-3.002E-02	6.725E-02	4.508E-02	1.052E-04
7.046E-01	1.221E+00	-3.155E-02	6.692E-02	4.442E-02	1.627E-04
7.273E-01	1.213E+00	-2.986E-02	6.811E-02	4.368E-02	1.462E-04
7.500E-01	1.200E+00	-2.675E-02	6.730E-02	4.382E-02	1.658E-05

7.727E-01	1.187E+00	-2.759E-02	6.735E-02	4.303E-02	5.206E-05
7.954E-01	1.177E+00	-2.644E-02	6.582E-02	4.257E-02	5.492E-06
8.182E-01	1.165E+00	-2.578E-02	6.462E-02	4.196E-02	3.335E-05
8.409E-01	1.155E+00	-2.319E-02	6.115E-02	4.042E-02	2.283E-05
8.637E-01	1.145E+00	-2.289E-02	6.069E-02	4.055E-02	-7.910E-06
8.864E-01	1.143E+00	-2.222E-02	5.928E-02	4.100E-02	-2.436E-05
9.091E-01	1.140E+00	-2.169E-02	5.763E-02	4.029E-02	3.817E-05
9.318E-01	1.136E+00	-2.076E-02	5.817E-02	4.043E-02	-3.906E-06
9.546E-01	1.137E+00	-2.115E-02	5.882E-02	4.059E-02	7.113E-06
9.773E-01	1.142E+00	-2.048E-02	6.008E-02	4.188E-02	3.743E-05
1.000E+00	1.146E+00	-2.024E-02	6.251E-02	4.194E-02	-1.253E-06
1.023E+00	1.152E+00	-2.016E-02	6.311E-02	4.297E-02	-1.314E-05
1.045E+00	1.158E+00	-2.040E-02	6.538E-02	4.421E-02	9.796E-06
1.068E+00	1.162E+00	-2.134E-02	6.493E-02	4.528E-02	9.228E-05
1.091E+00	1.170E+00	-2.158E-02	6.699E-02	4.721E-02	1.207E-04
1.114E+00	1.182E+00	-2.214E-02	6.670E-02	4.646E-02	1.190E-04
1.136E+00	1.186E+00	-2.280E-02	6.816E-02	4.669E-02	9.644E-05
1.159E+00	1.193E+00	-2.380E-02	6.739E-02	4.766E-02	2.054E-04
1.182E+00	1.200E+00	-2.607E-02	6.879E-02	4.825E-02	1.958E-04
1.205E+00	1.208E+00	-2.592E-02	6.833E-02	4.865E-02	2.623E-04
1.227E+00	1.215E+00	-2.709E-02	6.805E-02	4.809E-02	2.068E-04
1.250E+00	1.229E+00	-2.840E-02	6.743E-02	4.845E-02	2.734E-04
1.273E+00	1.235E+00	-2.834E-02	6.642E-02	4.678E-02	2.399E-04
1.295E+00	1.246E+00	-2.973E-02	6.383E-02	4.709E-02	2.326E-04
1.318E+00	1.255E+00	-3.068E-02	6.281E-02	4.536E-02	2.795E-04
1.341E+00	1.261E+00	-3.185E-02	6.088E-02	4.427E-02	2.330E-04
1.364E+00	1.266E+00	-3.281E-02	5.986E-02	4.335E-02	2.525E-04
1.386E+00	1.273E+00	-3.169E-02	5.726E-02	4.273E-02	2.179E-04
1.409E+00	1.274E+00	-3.200E-02	5.733E-02	4.138E-02	1.811E-04
1.432E+00	1.274E+00	-3.265E-02	5.731E-02	4.114E-02	1.922E-04
1.455E+00	1.266E+00	-3.286E-02	5.980E-02	4.133E-02	2.080E-04
1.477E+00	1.265E+00	-3.394E-02	6.096E-02	4.209E-02	2.967E-04
1.500E+00	1.258E+00	-3.312E-02	6.283E-02	4.340E-02	2.300E-04
1.523E+00	1.246E+00	-3.398E-02	6.633E-02	4.495E-02	1.688E-04
1.545E+00	1.237E+00	-3.327E-02	6.736E-02	4.561E-02	2.664E-04
1.568E+00	1.226E+00	-3.399E-02	6.870E-02	4.557E-02	2.897E-04
1.591E+00	1.214E+00	-3.302E-02	7.094E-02	4.711E-02	2.698E-04
1.614E+00	1.201E+00	-3.320E-02	7.292E-02	4.784E-02	3.292E-04

1.636E+00	1.187E+00	-3.197E-02	7.287E-02	4.736E-02	2.631E-04
1.659E+00	1.170E+00	-3.164E-02	7.571E-02	4.878E-02	2.920E-04
1.682E+00	1.157E+00	-2.942E-02	7.649E-02	4.759E-02	2.399E-04
1.705E+00	1.143E+00	-2.826E-02	7.783E-02	4.892E-02	2.653E-04
1.727E+00	1.128E+00	-2.618E-02	7.830E-02	4.739E-02	2.642E-04
1.750E+00	1.112E+00	-2.374E-02	7.990E-02	4.722E-02	3.550E-04
1.773E+00	1.098E+00	-2.134E-02	7.881E-02	4.731E-02	3.920E-04
1.795E+00	1.078E+00	-2.003E-02	7.876E-02	4.594E-02	3.280E-04
1.818E+00	1.058E+00	-1.872E-02	7.815E-02	4.501E-02	3.450E-04
1.841E+00	1.047E+00	-1.759E-02	7.650E-02	4.408E-02	4.070E-04
1.864E+00	1.032E+00	-1.589E-02	7.364E-02	4.297E-02	3.630E-04
1.886E+00	1.015E+00	-1.584E-02	7.280E-02	4.212E-02	3.980E-04
1.909E+00	1.004E+00	-1.364E-02	6.883E-02	4.076E-02	3.850E-04
1.932E+00	9.998E-01	-1.341E-02	6.702E-02	4.080E-02	4.510E-04
1.955E+00	9.935E-01	-1.283E-02	6.606E-02	4.002E-02	4.510E-04
1.977E+00	9.915E-01	-1.350E-02	6.559E-02	3.988E-02	5.120E-04
2.000E+00	9.866E-01	-1.424E-02	6.646E-02	4.016E-02	5.830E-04
2.023E+00	9.855E-01	-1.509E-02	6.170E-02	3.944E-02	3.364E-04
2.045E+00	9.873E-01	-1.579E-02	6.156E-02	4.042E-02	3.624E-04
2.068E+00	9.892E-01	-1.746E-02	6.204E-02	4.003E-02	4.219E-04
2.091E+00	9.925E-01	-1.755E-02	6.146E-02	4.166E-02	4.514E-04
2.114E+00	9.965E-01	-1.920E-02	6.062E-02	4.119E-02	3.898E-04
2.136E+00	9.998E-01	-2.130E-02	6.111E-02	4.222E-02	4.457E-04
2.159E+00	1.004E+00	-2.120E-02	5.874E-02	4.182E-02	3.717E-04
2.182E+00	1.007E+00	-2.172E-02	5.783E-02	4.061E-02	3.646E-04
2.205E+00	1.011E+00	-2.358E-02	5.689E-02	3.928E-02	3.617E-04
2.227E+00	1.013E+00	-2.595E-02	5.667E-02	4.073E-02	3.896E-04
2.250E+00	1.010E+00	-2.497E-02	5.589E-02	3.869E-02	3.589E-04
2.273E+00	1.010E+00	-2.543E-02	5.635E-02	3.979E-02	3.146E-04
2.295E+00	1.009E+00	-2.547E-02	5.750E-02	3.775E-02	2.782E-04
2.318E+00	1.001E+00	-2.524E-02	5.972E-02	3.934E-02	2.378E-04
2.341E+00	9.884E-01	-2.634E-02	6.540E-02	4.192E-02	2.721E-04
2.364E+00	9.737E-01	-2.643E-02	7.075E-02	4.242E-02	2.071E-04
2.386E+00	9.564E-01	-2.586E-02	8.506E-02	4.423E-02	1.630E-04
2.409E+00	9.174E-01	-2.629E-02	1.337E-01	4.692E-02	2.866E-04
2.432E+00	6.931E-01	-2.311E-02	3.998E-01	4.499E-02	-1.900E-03
2.455E+00	1.693E-01	-8.170E-03	3.494E-01	2.944E-02	-2.660E-03
2.477E+00	9.939E-02	-7.110E-03	2.712E-01	2.410E-02	-9.884E-04

## b) Y/P=1.5

X/P	W/W <sub>bulk</sub>	V/W <sub>bulk</sub>	w <sub>rms</sub> /W <sub>bulk</sub>	v <sub>rms</sub> /W <sub>bulk</sub>	vw/(W <sub>bulk</sub> ) <sup>2</sup>
0.000E+00	1.104E+00	-2.200E-02	5.814E-02	3.983E-02	-5.671E-06
2.274E-02	1.104E+00	-2.171E-02	5.954E-02	4.033E-02	4.455E-05
4.544E-02	1.109E+00	-2.149E-02	5.986E-02	3.955E-02	1.618E-05
6.818E-02	1.117E+00	-2.223E-02	6.065E-02	4.062E-02	1.978E-05
9.091E-02	1.118E+00	-2.260E-02	6.201E-02	4.114E-02	-1.296E-05
1.137E-01	1.129E+00	-2.493E-02	6.424E-02	4.164E-02	7.334E-05
1.364E-01	1.135E+00	-2.684E-02	6.446E-02	4.263E-02	1.262E-04
1.591E-01	1.147E+00	-2.919E-02	6.533E-02	4.292E-02	8.488E-05
1.818E-01	1.148E+00	-3.175E-02	6.636E-02	4.370E-02	1.808E-04
2.046E-01	1.157E+00	-3.453E-02	6.755E-02	4.447E-02	1.815E-04
2.273E-01	1.168E+00	-3.546E-02	6.693E-02	4.512E-02	1.159E-04
2.500E-01	1.173E+00	-3.876E-02	6.848E-02	4.687E-02	1.540E-04
2.727E-01	1.185E+00	-4.075E-02	6.755E-02	4.538E-02	2.111E-04
2.954E-01	1.195E+00	-4.123E-02	6.624E-02	4.608E-02	1.320E-04
3.182E-01	1.204E+00	-4.307E-02	6.536E-02	4.522E-02	1.363E-04
3.409E-01	1.212E+00	-4.479E-02	6.374E-02	4.477E-02	1.508E-04
3.637E-01	1.222E+00	-4.641E-02	6.179E-02	4.294E-02	1.510E-04
3.864E-01	1.233E+00	-4.631E-02	5.985E-02	4.200E-02	7.671E-05
4.091E-01	1.237E+00	-4.869E-02	5.695E-02	4.058E-02	1.213E-04
4.318E-01	1.246E+00	-4.835E-02	5.655E-02	4.065E-02	1.261E-04
4.546E-01	1.246E+00	-5.011E-02	5.621E-02	3.961E-02	1.338E-04
4.773E-01	1.245E+00	-4.911E-02	5.794E-02	3.997E-02	1.211E-04
5.000E-01	1.240E+00	-5.087E-02	5.923E-02	4.047E-02	1.764E-04
5.227E-01	1.235E+00	-5.089E-02	6.249E-02	4.112E-02	2.012E-04
5.454E-01	1.224E+00	-5.293E-02	6.466E-02	4.225E-02	2.284E-04
5.682E-01	1.218E+00	-5.346E-02	6.813E-02	4.283E-02	2.206E-04
5.909E-01	1.206E+00	-5.277E-02	7.146E-02	4.438E-02	2.081E-04
6.137E-01	1.195E+00	-5.082E-02	7.404E-02	4.470E-02	2.274E-04
6.364E-01	1.178E+00	-5.147E-02	7.540E-02	4.590E-02	2.177E-04
6.591E-01	1.171E+00	-5.072E-02	7.622E-02	4.579E-02	2.378E-04
6.818E-01	1.159E+00	-4.930E-02	7.781E-02	4.637E-02	2.475E-04
7.046E-01	1.148E+00	-4.671E-02	8.074E-02	4.695E-02	2.201E-04
7.273E-01	1.130E+00	-4.429E-02	8.155E-02	4.572E-02	1.230E-04
7.500E-01	1.111E+00	-4.105E-02	8.045E-02	4.543E-02	1.456E-04
7.727E-01	1.101E+00	-3.971E-02	7.973E-02	4.486E-02	1.500E-04

7.954E-01	1.089E+00	-3.679E-02	8.065E-02	4.495E-02	1.570E-04
8.182E-01	1.072E+00	-3.442E-02	7.698E-02	4.518E-02	1.225E-04
8.409E-01	1.062E+00	-3.196E-02	7.473E-02	4.301E-02	9.067E-05
8.637E-01	1.051E+00	-2.890E-02	7.032E-02	4.278E-02	7.161E-05
8.864E-01	1.044E+00	-2.750E-02	6.695E-02	4.186E-02	5.753E-05
9.091E-01	1.043E+00	-2.486E-02	6.778E-02	4.277E-02	1.573E-05
9.318E-01	1.041E+00	-2.319E-02	6.603E-02	4.179E-02	1.536E-05
9.546E-01	1.043E+00	-2.259E-02	6.710E-02	4.154E-02	-3.872E-05
9.773E-01	1.050E+00	-2.068E-02	6.876E-02	4.271E-02	-1.551E-05
1.000E+00	1.056E+00	-2.069E-02	6.987E-02	4.248E-02	4.181E-05
1.023E+00	1.068E+00	-2.142E-02	7.138E-02	4.255E-02	1.039E-04
1.045E+00	1.072E+00	-2.113E-02	7.333E-02	4.448E-02	8.530E-05
1.068E+00	1.084E+00	-2.225E-02	7.357E-02	4.424E-02	1.312E-04
1.091E+00	1.096E+00	-2.285E-02	7.725E-02	4.495E-02	1.696E-04
1.114E+00	1.103E+00	-2.411E-02	7.622E-02	4.639E-02	2.156E-04
1.136E+00	1.118E+00	-2.639E-02	7.659E-02	4.708E-02	3.113E-04
1.159E+00	1.126E+00	-2.849E-02	7.597E-02	4.774E-02	2.664E-04
1.182E+00	1.133E+00	-3.085E-02	7.631E-02	4.950E-02	3.989E-04
1.205E+00	1.146E+00	-3.201E-02	7.594E-02	4.874E-02	4.035E-04
1.227E+00	1.160E+00	-3.375E-02	7.383E-02	4.937E-02	3.288E-04
1.250E+00	1.169E+00	-3.591E-02	7.477E-02	4.948E-02	4.086E-04
1.273E+00	1.175E+00	-3.851E-02	7.229E-02	4.941E-02	4.207E-04
1.295E+00	1.187E+00	-4.072E-02	7.103E-02	4.746E-02	3.386E-04
1.318E+00	1.194E+00	-4.280E-02	6.827E-02	4.617E-02	3.651E-04
1.341E+00	1.206E+00	-4.292E-02	6.723E-02	4.545E-02	3.181E-04
1.364E+00	1.210E+00	-4.592E-02	6.361E-02	4.416E-02	3.464E-04
1.386E+00	1.220E+00	-4.542E-02	6.110E-02	4.250E-02	3.024E-04
1.409E+00	1.222E+00	-4.572E-02	6.019E-02	4.272E-02	2.604E-04
1.432E+00	1.225E+00	-4.708E-02	5.893E-02	4.168E-02	2.590E-04
1.455E+00	1.222E+00	-4.761E-02	5.860E-02	4.101E-02	2.781E-04
1.477E+00	1.218E+00	-4.788E-02	6.016E-02	4.169E-02	2.649E-04
1.500E+00	1.213E+00	-4.953E-02	6.103E-02	4.164E-02	2.835E-04
1.523E+00	1.207E+00	-5.042E-02	6.394E-02	4.281E-02	3.190E-04
1.545E+00	1.193E+00	-5.007E-02	6.740E-02	4.461E-02	3.764E-04
1.568E+00	1.186E+00	-5.094E-02	6.829E-02	4.424E-02	3.273E-04
1.591E+00	1.171E+00	-5.091E-02	7.010E-02	4.542E-02	4.410E-04
1.614E+00	1.159E+00	-5.184E-02	7.123E-02	4.703E-02	4.595E-04
1.636E+00	1.149E+00	-5.109E-02	7.429E-02	4.710E-02	4.565E-04

1.659E+00	1.140E+00	-4.941E-02	7.249E-02	4.716E-02	4.476E-04
1.682E+00	1.122E+00	-4.989E-02	7.475E-02	4.742E-02	4.733E-04
1.705E+00	1.113E+00	-4.733E-02	7.485E-02	4.637E-02	3.896E-04
1.727E+00	1.100E+00	-4.669E-02	7.823E-02	4.681E-02	4.410E-04
1.750E+00	1.087E+00	-4.358E-02	7.537E-02	4.678E-02	5.010E-04
1.773E+00	1.075E+00	-4.016E-02	7.405E-02	4.661E-02	4.600E-04
1.795E+00	1.064E+00	-3.671E-02	7.357E-02	4.550E-02	4.680E-04
1.818E+00	1.045E+00	-3.466E-02	7.321E-02	4.531E-02	4.420E-04
1.841E+00	1.035E+00	-3.207E-02	7.407E-02	4.375E-02	3.960E-04
1.864E+00	1.017E+00	-2.970E-02	7.125E-02	4.333E-02	3.520E-04
1.886E+00	1.005E+00	-2.760E-02	7.122E-02	4.233E-02	2.930E-04
1.909E+00	9.926E-01	-2.643E-02	6.731E-02	4.076E-02	2.700E-04
1.932E+00	9.833E-01	-2.373E-02	6.834E-02	4.089E-02	3.560E-04
1.955E+00	9.787E-01	-2.345E-02	6.577E-02	4.081E-02	3.400E-04
1.977E+00	9.768E-01	-2.264E-02	6.478E-02	3.982E-02	3.780E-04
2.000E+00	9.697E-01	-2.282E-02	6.557E-02	3.965E-02	4.080E-04
2.023E+00	9.664E-01	-2.266E-02	6.131E-02	3.961E-02	3.085E-04
2.045E+00	9.668E-01	-2.369E-02	6.277E-02	4.026E-02	3.619E-04
2.068E+00	9.664E-01	-2.533E-02	6.244E-02	4.229E-02	4.128E-04
2.091E+00	9.665E-01	-2.596E-02	6.436E-02	4.082E-02	4.696E-04
2.114E+00	9.670E-01	-2.818E-02	6.436E-02	4.193E-02	4.846E-04
2.136E+00	9.708E-01	-2.993E-02	6.422E-02	4.213E-02	4.816E-04
2.159E+00	9.766E-01	-3.113E-02	6.336E-02	4.139E-02	4.894E-04
2.182E+00	9.825E-01	-3.292E-02	6.201E-02	4.163E-02	4.302E-04
2.205E+00	9.890E-01	-3.447E-02	6.188E-02	4.122E-02	4.591E-04
2.227E+00	9.959E-01	-3.520E-02	5.951E-02	4.092E-02	4.512E-04
2.250E+00	9.966E-01	-3.856E-02	6.009E-02	4.154E-02	4.884E-04
2.273E+00	1.001E+00	-3.946E-02	5.785E-02	3.911E-02	4.191E-04
2.295E+00	1.001E+00	-3.956E-02	5.720E-02	3.961E-02	3.598E-04
2.318E+00	9.992E-01	-4.126E-02	5.988E-02	3.862E-02	3.344E-04
2.341E+00	9.894E-01	-4.115E-02	6.461E-02	4.082E-02	3.128E-04
2.364E+00	9.759E-01	-4.368E-02	7.055E-02	4.282E-02	3.490E-04
2.386E+00	9.538E-01	-4.424E-02	8.630E-02	4.510E-02	3.159E-04
2.409E+00	8.791E-01	-4.567E-02	2.394E-01	4.826E-02	5.297E-05
2.432E+00	4.443E-01	-2.889E-02	4.585E-01	4.590E-02	-6.180E-03
2.455E+00	1.061E-01	-8.260E-03	2.853E-01	2.663E-02	-2.670E-03
2.477E+00	2.710E-03	-3.140E-03	5.194E-02	1.490E-02	-1.809E-05

## c) Y/P=2.455

X/	W/W <sub>bulk</sub>	V/W <sub>bulk</sub>	w <sub>rms</sub> /W <sub>bulk</sub>	v <sub>rms</sub> /W <sub>bulk</sub>	vw/(W <sub>bulk</sub> ) <sup>2</sup>
0.000E+00	8.145E-01	-2.317E-02	6.467E-02	3.821E-02	-4.021E-04
2.274E-02	8.250E-01	-2.219E-02	6.959E-02	3.813E-02	-3.587E-04
4.544E-02	8.282E-01	-2.279E-02	7.014E-02	4.882E-02	-3.826E-04
6.818E-02	8.387E-01	-1.979E-02	7.195E-02	4.079E-02	-3.541E-04
9.091E-02	8.633E-01	-1.992E-02	7.031E-02	5.283E-02	-2.816E-04
1.137E-01	8.865E-01	-1.972E-02	7.234E-02	5.034E-02	-1.502E-04
1.364E-01	8.997E-01	-1.942E-02	7.352E-02	5.118E-02	-1.126E-04
1.591E-01	9.192E-01	-2.020E-02	7.294E-02	5.415E-02	-1.249E-04
1.818E-01	9.365E-01	-2.005E-02	7.095E-02	6.222E-02	9.154E-05
2.046E-01	9.524E-01	-2.202E-02	7.142E-02	6.111E-02	3.342E-05
2.273E-01	9.726E-01	-2.219E-02	6.840E-02	6.000E-02	1.137E-04
2.500E-01	9.814E-01	-2.309E-02	7.193E-02	5.894E-02	6.660E-05
2.727E-01	9.882E-01	-2.681E-02	8.089E-02	5.797E-02	2.574E-04
2.954E-01	9.903E-01	-2.820E-02	8.378E-02	5.380E-02	4.127E-04
3.182E-01	9.939E-01	-3.247E-02	7.437E-02	5.690E-02	3.303E-04
3.409E-01	9.973E-01	-3.029E-02	7.383E-02	6.296E-02	4.485E-04
3.637E-01	9.935E-01	-3.364E-02	7.502E-02	5.397E-02	4.966E-04
3.864E-01	9.968E-01	-2.797E-02	7.664E-02	6.020E-02	5.036E-04
4.091E-01	9.978E-01	-2.908E-02	7.695E-02	5.157E-02	5.921E-04
4.318E-01	9.959E-01	-2.916E-02	7.751E-02	5.168E-02	6.675E-04
4.546E-01	9.875E-01	-3.213E-02	7.904E-02	5.502E-02	6.161E-04
4.773E-01	9.860E-01	-3.219E-02	8.060E-02	5.090E-02	7.183E-04
5.000E-01	9.843E-01	-3.472E-02	8.509E-02	6.094E-02	7.081E-04
5.227E-01	9.781E-01	-3.462E-02	7.994E-02	5.340E-02	7.491E-04
5.454E-01	9.732E-01	-3.694E-02	7.960E-02	6.047E-02	7.274E-04
5.682E-01	9.688E-01	-3.559E-02	7.815E-02	5.419E-02	8.096E-04
5.909E-01	9.643E-01	-3.652E-02	7.759E-02	5.297E-02	7.469E-04
6.137E-01	9.572E-01	-3.655E-02	7.937E-02	5.474E-02	6.955E-04
6.364E-01	9.485E-01	-3.654E-02	7.511E-02	5.338E-02	7.034E-04
6.591E-01	9.391E-01	-3.711E-02	7.430E-02	5.094E-02	7.385E-04
6.818E-01	9.351E-01	-3.654E-02	7.404E-02	4.505E-02	7.084E-04
7.046E-01	9.210E-01	-3.641E-02	7.193E-02	4.852E-02	5.590E-04
7.273E-01	9.192E-01	-3.479E-02	6.846E-02	4.665E-02	4.551E-04
7.500E-01	9.017E-01	-3.440E-02	6.793E-02	4.654E-02	5.405E-04
7.727E-01	8.963E-01	-3.387E-02	6.646E-02	4.632E-02	3.980E-04

7.954E-01	8.854E-01	-3.287E-02	6.660E-02	4.594E-02	3.307E-04
8.182E-01	8.702E-01	-3.247E-02	6.288E-02	4.064E-02	2.441E-04
8.409E-01	8.579E-01	-3.175E-02	5.972E-02	4.510E-02	8.005E-05
8.637E-01	8.482E-01	-3.067E-02	5.892E-02	4.449E-02	6.309E-05
8.864E-01	8.380E-01	-3.068E-02	5.747E-02	4.257E-02	2.226E-05
9.091E-01	8.325E-01	-2.848E-02	5.503E-02	3.959E-02	-1.296E-04
9.318E-01	8.284E-01	-2.738E-02	5.621E-02	4.248E-02	-1.393E-04
9.546E-01	8.285E-01	-2.732E-02	5.657E-02	4.291E-02	-1.960E-04
9.773E-01	8.304E-01	-2.596E-02	5.789E-02	3.762E-02	-2.597E-04
1.000E+00	8.340E-01	-2.319E-02	6.432E-02	4.392E-02	-3.109E-04
1.023E+00	8.404E-01	-2.214E-02	6.149E-02	4.431E-02	-2.383E-04
1.045E+00	8.512E-01	-2.074E-02	6.390E-02	4.670E-02	-3.268E-04
1.068E+00	8.632E-01	-1.984E-02	6.452E-02	5.126E-02	-3.432E-04
1.091E+00	8.763E-01	-1.700E-02	6.340E-02	4.545E-02	-2.375E-04
1.114E+00	8.826E-01	-1.586E-02	6.326E-02	4.584E-02	-1.904E-04
1.136E+00	8.960E-01	-1.607E-02	6.251E-02	5.249E-02	-1.931E-04
1.159E+00	9.070E-01	-1.569E-02	6.260E-02	4.995E-02	-2.766E-05
1.182E+00	9.179E-01	-1.442E-02	6.318E-02	4.980E-02	4.796E-07
1.205E+00	9.292E-01	-1.474E-02	6.144E-02	4.978E-02	1.242E-04
1.227E+00	9.330E-01	-1.576E-02	6.134E-02	5.117E-02	2.127E-04
1.250E+00	9.429E-01	-1.566E-02	6.258E-02	4.930E-02	1.914E-04
1.273E+00	9.478E-01	-1.656E-02	6.406E-02	5.015E-02	3.417E-04
1.295E+00	9.510E-01	-1.871E-02	6.634E-02	5.184E-02	4.519E-04
1.318E+00	9.520E-01	-1.964E-02	6.757E-02	4.766E-02	4.822E-04
1.341E+00	9.502E-01	-2.249E-02	7.071E-02	5.070E-02	5.320E-04
1.364E+00	9.495E-01	-2.405E-02	7.202E-02	5.552E-02	6.928E-04
1.386E+00	9.500E-01	-2.562E-02	7.395E-02	5.782E-02	6.095E-04
1.409E+00	9.403E-01	-2.717E-02	7.618E-02	6.265E-02	7.293E-04
1.432E+00	9.330E-01	-3.028E-02	7.787E-02	6.894E-02	8.098E-04
1.455E+00	9.319E-01	-3.062E-02	8.341E-02	7.296E-02	8.200E-04
1.477E+00	9.290E-01	-2.904E-02	7.945E-02	6.230E-02	9.455E-04
1.500E+00	9.181E-01	-3.061E-02	8.105E-02	6.533E-02	8.584E-04
1.523E+00	9.180E-01	-3.066E-02	8.104E-02	5.844E-02	9.663E-04
1.545E+00	9.103E-01	-3.057E-02	8.282E-02	5.507E-02	8.594E-04
1.568E+00	8.990E-01	-3.087E-02	8.161E-02	5.314E-02	9.359E-04
1.591E+00	8.926E-01	-3.116E-02	8.275E-02	5.182E-02	9.909E-04
1.614E+00	8.784E-01	-2.924E-02	8.159E-02	4.940E-02	8.601E-04
1.636E+00	8.666E-01	-3.062E-02	8.274E-02	5.031E-02	8.192E-04

1.659E+00	8.566E-01	-2.997E-02	8.349E-02	5.109E-02	7.966E-04
1.682E+00	8.395E-01	-2.992E-02	8.211E-02	4.683E-02	8.335E-04
1.705E+00	8.314E-01	-3.041E-02	8.085E-02	4.650E-02	6.857E-04
1.727E+00	8.102E-01	-2.958E-02	7.993E-02	4.454E-02	6.400E-04
1.750E+00	7.892E-01	-3.026E-02	7.394E-02	4.241E-02	4.790E-04
1.773E+00	7.727E-01	-3.194E-02	7.336E-02	4.238E-02	3.710E-04
1.795E+00	7.571E-01	-3.149E-02	7.431E-02	4.188E-02	3.260E-04
1.818E+00	7.383E-01	-3.085E-02	7.240E-02	4.166E-02	2.350E-04
1.841E+00	7.244E-01	-2.991E-02	7.222E-02	3.948E-02	1.650E-04
1.864E+00	7.103E-01	-2.978E-02	6.905E-02	3.996E-02	6.640E-05
1.886E+00	6.938E-01	-2.870E-02	6.469E-02	3.758E-02	-3.450E-05
1.909E+00	6.915E-01	-2.722E-02	6.209E-02	3.753E-02	-8.080E-05
1.932E+00	6.857E-01	-2.548E-02	6.249E-02	3.619E-02	-1.410E-04
1.955E+00	6.907E-01	-2.431E-02	5.347E-02	3.496E-02	-1.390E-04
1.977E+00	6.871E-01	-2.350E-02	5.218E-02	3.396E-02	-1.570E-04
2.000E+00	6.947E-01	-2.205E-02	5.088E-02	3.367E-02	-1.260E-04
2.023E+00	7.001E-01	-2.099E-02	5.242E-02	3.334E-02	-1.431E-04
2.045E+00	7.045E-01	-1.848E-02	5.231E-02	3.317E-02	-1.530E-04
2.068E+00	7.111E-01	-1.611E-02	5.409E-02	3.137E-02	-1.213E-04
2.091E+00	7.198E-01	-1.310E-02	5.219E-02	2.981E-02	-6.177E-05
2.114E+00	7.154E-01	-1.246E-02	5.548E-02	3.170E-02	-3.064E-05
2.136E+00	7.295E-01	-1.200E-02	5.447E-02	2.972E-02	5.522E-05
2.159E+00	7.310E-01	-1.360E-02	5.618E-02	3.141E-02	1.239E-04
2.182E+00	7.330E-01	-1.402E-02	5.774E-02	3.636E-02	1.969E-04
2.205E+00	7.396E-01	-1.516E-02	5.843E-02	3.884E-02	2.912E-04
2.227E+00	7.351E-01	-1.381E-02	6.282E-02	4.032E-02	4.139E-04
2.250E+00	7.380E-01	-1.244E-02	6.501E-02	4.473E-02	4.916E-04
2.273E+00	7.380E-01	-9.730E-03	7.087E-02	4.394E-02	5.421E-04
2.295E+00	7.368E-01	-7.830E-03	8.374E-02	4.838E-02	7.085E-04
2.318E+00	7.257E-01	-7.800E-04	1.020E-01	5.500E-02	8.697E-04
2.341E+00	6.961E-01	2.500E-03	1.480E-01	6.478E-02	1.280E-03
2.364E+00	6.500E-01	2.700E-03	2.099E-01	7.266E-02	1.890E-03
2.386E+00	4.617E-01	3.600E-03	3.269E-01	7.811E-02	2.520E-03
2.409E+00	2.774E-01	7.340E-03	3.505E-01	7.014E-02	1.990E-03
2.432E+00	5.091E-02	1.230E-03	1.833E-01	2.876E-02	5.267E-04
2.455E+00	3.044E-02	6.607E-04	1.197E-01	2.102E-02	1.971E-04
2.477E+00	-4.680E-04	9.200E-05	3.100E-03	5.130E-03	9.791E-08



### ANNEX 3: NOMENCLATURE

#### General

BPGs	Best Practice Guidelines
CAD	Computer-Aided Design
CAPS	CSNI Activity Proposal Sheet
CFD	Computational Fluid Dynamics
CFD4NRS	Computational Fluid Dynamics for Nuclear Reactor Safety (Workshop)
CPU	Central Processing Unit
CSNI	Committee on the Safety of Nuclear Installations
IAEA	International Atomic Energy Agency
IBM	Immersed Boundary Method
ISP	International Standard Problem
JRC NL	Joint Research Center, Petten, Netherlands
KAERI	Korea Atomic Energy Research Institute
LDA/LDV	Laser Doppler Anemometry/Laser Doppler Velocimetry
MATiS-H	Measurements and Analysis of Turbulence in Subchannels – Horizontal
NEA	Nuclear Energy Agency
NRS	Nuclear Reactor Safety
NURETH	Topical Meeting on Nuclear Reactor Thermal Hydraulics
OECD	Organisation for Economic Cooperation and Development
PIRT	Phenomena Identification Ranking Table
PRG	Project Review Group
R&D	Research and Development
RMS	Root-Mean Square
V&V	Verification and Validation
WG	Writing Group
WGAMA	Working Group on the Analysis and Management of Accidents
X, Y, Z	Cartesian Coordinates

**Variables**

$D_H$	Hydraulic Diameter
$P$	Pitch
$Re$	Reynolds Number
$Sp$	Split-type
$Sw$	Swirl-type
$u, v, w$	Cartesian Components of Instantaneous Velocity
$u', v', w'$	Cartesian Components of Fluctuating Velocity
$U, V, W$	Cartesian Components of Mean Velocity
$\omega$	Vorticity

**Turbulence Models**

BSL RSM	Baseline Reynolds Stress Model
DES	Detached Eddy Simulation
DNS	Direct Numerical Simulation
EARSM	Explicit Algebraic Reynolds Stress Model
EVM	Eddy Viscosity Model
LES	Large Eddy Simulation
NLEVM	Non-Linear Eddy Viscosity Model
RANS	Reynolds-Averaged Navier-Stokes
RSM	Reynolds-Stress Model
SAS	Scale-Adaptive Simulation
SGS	Sub-Grid Scale
SSG	Speziale-Sarkar-Gatski
SST	Shear Stress Transport
URANS	Unsteady Reynolds-Averaged Navier-Stokes
WALE	Wall-Adapting Local Eddy-viscosity